Investigation of Avalanche Flow and its Interaction with the Obstacles

Doctoral Thesis

By

Rakesh Kumar Aggarwal (2017MEZ0029)

Department of Mechanical Engineering

Submitted

in the partial fulfillment of the requirements of the degree

of

Doctor of Philosophy

to the



Indian Institute of Technology, Ropar Rupnagar 140001, India Sept, 2024 © Indian Institute of Technology Ropar- 2024 All rights reserved.



INDIAN INSTITUTE OF TECHNOLOGY ROPAR, PUNJAB, INDIA

CANDIDATE'S DECLARATION

I hereby certify that the work presented in this thesis, titled "Investigation of Avalanche and its Interaction with the Obstacles" in partial fulfillment of the requirements for the of the degree of Doctor of Philosophy and submitted to Department of Mechanical IIT, Ropar, is an authentic record of my own work carried out during the period 2018 to Sept, 2024 under the supervision of Dr. Ranjan Das and Dr. Hemendra Singh

The content presented in this thesis has not been submitted elsewhere for the award of any

(Mr. Rakesh Kumar Aggarwal)

3 Sept. 2024

to certify that the above statement made by the candidate is correct to the best of my ledge. The Ph.D. Viva-Voce examination of Mr. Rakesh, Research Scholar, has been held

= 23 Sept, 2024

(Dr. Ranjan Das)

(Dr. Hemendra Singh Gusain)

Acknowledgements

achievement of my life, let alone my doctoral programme's research work. It is their good that has made possible for me to shatter clouds of negativity and despair in my mind and forward to overcome every obstacle that showed up in my life. I also acknowledge the provided by my wife during this work.

my gratitude and thank go to my supervisors Dr. Ranjan Das and Dr. Hemendra Singh for helping me complete this research work by providing constant guidance from time to because of their insightful ideas that I was able to refine my every single work to the required for publishing in the academic community. Further, I would like to say my Ph.D. doctoral committee members; Prof. Navin Kumar, Dr. Himanshu Tyagi, Dr. Kumar and Dr. S C Martha for evaluating and giving the valuable remarks in my research also gratefully acknowledge the support provided by Director, Defence Geoinformatics Establishment (DGRE), DRDO, Chandigarh and other research facilities provided by Espar.

would like to express my deep gratitude to Dr. Amit Tyagi from CFEES (Now at HQ) who provided me useful tips for getting admission in Ph.D. at IIT, Ropar. Finally, I express my thankfulness to Dr. Amod Kumar from DGRE for providing me constant argument to pursue the doctoral programme. I would also like to thank Mr. Jagmohan and Md Irfan Akhtar from DGRE for providing administrative help during this work. I hark all my colleagues at IIT, Ropar who helped me whenever I needed them. I would like the amonymous Reviewers whose constructive comments and soons helped me to improve and publish my research work in the reputed also conferences. Indeed, I would like to thank each and everybody who might have helped to be way or another in completing this work. In the end, I thank God for helping me in through all the difficulties and challenges.

(Rakesh Kumar Aggarwal)

Abstract

At present, mainly, avalanche forecasting and avalanche control techniques are used to manage the avalanche hazards. Avalanche forecasting is in general issued over a large mountain area. This technique is suitable where limited movement of people and vehicles is there and frequency of avalanching is very less. Avalanche control is another technique which involves either permanent control of avalanches through the structure control or temporary control of avalanches through the artificial triggering of the unstable snow mass in the formation zone of the avalanche through explosives. Avalanche control becomes essential for busy highways, railway tracks, electric towers, or snow bound areas where large human population is involved. In order to control the avalanche, different avalanche control structures can be used in its path. In order to prevent initiation of avalanche from the formation zone itself, snow bridges, snow rakes and snow net structures can be used. Sometimes, due to terrain conditions, road conditions or some other constraints, it is not possible to install avalanche control structures in the formation zone. In that case, avalanche control structures like snow gallery, diversion wall etc. are installed in the middle zone of the avalanche path. These structures divert the direction of the avalanche. Catch dam, mounds and wedge type structures are typically installed in the runout zone of an avalanche. These structures retard, stop, or split the avalanche. The present study was undertaken with a focus on the track zone and runout zone avalanche control structures. The present design of these structures is mainly based on the empirical guidelines. In order that these structures can be installed at a large number of avalanche prone areas, it is important to have optimum design of these middle zone and runout zone avalanche control structures. To achieve this objective, accurate knowledge of the avalanche flow parameters i.e., avalanche impact pressure, flow depth, velocity, runout distance, dynamic coefficient of snow friction, shear forces, normal forces etc. is very important. A number of measurements are available for the above parameters but these experimental studies are not comprehensive in nature and cannot be used for the design of all kinds of avalanche control structures under varying conditions of mountain terrains, altitude, and snow types. To counter these shortcomings, a number of avalanche dynamics models developed by various researchers exist, which can simulate most of the avalanche flow

parameters mentioned above under different conditions. However, most of these models ignore the actual interaction of the avalanche with the obstacles/structures, which is vital for the accurate assessment of the avalanche impact pressures, velocity, drag coefficient, runout distance, lateral spread, debris deposition etc. Further, the available models for estimating the snow avalanche impact pressures are mostly one-dimensional (1-D), two-dimensional (2-D) or pseudo three-dimensional (3-D) in nature, which model the important avalanche flow parameters mentioned above with a large number of assumptions. In order to address some of these gaps, in the current work, 3-D non-Newtonian Navier-Stokes equations based simulation model has been developed. Further, the conventional no-slip fluid boundary condition was replaced by the slipwall boundary condition. The present model overcomes the limitations of previously used Newtonian fluid based models that fail to simulate the avalanche debris deposition and the depthaveraged models, which are not in position to accurately capture the avalanche-obstacle interaction process. Present simulation outcomes were observed in acceptable conformity with the experimental data with an average root mean squares error (RMSE) of 0.166 for the avalanche debris depth and RMSE of 1.48 for the avalanche front velocity. Further, for transient comparison, snow avalanche impact pressures were measured on an instrumented obstacle of 1 m height and 0.65 m width for high-density moist snow. This experimental set-up has been developed and installed on a 61 m long experimental facility i.e., snow chute at Dhundhi field research station located about 20 kms away from Manali, Himachal Pradesh (H.P.), India. Based on experimentations and simulations carried out in the current work, the measured and the simulated avalanche impact pressures were correlated, which can be used to estimate the avalanche impact pressures on the structures for the dense flow of avalanches. The root mean square error between the currently proposed model and the measured data is nearly 10.74, which is significantly lesser than the existing models for the estimation of the avalanche impact pressures on the obstacles. Further, the effective drag coefficient C'_d for the avalanche flow and the instrumented obstacle, which takes into account the combined effects of the fluid, solid, granular, and compressibility effects of the flowing snow, is found in the range of 3.97 to 8.54, which is in agreement with the published studies. Due to better control on the experimental conditions, accuracy and repeatability of the data is also expected to be high. This work related to the model development and validation is presented in Chapter 3 of the thesis. In this model, average value of dynamic coefficient of Coulomb friction between the snow chute surface and

the snow μ_k has been used as 0.12. This value was validated based on the thirty two measurements carried out during the period 2017-2020 for the shear force and normal force components of the avalanches. The measurements were carried out using a three component piezoelectric load cells based dynamometer, which in turn was installed on the 12° slope of the snow chute mentioned above. Details of this work are presented in Chapter 4 of the thesis. Lastly, an attempt has been made in the current work to simulate avalanche flow interaction with an Instrumented Tower installed in the path of an important avalanche site (named as MSP-10) at Dhundhi. Due to huge size of the mountain terrain, geometric and computational complexity was high. For this reason, the developed model was applied in the 2-D domain for these simulations. The present proposed model is able to simulate avalanche mass retention before the Instrumented Tower and avalanche impact pressure on its pylons. The simulated results are in agreement with the observations. The results gave the confidence that the proposed model can be used to simulate many such avalanche-obstacle situations for the better assessment of avalanche loads on the obstacles/structures. Details of this work are presented in Chapter 5 of the thesis. The thesis ends with the conclusions and the future scope of work. The present thesis may find its applications in assessment of avalanche impact pressures on the structures in the runout zone of the avalanche like catch dams, mounds etc. and numerical assessment of shear force and normal force components of an avalanche on snow sheds/galleries. However, present work may be more useful in case of high density wet snow conditions.

List of Publications

Journals

- [J1] Aggarwal, R.K., Das, R., Gusain, H.S. (2024). Accounting deviations between the measured and simulated impact pressures in high-density snow avalanches. *Arctic, Antarctic, and Alpine Research* 56(1):2302836. https://doi.org/10.1080/15230430.2024.2302836
- [J2] Aggarwal, R.K., Das, R., Gusain, H.S. (2024). New database for the estimation of dynamic coefficient of friction of snow. *Open Geosciences* 16(1):20220639. https://doi.org/10.1515/geo-2022-0639

Conference Proceedings

- [C1] Aggarwal, R.K., Das, R., Gusain, H.S. (2024). Development of a new instrumented structure for the measurement of avalanche impact pressure. 9th International and 49th National Conference on Fluid Mechanics and Fluid Power (FMFP-2022), IIT Roorkee, India, December 14-16, 2022. Published in Edited Book: Fluid Mechanics and Fluid Power (FMFP), Volume 7. FMFP 2022. Lecture Notes in Mechanical Engineering. Springer, Singapore. https://doi.org/10.1007/978-981-99-7047-6 27
- [C2] Aggarwal, R.K., Das, R., Gusain, H.S. (2024). Modelling of avalanche flow interaction with an Instrumented Tower at MSP-10 avalanche site, Dhundhi, India. *International Conference on Fluid, Thermal and Energy Systems (ICFTES'24), NIT Calicut*, June 6-8, 2024. (*Presented*)
- [C3] Aggarwal, R.K., Das, R., Gusain, H.S. (2024). Modelling of avalanche debris deposition in the presence and absence of an obstacle using a 3-D avalanche dynamics model (*to be communicated*).

Table of Contents

Acknowledgementsi	
Abstract	ii
List of Publications	V
List of Notations	xix
1. Introduction	1
1.1 Definition of a snow avalanche	1
1.2 Avalanche accidents	2
1.3 Necessary parameters for an avalanche occurrence	6
1.4 Types of avalanches	6
1.4.1 Based on the initiation mechanism and snow type	6
1.4.1.1 Loose snow avalanche	8
1.4.1.2 Slab avalanche	8
1.4.1.3 Glide avalanche	8
1.4.1.4 Powder avalanche	8
1.4.1.5 Wet snow avalanche	9
1.4.2 Based on the size	9
1.4.3 Open and confined avalanches	9
1.5 Range of avalanche speeds and impact pressures	9
1.6 Avalanche control and mitigation measures	10

	1.6.1 Artificial triggering	11
	1.6.2 Avalanche zoning	12
	1.6.3 Formation zone structures.	12
	1.6.4 Middle zone structures	13
	1.6.5 Runout zone structures	15
2.	Literature review	17
	2.1 Introduction.	17
	2.2 Literature survey	18
	2.2.1 Avalanche dynamics models	18
	2.2.2 Avalanche impact pressure, drag coefficient, and the parameters	
	2.2.3 Dynamic coefficient of friction of snow	28
	2.3 Summary of the literature survey	30
3.	Development of a 3-D avalanche dynamics model and its interact	ion with
	the obstacles	33
	3.1 Introduction.	33
	3.2 About the study area	33
	3.3 About the experimental site.	34
	3.4 Development of the 3-D avalanche dynamics model	35
	3.4.1 Assumptions in the model	35
	3.4.2 Main governing equations	36
	3.4.3 Discretization and numerical solution of the model	38

	3.4.4 Solver parameters for the simulations	39
	3.4.5 Domain, boundary conditions and the material properties	39
	3.4.5.1 Wall shear stress model	40
	3.4.5.2 Physical properties of snow and air	.42
	3.4.6 Mesh size dependence	44
	3.5 Experiments on snow chute, Dhundhi, and corresponding model simulations significant avalanche flow parameters	
	3.6 Dynamic similarity of the chute experiments with the real-scale avalanches	57
	3.7 Measured vs. simulated avalanche impact pressures	58
	3.7.1 About the avalanche impact pressure measurement sys	
	3.7.2 Experiments conducted using avalanche impact pressure measurement sys	
	3.7.3 Comparison between the simulated and the measured avalanche impressures.	_
	3.7.4 Estimation of the effective drag coefficient and corrected peak impact pressures the moist snow.	
	3.7.5 Comparison of simulated impact pressures with the other models	72
	3.8 Conclusions.	73
4.	Estimation of dynamic coefficient of friction of snow	75
	4.1 Introduction	75
	4.2 About the measurement system	75
	4.3 Installation of the measurement system.	76

Table of Contents

R	eferences	100
6.	Conclusions and future scope	98
	5.6 Conclusions.	96
	5.5 Results and discussion.	90
	5.4 Domain, meshing and boundary conditions	88
	5.3 Application of the model developed in current work	87
	5.2 Brief description of the study site	86
	5.1 Introduction.	86
	real avalanche site	86
5.	Simulation of avalanche flow interaction with an Instrume	nted Tower at a
	4.6 Conclusions	84
	4.5 Results and discussion.	78
	4.4 Measurement/computation procedure	77

List of Figures

Figure 1.1: A naturally triggered high density wet snow avalanche from Patalsu peak in Solang valley, Himachal Pradesh, India on 21 February, 2019 depicting (a) its movement (b) uprooting the trees in its path
Figure 1.2: A loose snow avalanche at Gulmarg, Jammu and Kashmir (J&K), India in January, 2023
Figure 1.3: A wet snow avalanche on 5 April, 2023 at Nathula, North Sikkim, India4
Figure 1.4: A naturally triggered dry snow powder avalanche in Sarbal region of Sonamarg area of Jammu and Kashmir, India on 8 February, 2024 showing its (a) initial movement (b) approaching the human habitation (c) hitting the shelters (Note: no loss of life and significant damage to property was reported due to this avalanche)
Figure 1.5: One skier killed while seven others rescued safely after a major powder snow avalanche hit Apharwat peak in world-famous ski-resort Gulmarg, J & K, India on 22 February, 2024
Figure 1.6: A number of vehicles buried under snow after a wet snow avalanche accident happened on 03 March, 2024 at Nehru Kund on the Manali-Solang road, Himachal Pradesh, India
Figure 1.7: After a wet snow avalanche accident happened on 29 March, 2024 in Hung area of Sonamarg, J & K, India vehicle (a) a number of vehicles hit and buried under snow (b) rescue operations being carried out to extract the trapped vehicles and the people
Figure 1.8: Section of an arbitrary mountain depicting necessary factors for avalanche occurrence

Figure 1.9: Depiction of three main zones of a real avalanche site located in Greater Himalayar range of Himachal Pradesh, India
Figure 1.10: Snow bridge structures in the formation zone at Banihal top, J & K, India12
Figure 1.11: Snow umbrella type structures installed in the formation zone at MSP-6 site Dhundhi, Himachal Pradesh, India
Figure 1.12: A 135 m long snow shed at MSP-3 avalanche site, Dhundhi, H.P., India14
Figure 1.13: A 120 m long snow shed at MSP-7 avalanche site, Dhundhi, H.P., India14
Figure 1.14: A 240 m long and 8 m high catch dam at MNP-3 avalanche site, north portal of Atatunnel, Himachal Pradesh, India
Figure 1.15: Integrated scheme of earthen mounds and diversion wall used for the protection of Shri Badrinath temple, Uttarakhand, India
Figure 3.1: A view of the (a) field research station of DGRE at Dhundhi (b) observatory for recording meteorological parameters and the snowpack information
Figure 3.2: A view of the experimental facility, snow chute at Dhundhi, Himachal Pradesh India
Figure 3.3: Boundary conditions for the 3-D geometry of snow chute at Dhundhi, H.P. India
Figure 3.4: Wall shear stress components of snow on an inclined plane (here, $\tau_{s wall}$ (N m ⁻²) stands for the total wall shear stress of snow; $\tau_{s wall}$ (N m ⁻²) stands for the x-component of $\tau_{s wall}$; $\tau_{s wall}$ (N m ⁻²) stands for the y-component of $\tau_{s wall}$ and θ is the angle of the plane in degrees)
Figure 3.5: Flow rheology of snow as a bi-viscous Bingham fluid (here, τ_0 (N m ⁻²) stands for the yield strength of snow; η_0 (N s m ⁻²) stands for the dynamic viscosity of snow in the locked portion of the flow; k (N s m ⁻²) stands for the dynamic viscosity of snow after the yield region and $\dot{\gamma}_0$ (s ⁻¹) stands for the shear strain rate of snow in the locked portion of the flow).

Figure 3.6: Simulated contours of snow velocity v_s at a time-step $t=1.5$ s, after the release of
equal volume of snow from the hopper of the snow chute, Dhundhi, H.P., India and also keeping
all other input conditions same, except varying the mesh sizes as (a) 0.05 m (b) 0.1 m (c) 0.2
m45
Figure 3.7: Observed snow avalanche mass at various time-steps t of the flow during the
experiment on 5 March, 2018 at snow chute, Dhundhi, H.P., India47
Figure 3.8: Simulated contours of snow avalanche mass corresponding to the experiment on 5
March, 2018 at snow chute, Dhundhi
Figure 3.9: Point-wise comparison between the observed and simulated snow avalanche debris
depth d_s for the experiment on 5 March, 2018 at snow chute, Dhundhi
Figure 3.10: Simulation of snow velocity near the test bed of the snow chute, Dhundhi
corresponding to the experiment on 5 March, 2018, when snow is assumed as a (a) Newtonian
fluid (b) bi-viscous Bingham fluid50
Figure 3.11: Profile of snow avalanche debris depth d_s for the experiment on 4 March, 2018 at
the test bed area of the snow chute, Dhundhi (a) simulated (b) observed (c) observed vs.
simulated point-wise data50
Figure 3.12: Profile of snow avalanche debris depth d_s for the experiment on 7 March, 2018 at
the test bed area of the snow chute, Dhundhi (a) simulated (b) observed (c) observed vs.
simulated point-wise data51
Figure 3.13: Profile of snow avalanche debris depth d_s for the experiment on 21 Feb, 2019 at the
test bed area of the snow chute, Dhundhi (a) simulated (b) observed (c) observed vs. simulated
point-wise data51
Figure 3.14: Profile of snow avalanche debris depth d_s for the experiment on 25 Feb, 2019 at the
test bed area of the snow chute, Dhundhi (a) simulated (b) observed (c) observed vs. simulated
point-wise data

Figure 3.15: Profile of snow avalanche debris depth d_s for the experiment on 25 Jan 2020 at the
test bed area of the snow chute, Dhundhi (a) simulated (b) observed (c) observed vs. simulated
point-wise data52
Figure 3.16: Simulation of snow velocity v_s at different time steps t for the experiment conducted on 05 March, 2018
Figure 3.17: Point-wise comparison between the simulated and estimated avalanche front velocities v_{fr} at the end of 12° slope of the snow chute
Figure 3.18: Variation of the simulated snow velocity v_s profile (a) at the hopper exit (b) on 30° and 12° slopes.
Figure 3.19: Transient variation of the simulated (a) snow dynamic viscosity η_s (a) snow strain rate $\dot{\gamma}$
Figure 3.20: Variation of simulated snow slip-velocity $v_{s, slip}$ all along the length of the snow chute
Figure 3.21: Simulated contour of air blast velocity v_a over the snow mass
Figure 3.22: Variation of simulated Reynolds number R_e and Froude number F_r of the flowing snow shown as a function of distance, just after the snow is released from the hopper of the snow chute, Dhundhi, H.P., India, for the demonstration of the dynamic behavior of the chute avalanches versus real avalanches
Figure 3.23: Schematic of the avalanche impact pressure measurement system (<i>AIPMS</i>) showing (a) its position at a distance of 0.9 m from the end of 12° slope of the snow chute (b) its front plate facing the avalanche (c) its side view showing the back support detail
Figure 3.24: A view of the avalanche impact pressure measurement system (<i>AIPMS</i>) installed on snow chute, Dhundhi, H.P., India

Figure 3.25: A view of the interaction of the snow avalanches with AIPMS at snow chute, Dhundhi (H.P., India)
Figure 3.26: Measurement of the avalanche impact pressures P_m by AIPMS after complete blocking of the avalanche flow from the sides with barriers (Experiment E2 on 15 March, 2021)
Figure 3.27: Simulation results on experiment on 17 Feb, 2020 for avalanche flow mass and its interaction with AIPMS at various time-steps <i>t</i> of the flow
Figure 3.28: At a time-step $t = 5.2$ s, simulated (a) snow velocity v_s (b) snow total pressure (impact pressure) P_s (Experiment on 17 Feb, 2020)
Figure 3.29: Observation of the avalanche flow and its depth at the significant points on the snow chute at various flow time-steps <i>t</i> during the experiment carried out on 17 Feb, 2020
Figure 3.30: Simulated versus measured avalanche impact pressures at (a) 0.2 m depth from the snow chute test bed surface (b) 0.6 m depth from the snow chute test bed surface (Experiments on 14 Feb, 2020; 17 Feb, 2020 and 23 Feb, 2020)
Figure 3.31: Simulated versus measured avalanche impact pressures at (a) 0.2 m depth from the snow chute test bed surface (b) 0.6 m depth from the snow chute test bed surface (Experiments on 15 March, 2021 (E1);18 March, 2021 and 19 March, 2021)
Figure 3.32: Simulated versus measured avalanche impact pressures after complete blocking of flow from the sides with the barriers at (a) 0.2 m depth from the snow chute test bed surface (b) 0.6 m depth from the snow chute test bed surface (Experiment E2 on 15 March, 2021)

Figure 3.33: Variation of simulated fluid drag coefficient C_d and the corresponding effective drag coefficient C'_d during the avalanche flow-obstacle interaction process in case of the experiments conducted on (a) 15 March, 2021 (E1, $\rho_i = 578 \text{ kg m}^{-3}$) (b) 14 Feb, 2020 ($\rho_i = 325 \text{ kg m}^{-3}$)
Figure 3.34: A comparison of deviations between the output of present proposed model P_i and other well-known models for the estimation of peak avalanche impact pressures on the obstacles (here, deviations for the above models are calculated with reference to the peak measured avalanche impact pressures $P_{m, max}$ in the current experiments)
Figure 4.1: Measuring system for shear force (F_x) and normal force (F_z) components of an avalanche
Figure 4.2: (a) A view of the snow chute at Dhundhi, Himachal Pradesh, India (b) close view of the dynamometer installed on 12° slope of the snow chute (c) a view of the data acquisition and display details of the snow dynamic coefficient of friction μ_k measurement system.
Figure 4.3: Display of voltage values on the computer screens during an experiment at snow chute, Dhundhi, H.P., India corresponding to (a) shear force F_x , F_y components and (b) normal force F_z components
Figure 4.4: Variation of (a) shear force F_x (N) with snow density ρ_i (kg m ⁻³) (b) normal force F_z (N) with snow density ρ_i (kg m ⁻³)82
Figure 4.5: Variation of dynamic coefficient of friction of snow μ_k with its density $\rho_i (\text{kg m}^{-3})$ 82
Figure 5.1: Observation of maximum standing snow depth $h_{ss, max}$ and three days maximum increment $\Delta h_{ss, max}$, for the months December–March (1990–2019) at Dhundhi field observatory, H.P., India.
Figure 5.2: Observation of maximum standing snow depth <i>hss., max</i> , in the month of April (1990–2019) at Dhundhi field observatory, H.P., India

Figure 5.3: Drawing of elevation profile along the preferential avalanche flow direction for MSP-10 avalanche site at Dhundhi, H.P., India
Figure 5.4: Geometric domain for MSP-10 avalanche site with Instrumented Tower at Dhundhi, H.P., India
Figure 5.5: Instrumented Tower at MSP-10, Dhundhi, H.P., India (a) a close view of the real structure at the site (b) 2-D simplified geometry used for the CFD model simulations
Figure 5.6: Simulation of avalanche flow interaction with an Instrumented Tower at MSP-10 avalanche site, Dhundhi, Himachal Pradesh, India at various time-steps t of the flow for snow density $\rho_i = 200 \text{ kg m}^{-3}$ and snow fracture depth $h_d = 1.7 \text{ m}$ (Case C1)91
Figure 5.7: Simulation of (a) snow volume fraction (b) snow velocity v_s (m s ⁻¹) (c) snow total pressure P_s (Pa), in the three cases (C1, C2 & C3) having different snow density ρ_i (kg m ⁻³) and fracture depth h_d (m) in the formation zone of the avalanche, at a time-step t =35 s and wall slip factor W_s =0.25.
Figure 5.8: Simulation of (a) snow volume fraction (b) snow velocity v_s (m s ⁻¹) (c) snow total pressure P_s (Pa), in the three cases (C1, C2 & C3) having different snow density ρ_i (kg m ⁻³) and fracture depth h_d (m) in the formation zone of the avalanche, at a time-step t =45 s and wall slip factor W_s =0.25
Figure 5.9: A zoomed view of simulation of snow velocity v_s (m s ⁻¹), in the three cases (C1, C2 & C3) having different snow density ρ_i (kg m ⁻³) and fracture depth h_d (m) in the formation zone of the avalanche, at a time-step t =45 s and wall slip factor W_s =0.2594
Figure 5.10: A zoomed view of simulation of snow total pressure P_s (Pa), in the three cases (C1, C2 & C3) having different snow density ρ_i (kg m ⁻³) and fracture depth h_d (m) in the formation zone of the avalanche, at a time-step t =45 s and wall slip factor W_s =0.25.

List of Tables

Table 1.1: Classification of size of an avalanche
Table 3.1: Effect of varying mesh size on the model simulations
Table 3.2: Summary of the experiments for finding significant avalanche flow parameters at snow chute, Dhundhi, Himachal Pradesh, India
Table 3.3: Summary of the experiments for the measurement of avalanche impact pressure P_m at snow chute, Dhundhi, Himachal Pradesh, India
Table 3.4: Ratio R_p of the peak values of the measured avalanche impact pressures $P_{m, max}$ and simulated avalanche impact pressures $P_{s, max}$
Table 4.1: Summary of the measurements for shear force F_x and normal force F_z components of
an avalanche during the period 2017-2020 at snow chute, Dhundhi, Himachal Pradesh,
India81

List of Notations

```
C'_d: effective drag coefficient (between the avalanche and obstacle)
\mu_k: dynamic coefficient of friction between the snow chute surface and snow
\xi: turbulent friction coefficient, m s<sup>-2</sup>
\rho_i: average snow density in the snow chute hopper/before hitting any obstacle, kg m<sup>-3</sup>
T_s: temperature of snow, °C
V: snow filling capacity of the snow chute hopper, m<sup>3</sup>
\alpha_s: volume fraction of snow phase
\alpha_a: volume fraction of air phase
V<sub>s</sub>: volume of a secondary phase 's' (snow)
\vec{v}_{\rm s}: velocity vector of snow, m s<sup>-1</sup>
p: hydrodynamic/gauge pressure shared by both the primary (air) and secondary phases (snow),
   (N m^{-2})
\vec{q}: acceleration due to gravity, m s<sup>-2</sup>
\bar{\bar{\tau}}_s: phase stress-strain tensor for snow, N m<sup>-2</sup>
\eta_{\rm S}: shear viscosity of snow, N s m<sup>-2</sup>
\lambda_s: bulk viscosity of snow, N s m<sup>-2</sup>
\overline{\overline{I}}: unit tensor
\vec{R}_{as}: interaction force between the snow and air phases, N m<sup>-3</sup>
K_{as}: interphase momentum exchange coefficient, kg m<sup>-3</sup> s<sup>-1</sup>
```

```
\delta_{as}: particulate relaxation time, s
f: drag function
ω: drag coefficient (relative between the snow and air phases)
R_{ee}: relative Reynolds number between the snow and air phases
\rho_{\rm sa}: mixture density of snow and air, kg m<sup>-3</sup>
\mu_{sa}: mixture viscosity of snow and air, N s m<sup>-2</sup>
\mu_a: dynamic viscosity of air, N s m<sup>-2</sup>
d_{\text{sa}}: mixture particle diameter of snow and air, m
d_i: particle diameter of the primary air phase, m
d_a: particle diameter of the secondary snow phase, m
\varepsilon: computation time-step for the simulations, s
\tau_{s|wall}: total wall shear stress at the snow and snow chute-bottom interface, N m<sup>-2</sup>
W<sub>s</sub>: wall slip factor
h_s: simulated depth of the snow, m
\theta: angle of the snow chute/mountain slope, degree (to be converted in radians in the equations)
\rho_a: density of air, kg m<sup>-3</sup>
τ: shear stress intensity for snow, N m<sup>-2</sup>
τ<sub>0</sub>: yield stress/strength of snow, N m<sup>-2</sup>
\eta_0 : dynamic viscosity of snow in the locked portion of the flow, N s \rm m^{\text{-}2}
\dot{\gamma}_0 : shear strain rate of snow in the locked portion of the flow, s^{\text{-}1}
\dot{\gamma}: shear strain rate of snow after the yield region, s<sup>-1</sup>
k: dynamic viscosity of snow after the yield region, N s m<sup>-2</sup>
```

```
c: cohesion strength between the snow grains, N m<sup>-2</sup>
φ: internal friction angle of snow, degree (to be converted in radians in the equations)
\eta_s: effective Newtonian viscosity of snow for a bi-viscous Bingham fluid, N s m<sup>-2</sup> (Pa s)
\overline{\overline{D}}: second invariant of rate of deformation tensor, s<sup>-1</sup>
\beta: angle of repose of snow, degree
t: avalanche flow time-step, s
v_s: magnitude of snow velocity, m s<sup>-1</sup>
v<sub>s, max</sub>: simulated maximum snow velocity, m s<sup>-1</sup>
d_s: avalanche debris depth, m
\rho_f: average avalanche debris density, kg m<sup>-3</sup>
v_{fr}: simulated avalanche front velocity, m s<sup>-1</sup>
v<sub>s. slip</sub>: simulated snow slip-velocity at the snow chute-snow interface, m s<sup>-1</sup>
v_a: air blast velocity, m s<sup>-1</sup>
F_r: Froude number
R<sub>e</sub>: Reynolds number
P_m: measured avalanche impact pressure values, Pa/kPa
Pd: snow dynamic pressure, Pa/kPa
P<sub>s</sub>: simulated snow total pressure/avalanche impact pressure, Pa/kPa
P_{m, max}: peak value of the measured avalanche impact pressure, kPa
P_{s, max}: peak value of the simulated avalanche impact pressure, kPa
R_p: ratio of peak value of measured avalanche impact pressure and the peak value of the
```

simulated avalanche impact pressure

 F_d : drag force computed on the frontal projected area of the avalanche impact pressure measurement system (AIPMS), N

 A_p : frontal projected area of the AIPMS, m²

 v_{sf} : average free stream snow velocity, m s⁻¹

Cd: fluid drag coefficient for the snow and obstacle

Pi: corrected simulated peak avalanche impact pressure on an obstacle, Pa/kPa

 F_x : net shear force of the flowing avalanche in the x-direction, N

 F_y : net shear force of the flowing avalanche in the y-direction, N

 F_z : net normal force of the flowing avalanche in the z-direction, N

hd: snow fracture depth in the formation zone, m

 $\Delta h_{ss, max}$: three days maximum increment in standing snow, cm

 A_d : average altitude of the formation zone of the MSP-10 avalanche site, m

Chapter 1

Introduction

1.1 Definition of a snow avalanche

Snow avalanche is defined as a sudden gravity-driven mass of snow that once triggered due to failure of the weak layer within a seasonal snowpack, moves down the mountain slopes. Avalanches can also contain rocks, soil, ice or trees along with the snow. The movement of the avalanche is principally due to the gravity. However, sometimes, other factors like snow drift due to wind, earthquake or a helicopter sound may contribute in triggering the avalanche. In general, avalanches affect people directly by causing injury or death or by detaining them. Avalanches also cause property damage and affect the environment (McClung and Schaerer, 1999). Some of the major sectors affected by avalanches are:

- Avalanches cause interruption of movement of people and vehicles on the important highways and railways in the snow bound mountainous areas.
- Many countries of the World prominently; Switzerland, Austria, Italy, Japan, China, Canada and United States are affected by the avalanches. In India, avalanches pose danger mainly to the Army deployed in Jammu & Kashmir, Uttarakhand and North East of India.
- Avalanches destroy buildings and kill or injure residents in the avalanche prone areas of the World. Engineers have to judiciously decide regarding the placement, design, and protection of facilities and operations in avalanche prone mountainous terrain.
- Sometimes, telephone and electric transmission towers and lines, and ski lift towers are severely affected by the avalanches and so need proper protection from the avalanche hazard. The tremendous growth in the backcountry winter mountain travel activities like skiing, mountaineering and snowmobiling have increased the number of avalanche fatalities.

• In a few cases, avalanches may hit the hydroelectric projects and block the path of the rivers.

1.2 Avalanche accidents

Avalanche incidents happen almost every year at various parts of the snow bound mountainous regions of the World. Due to increasing human intervention, most of the snow bound mountain areas have become hazardous with the passage of time and so, a large number of avalanche accidents every year in some part of the world. Avalanche hazard occurs more in the thickly populated areas. To recall some of the major historical events, during third century BC, African general Hannibal Barca lost eighteen thousand men, two thousand horses and several elephants, while crossing the mountains to invade Italy from the north, according to Roman historians (Internet resource 1). In March, 1910, ninety six people were killed when two trains were bowled off the track near Stevens Pass, Washington due to an avalanche; 62 workmen were killed at Rogers Pass, British Columbia, while attempting to shovel the track buried by an earlier avalanche). On January 20, 1951, an estimated 240 people died when accumulated snow gave way after a series of heavy rains, sweeping down on a dozen towns in Austria, Italy and Switzerland. In 1979, widespread avalanche activity across the Lahul and Spiti region of Indian Himalaya resulted in the deaths of about 200 people (McClung and Schaerer, 1999). A glimpse of some of the recent avalanche accidents in India are depicted in Figures 1.1–1.7.

The past historical avalanche tragedies and the recent avalanche accidents mentioned above motivate the human race to take up this nature's challenge more sternly and work further to make precious human lives safer and also protect the important infrastructure, roads and buildings from the avalanche disasters. A number of technologies have been developed over the years by various researchers all over the world to mitigate the threat of the avalanches. Still there are a lot of challenges to be addressed by the Scientists for improving human safety in the snow bound mountains. A feeling of safety will enable people to enjoy the beauty of snow clad mountains without the fear of being trapped by the avalanches.

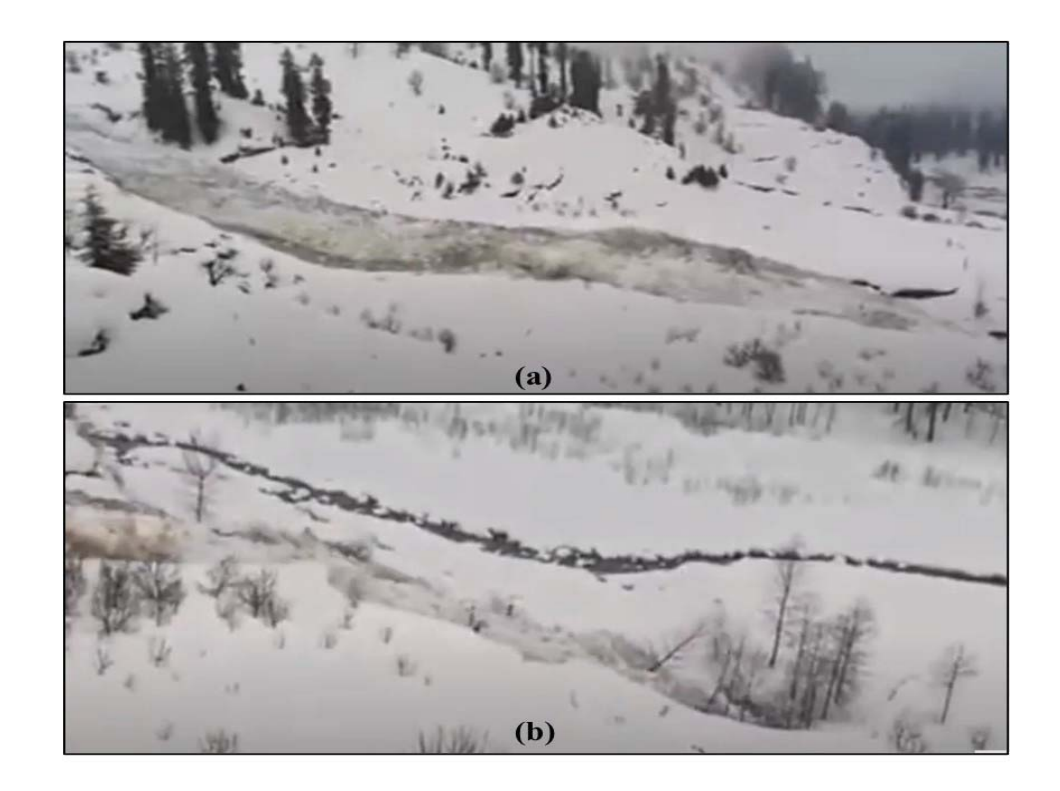


Figure 1.1: A naturally triggered high density wet snow avalanche from Patalsu peak in Solang valley, Himachal Pradesh, India on 21 February, 2019 depicting (a) its movement (b) uprooting the trees in its path



Figure 1.2: A loose snow avalanche at Gulmarg, Jammu and Kashmir (J&K), India in January, 2023



Figure 1.3: A wet snow avalanche on 5 April, 2023 at Nathula, North Sikkim, India

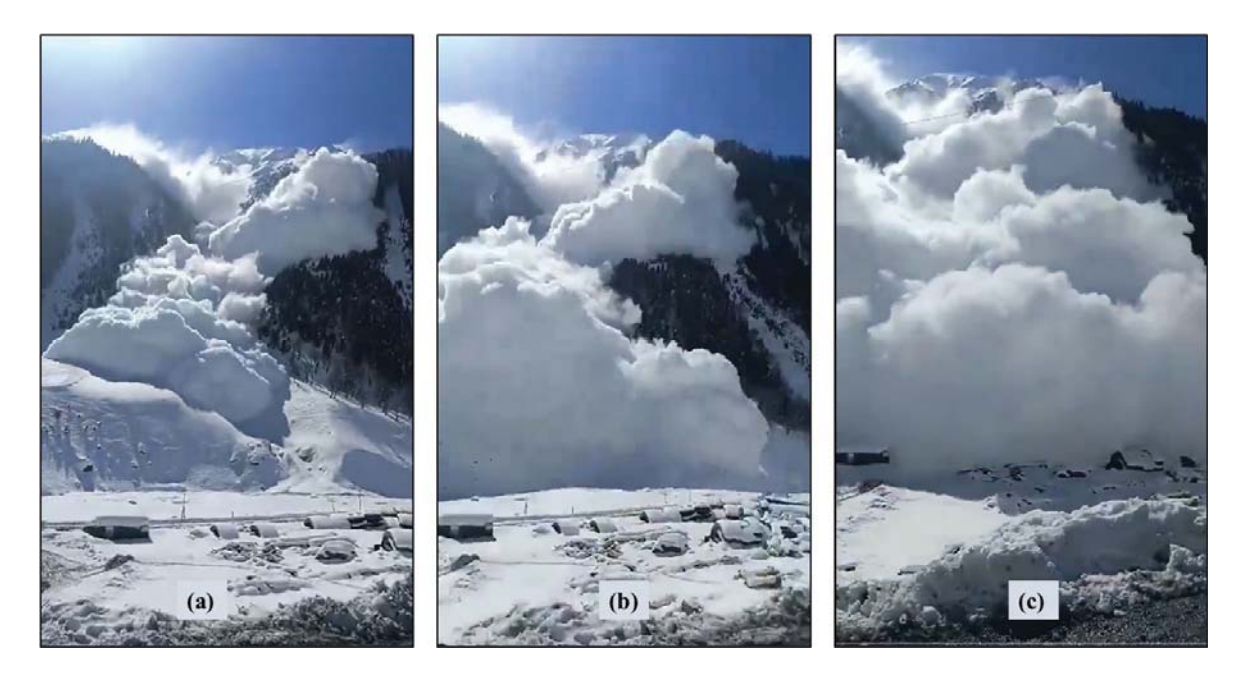


Figure 1.4: A naturally triggered dry snow powder avalanche in Sarbal region of Sonamarg area of Jammu and Kashmir, India on 8 February, 2024 showing its (a) initial movement (b) approaching the human habitation (c) hitting the shelters (*Note: no loss of life and significant damage to property was reported due to this avalanche*)



Figure 1.5: One skier killed while seven others rescued safely after a major powder snow avalanche hit Apharwat peak in world-famous ski-resort Gulmarg, J & K, India on 22 February, 2024



Figure 1.6: A number of vehicles buried under snow after a wet snow avalanche accident happened on 03 March, 2024 at Nehru Kund on the Manali-Solang road, Himachal Pradesh, India





Figure 1.7: After a wet snow avalanche accident happened on 29 March, 2024 in Hung area of Sonamarg, J & K, India vehicle (a) a number of vehicles hit and buried under snow (b) rescue operations being carried out to extract the trapped vehicles and the people

1.3 Necessary parameters for an avalanche occurrence

Snow avalanches are the constant physical-geographical phenomenon (Khapayev, 1978). For convenience path is divided into three zones; formation zone or start zone having an average slope varying from 30° to 50° from where the avalanche generally triggers, track zone or middle zone having an average slope varying from 12° to 30° where the avalanche gains acceleration, and runout zone or deposition zone having an average slope < 12° where the avalanche loses its momentum and finally stops. It is very well observed that an avalanche can occur only when a suitable combination of favorable factors of formation zone mountain slope $(30^{\circ}-50^{\circ})$, weather and snow are present as shown by Figures 1.8–1.9. If any one of these factors is absent, avalanche will not come. To elaborate further, avalanche formation requires that the shear stress acting on the weak snow layer in the snowpack equals or exceeds the shear strength of this layer (McClung and Schaerer, 1999).

1.4 Types of avalanches

1.4.1 Based on the initiation mechanism and snow type

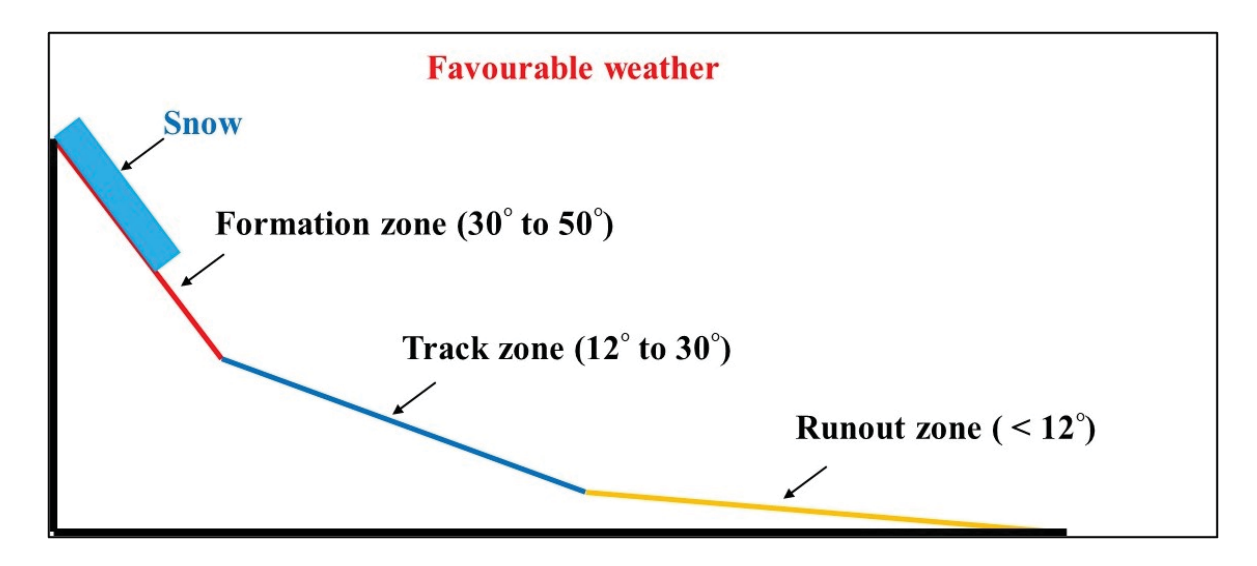


Figure 1.8: Section of an arbitrary mountain depicting necessary factors for avalanche occurrence

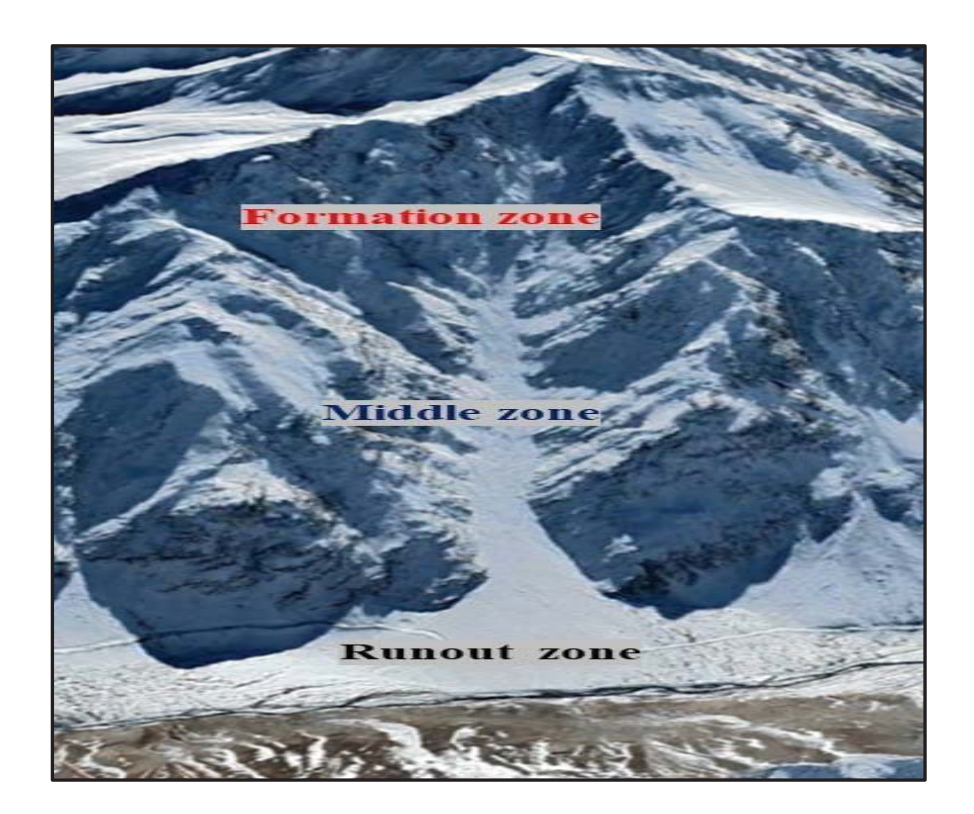


Figure 1.9: Depiction of three main zones of a real avalanche site located in Greater Himalayan range of Himachal Pradesh, India

1.4.1.1 Loose snow avalanche

Loose snow avalanches have a single point of origin from there they widen in a triangular pattern, as more snow is pushed down the slope and entrained into the slide (McClung and Schaerer, 1999). These avalanches generally happen after fresh snowfall and are less dangerous. They are sometimes called sluffs also. Dry flowing avalanches have density in the range of 100–150 kg m⁻³. A typically small dry snow avalanche has deposits density in the range of 200 kg m⁻³ while medium to large dry snow avalanche has debris deposits density in the range of 300–400 kg m⁻³.

1.4.1.2 Slab avalanche

Because of high-density of snow, slab avalanche, is usually more dangerous and responsible for more than 90% of the deaths that occur due to avalanches. It initiates by a failure at a depth in the snow cover, ultimately resulting in a block of snow. Slab avalanches have a distinct, broad fracture line. They can occur only when a bonded layer of snow slab is lying on top of a weak layer over a sufficiently large area. Slab avalanches can occur in dry or wet snow, even a long time after any snowfall. Speed of slab avalanches can go up to 40 m s⁻¹. These avalanches are often set off by skiers, wind or temperature changes (Internet resource 4).

1.4.1.3 Glide avalanche

Glide avalanches occur when a layer of snow slides down a slope as a single mass. They are often triggered by the movement of the underlying ground or by changes in temperature. Glide avalanches can be very dangerous because they can occur suddenly and without warning.

1.4.1.4 Powder avalanche

Powder snow avalanches are those avalanches in which a dense core of snow is absent and it consists of only a cloud of snow particles suspended in air, which can change into a larger avalanche as it progresses down the slope. Powder snow avalanches occur when a layer of fresh, dry snow becomes unstable and slides down a steep slope (> 40°). Powder avalanches can gain speeds up to 80 m s⁻¹. A dangerous wind blast precedes the fast moving snow. The runout distance of these avalanches is very large. Typically snow density in the powder avalanche is in

8

the order of 10 kg m⁻³ and air blast has density in the order of 1 kg m⁻³ (McClung and Schaerer, 1999).

1.4.1.5 Wet snow avalanche

Wet snow avalanches occur when a layer of wet snow becomes unstable and slides down a slope. This type of avalanche is more common in areas with a wet climate and high moisture content in the snow. Wet snow avalanches can be triggered by rain, temperature changes, or human activity. Wet flowing avalanche has density in the range of 150–200 kg m⁻³ while avalanche debris deposits have density in the range of 500–600 kg m⁻³ (Internet resource 4).

1.4.2 Based on the size

Avalanche size classification is a subjective topic. Each country has its own norms in classifying the avalanche size. Relatively, most comprehensive classification by the European avalanche warning services divides avalanches into five size categories as shown in Table 1.1 (Internet resources 5 and 6).

1.4.3 Open and confined avalanches

Open avalanches have no wall on the lateral sides of the avalanche path while a confined avalanche has path in the form of a gully. Most of the avalanches on nature are of confined type.

1.5 Range of avalanche speeds and impact pressures

Flow velocities of snow avalanches vary in the range of 15 m s⁻¹ to 60 m s⁻¹ for large dry snow avalanches, whereas wet avalanches move with moderate speeds in the range of 6–30 m s⁻¹. If the avalanche path is steep, dry snow avalanches may generate a powder cloud which can travel with speeds up to 90 m s⁻¹. However, the destructive potential of wet snow avalanches is much higher as compared to dry snow avalanches and powder avalanches. In a slab avalanche, the mass of descending snow may reach a speed of 40 m s⁻¹ and is capable of destroying forests and small villages in its path.

Avalanche impact pressure mainly depends upon the avalanche speed and snow density. In general, avalanche impact pressures vary from just 1 kPa for a small avalanche (relatively harmless to people) to the order of 1000 kPa for an extreme avalanche (can destroy a village or

Table 1.1: Classification of size of an avalanche

Size classification	Typical path travel length	Volume (m ³)	Runout distance (m)	Potential damage
	(m)			
Small (sluff)	< 50	100	Stops on steep slope	Unlikely to bury a person. In extreme terrain there is a danger of falling.
Medium	50-200	1000	Can reach the end of the relevant slope	Can bury, injure or kill people
Large	Several hundred meters	10000	Can cross flat terrain (well below 30°) over a distance of less than 50 m	Can bury and destroy cars, damage trucks, destroy small buildings and break a few trees
Very large	> 2000	100000	Traverses flat terrain (well below 30°) over a distance of more than 50 m	Can bury and destroy trucks and trains Can destroy fairly large buildings and small areas of forest.
Extremely large	> 2000	> 100000	Reaches the valley floor	Can devastate the landscape and has catastrophic destructive potential

forest) (McClung and Schaerer, 2011).

1.6 Avalanche control and mitigation measures

One simple method to escape the hazard of avalanches is just to skip the routes endangered by avalanches but this is practically not possible due to defence requirements, increasing population, recreational sports activities and international tourism all over the world. So, the only option left is to increase the safety of the humans and the property in the avalanche prone mountainous terrain through various scientific and engineering techniques. At present, mainly following methods are employed for this purpose:

• Avalanche forecasting

• Avalanche control

Snow avalanche forecasting is defined as supplying estimates of both current and future snow stability. Avalanche forecasting involves the integration of all available information into a prediction (McClung and Schaerer, 1999). The forecasting depends upon a number of meteorological factors. Both numerical avalanche prediction models and process-oriented models can be used for issuing prediction. Avalanche forecasting is in general issued over a large mountain area. This technique is suitable where limited movement of people and vehicles is there and frequency of avalanching is very less.

Avalanche control begins with a risk assessment conducted by surveying for potential avalanche terrain by identifying geographic features such as vegetation patterns, drainages, and seasonal snow distribution that are indicative of avalanches. From the identified avalanche risks, the hazard is assessed by identifying threatened human geographic features such as roads, skihills, and buildings. The prevention and mitigation plans include three major groups of interventions; active, passive and social awareness programmes. Avalanche control techniques either directly intervene in the evolution of the snow pack, or lessen the effect of an avalanche once it has occurred. Active methods include avoidance due to land use restrictions, temporary evacuation and artificial triggering. Passive measures include formation zone structures and afforestation to prevent avalanche initiation, diversion structures, dams, retarding structures etc. Social awareness includes making people aware about the precautions and thumb rules to be followed in the avalanche terrains (Internet resource 2). Brief description of the various techniques mentioned above is given below:

1.6.1 Artificial triggering

Artificial triggering of avalanches is a widely used cost-effective method for protecting roads, important highways, railroads, ski areas and other sites that can be efficiently and completely evacuated, and there is little or no risk of property damage. Explosive techniques involve the artificial triggering of smaller less destructive avalanches, by detonating charges either above or on the snow surface. The explosives may be deployed by manually hand tossing and lowering, by bombing from a helicopter, or by shelling with a howitzer, recoilless rifle, or air gun (Internet

resource 2). Sometimes, this technique is used in war situations also. In World War I, during fighting in the Alps on the Austrian-Italian front in December 1916, more than 10,000 troops were killed in a single day by avalanches triggered by artillery fired onto slopes of unstable snow (Internet resource 3). The biggest challenge in this method is the accurate assessment of the snowpack instability and then plan the operations accordingly.

1.6.2 Avalanche zoning

Avalanche zoning is probably the most reliable means of minimizing risk in avalanche terrain. However, the costs for obtaining high-quality avalanche hazard maps can be significant, and regardless of effort, hazard zone boundaries will entail some uncertainty.

1.6.3 Formation zone structures

Snow bridges, snow rakes and snow nets are the structures generally used in the formation zone of an avalanche to arrest the initiation of the avalanche (Figure 1.10). In a few cases, afforestation is also found to be a viable option for arresting creep and glide motion of the avalanches. Recently, because of their better ground anchoring and ease of installation, snow umbrella type structures also being used in the formation zone at few avalanche sites (Figure 1.11). These structures bring discontinuity in the snowpack and limit the fracture propagation and the avalanche size. The structures are used when volume of traffic on the related axis is high



Figure 1.10: Snow bridge structures in the formation zone at Banihal top, J & K, India



Figure 1.11: Snow umbrella type structures installed in the formation zone at MSP-6 site, Dhundhi, Himachal Pradesh, India

and avalanche forecasting and other techniques prove to be less effective in mitigating the avalanche threat to the people and the infrastructure. The structures are built in continuous rows over the full width and length of avalanche starting zones. The distance between rows, which is a function of the slope incline and the snow depth, may vary in the range of 10–40 m. The structures are at least as high as the expected greatest snow depth. The main disadvantage of this method is high initial cost. Other limitations are that these structures prove less effective in case of deep snow, unstable soil, and rugged and steep terrain. This technique proves cost effective for heavily populated areas below the avalanche path or as mentioned earlier high traffic on the road in the avalanche path. Sometimes horizontal terraces are also used in arresting the avalanche in the formation zone (McClung and Schaerer, 2011).

1.6.4 Middle zone structures

In the middle zone, deflectors and snow sheds are generally used for controlling the avalanche flow direction. Deflectors are walls built at an angle to the avalanche flow direction for diverting the avalanche away from the object to be protected. Deflectors are usually 6 to 12 m high, made from reinforced earth, gabion walls, cribs, concrete, or steel. Preferably, the angle between the

direction of an avalanche and the deflector should not exceed 20° for the effective deflection of the avalanche (McClung and Schaerer, 1999).

Snow sheds or galleries are tunnel like structures designed to allow avalanches to pass over them and people and vehicles safely move inside them (Figures 1.12–1.13). They are generally constructed for the protection of railways and highways. Concrete, steel, wood, and combinations of these materials are used for their construction. Sometimes, guiding dams are built on top of the snow sheds to prevent lateral spreading of the avalanches. These snow sheds



Figure 1.12: A 135 m long snow shed at MSP-3 avalanche site, Dhundhi, H.P., India



Figure 1.13: A 120 m long snow shed at MSP-7 avalanche site, Dhundhi, H.P., India

are also a costly solution for mitigating the avalanche threat and this option is exercised only for very important areas.

1.6.5 Runout zone structures

In this zone, generally earthen mounds or retarders, catch dams or arrestors, splitters etc. are used to slow down or arrest the avalanches. Catch dams are built perpendicular to the avalanche flow. In a catch dam, adequate storage capacity and height are the most important factors for the design as shown in Figure 1.14. Splitters are generally used to protect the individual houses, towers, church or some other important building. The apex of the splitter usually has an angle of 60° (McClung and Schaerer, 1999).

Retarders/mounds are obstacles located in avalanche paths to reduce the runout distance by dissipating motion energy of avalanches (Figure 1.15) (Rao, 1985). Retarders are most effective when the avalanches are slow and contain dense snow. The optimum height for the retarders is 5 to 6 m, but heights up to 8 m might be needed in areas of deep snow (McClung and Schaerer, 2011). Concrete, local soil or steel is used for the fabrication of these structures. The cost of the

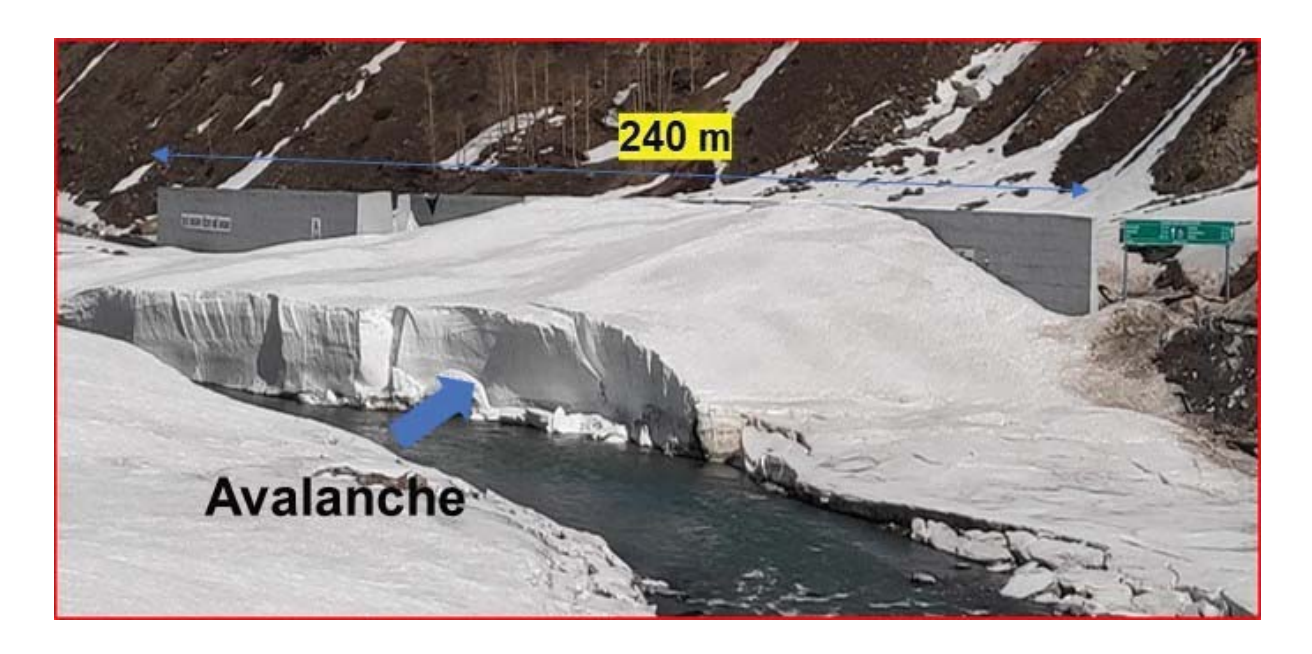


Figure 1.14: A 240 m long and 8 m high catch dam at MNP-3 avalanche site, north portal of Atal tunnel, Himachal Pradesh, India



Figure 1.15: Integrated scheme of earthen mounds and diversion wall used for the protection of Shri Badrinath temple, Uttarakhand, India

runout zone control structures is relatively much lesser as compared to the formation zone or middle zone control structures.

Chapter 2

Literature Review

2.1 Introduction

In order to control the avalanche in the various zones as mentioned in Chapter 1, different avalanche control structures like snow bridges, snow rakes, snow net structures, snow gallery, diversion wall, catch dam, mounds, wedge etc. are installed in various zones of the avalanche depending upon the terrain conditions and the infrastructure to be protected. It is already seen that cost of these structures is very high and so, it is not possible to install these structures at any avalanche path. However, with the increasing human activities in the mountains all over the world, controlling avalanches with full certainty is slowly becoming a necessity. It can be accepted that controlling avalanches through the structure measures is still the most certain method which provides almost 100 % safety to the humans and the infrastructures. In the light of this, significance of providing optimum design of these structures becomes very high. This may help in the near future in employing the structural control measures at a large number of avalanche sites with minimum efforts, cost and time. In the present work, since the objective is to enhance the understanding on the dynamic effects of the avalanches, focus is given on only middle zone and runout zone avalanche control structures. As mentioned earlier, in order to have optimum design of middle zone and runout zone avalanche control structures, accurate knowledge of avalanche impact pressures, flow depth, shear forces, normal forces and velocity etc. is vital. These parameters can be either obtained from measurements or through avalanche dynamics models. In this line of action, different researchers have carried out the work, in the field of 1-D, 2-D and 3-D modelling of avalanche dynamics and interaction with structures/obstacles using a number of different techniques under large varying conditions of snow and terrain conditions. Parallelly, a large number of experimental studies also been carried out by the various researchers for the estimation of the significant avalanche flow parameters

mentioned above. But there are a lot of research gaps in these past studies which need to be identified and addressed with more work. With this motivation, it was decided to carry out the extensive literature survey in the field of avalanche dynamics and interaction with the obstacles with a special focus on the dense flow of snow avalanches, estimation of avalanche impact pressures by actual interaction with the obstacles, estimation of dynamic coefficient of friction of snow and other associated parameters.

2.2 Literature survey

The complete literature survey is given in the following sections 2.2.1–2.2.3.

2.2.1 Avalanche dynamics models

Voellmy (1955) developed a simple and practical 1-D avalanche dynamics model. This was the pioneering work in this field. This model is based on the two important parameters; Coulomb dynamic friction coefficient μ_k and the turbulent friction coefficient ξ . The model estimates velocity, runout distance and impact pressures and is simple to use in the practical applications. However, in this model, there is a need to choose a mid-slope reference position for the computation of terminal velocity and runout distance. Results depend on where the reference is located. In order to overcome this limitation, Perla, Cheng, and McClung (1980) derived a 1-D differential equation for the centre of mass of an avalanche with the condition that the only logical reference is the starting position of the avalanche. In this work, analogous to Voellmy (1955) model, numerical solutions depend critically on two parameters; a friction coefficient μ_k and a dynamic resistance parameter M/D, which is the ratio of avalanche mass M to dynamic drag D. However, main limitation of this model is its mathematical redundancy. Due to this reason, even with the availability of complete velocity data for a given path, it is not possible to compute uniquely how μ_k and M/D vary on the given avalanche path. Hungr and McClung (1987) showed that an alternative runout equation for debris flows given by Takahashi and Yoshida (1979), which accounts for transfer of momentum and thrust between the main body of the debris wave and the frontal part which moves into the runout zone, can be easily adapted to snow avalanches within the context of the Voellmy model. Authors demonstrated that this proposed equation estimates runup height against the barriers, more accurately as compared to

the Voellmy equation for the computation of runup height. However, there is a need to verify this equation against field measurements. Nohguchi (1989) proposed a 3-D model for the motion of the mass centre of an avalanche over an arbitrary surface. Author demonstrated that avalanche paths over complex topography are very sensitive to small differences in the avalanche velocity. However, implementation of this model to the real avalanche conditions was not provided. Salm, Burkard, and Gubler (1990) presented the improved version of the Voellmy (1955) model popularly known as Voellmy-Salm (V-S) model. This model has been embedded in Swiss Guidelines for the avalanche runout zone calculations. The main contribution by the authors was adding snow fracture depth calculations and simplification of the computation procedure of the equations. V-S model has been used by a number of engineers in the mountains for the practical applications e.g., Kocyigit and Gurer (2007) applied the Voellmy-Salm model to compute the velocity and runout distance of avalanches that occurred in Uzungol, a village in Turkey. However, authors perceived that the validity of this model to other avalanche tracks in Turkey needs to be established. Salm (1993) presented further development of that used in the Swiss Guidelines by demonstrating that shearing in avalanche movement is concentrated near the ground and that, due to the geometrical roughness of the ground, a flow resistance proportional to the square of velocity must be taken into account in addition to dry friction. McClung and Mears (1995) presented an improved version of Swiss Guidelines for the calculation of avalanche runup and runout distance. This method applies only to the cases in which initial flow depth, velocity etc. are known in the runout zone of the avalanche.

Due to incapability of the PCM and Voellmy-Salm center of mass models to simulate transient behavior of the avalanches at any point on the avalanche path, a number of researchers explored depth-averaged or Saint-Venant shallow water equations for the development of avalanche dynamics models (Brugnot and Pochat, 1981; Bartelt, Salm, and Gruber, 1999; Satapathy, Keshari, and Kumar, 2009). These models are either 1-D, quasi 2-D or 2-D models. A few researchers attempted to apply the depth-averaged equations based models for the simulation of avalanche flow interaction with the obstacles (Faug, Naaim, and Naaim-Bouvet, 2004; Kattel et al., 2018; Fei et al., 2020). However, these studies were carried out at small-scale only.

Savage and Hutter (1989) improvised the depth-averaged equations by introducing the granular material concepts. Keshari, Satapathy, and Kumar (2010) introduced corrections for vertical velocity variation and density stratification along the snow depth in their 1-D depth-averaged model. This model was tested on a 61 m long snow chute at Dhundhi, Himachal Pradesh, India. The most notable development was done by a team of researchers from SLF Switzerland; Christen, Kowalski, and Bartelt (2010), who presented the computer model RAMMS, as a practical tool for the avalanche engineers. This model solves the 2-D depth-averaged equations governing avalanche flow with second-order accurate numerical solution schemes in a real mountain terrain. Authors have considered snow entrainment also in this model. Presently, simulation of avalanche flow interaction with the structures is not fully taken into account in this tool. It should be mentioned here that most of the researchers have used Voellmy-fluid as the basis in their depth-averaged models.

Due to limitations of both the mass-block models and depth-averaged equations to model vertical velocity and pressure variations along the depth of the avalanche, another group of researchers explored the development of Navier-Stokes (N-S) equations based models. Some of the prominent studies are elaborated here. A group of researchers; Lang and Martinelli (1979), Lang, Dawson, and Martinelli 1979 (a, b) and Dent and Lang (1980) developed 2-D numerical, finite difference computer programs based on the Navier-Stokes equations to give avalanche runout distance, velocity of the leading edge of the avalanche and depth of debris in the runout zone. These models treat snow as a Newtonian fluid and work on the basis of two friction coefficients, i.e., kinematic viscosity v as coefficient of internal friction and surface friction coefficient as Coulomb dynamic friction coefficient μ_k . On similar lines, Norem, Irgens, and Schieldrop (1989) developed non-steady two-dimensional shear together with the use of a finitedifference programme to calculate snow-avalanche velocities and flow heights in the runout zone. However, authors considered no-slip velocity in their model computations. Dent and Lang (1983) developed a modified Bingham numerical model and tested for the simulation of the motion of snow avalanches. This two-dimensional, incompressible model takes the form of a two-viscosity system in which a large viscosity is employed in the low stress regions of the flow and a smaller viscosity is used in the high stress regions. Model and test results for velocity, run

out distance and debris distribution agreed. However, it was noticed from the results that a lot of trailing snow debris mass was found in the simulations while in the tests it was not. This is most probably due to employing no-slip boundary condition by the authors in their model. Bovet et al. (2007) and Bovet, Chiaia, and Preziosi (2010, a) applied the level set method coupled with the Navier-Stokes equations, suitable for free boundary problems to snow avalanches. In their model, they considered a domain composed by air and snow, having different densities and viscosities. Both Newtonian and non-Newtonian Bingham fluid rheology for snow was explored by the authors in their simulations. However, authors considered arbitrary 2-D domain in this study and provided validation of the model with a small set of experimental data. Further, slipvelocity model details were not provided. As an improvement over this work, Oda et al. (2011) applied a 2-D two-phase flow model to simulate snow avalanche motion with the consideration of snow as a Bingham fluid. Authors compared their model results with measured values of snow viscosity, impact force and runout distance and debris deposition. Authors also gave details for the slip-boundary condition used in their model. Although the numerical method was able to predict the flow behavior of snow avalanche reasonably well, treatment of the bottom surface lacked objectivity and needs further investigation. On similar lines, Aggarwal and Kumar (2012) presented a 2-D Eulerian multiphase model of snow and air based on the application of Navier-Stokes equations. With this model, authors demonstrated the simulation of avalanche flow and its interaction with catch dam type obstacle for a 61 m long snow chute at Dhundhi, India. Snow was considered as a bi-viscous Bingham fluid. This model used a large number of assumptions. Further, validation was not done with the sufficient experimental data. Following a different approach, Domnik and Pudasaini (2012) presented a fully two-dimensional, novel Coulombviscoplastic sliding model, which includes some basic features and observed phenomena in dense granular flows like the exhibition of a yield strength and a non-zero slip velocity. However, the model is quite complex and difficult to apply in the real field conditions. As a step further in this direction, Oda et al. (2014) and Romanova (2017) explored the applications of two-phase flow models to simulate the avalanche motion corresponding to real avalanche events. Avalanche was considered as a turbulent two-phase flow of snow and air. Authors took snow as non-Newtonian incompressible Bingham fluid or Herschel-Bulkley fluid model and air as a

Newtonian fluid. There is a need to validate these models with more case studies. Domnik et al. (2013) developed an innovative multiscale strategy to couple the full two-dimensional, non-depth-averaged model with a one-dimensional, depth-averaged model for the dense flow of avalanches. With the coupled model, in regions with smooth changes, depth- averaged model was used and in regions where depth-averaging becomes inaccurate, like in the initiation and deposition regions and particularly, when the flow hits an obstacle or a defence structure, Navier-Stokes equations based model was employed. This coupled model gave good results but needs to be tested in the large scale avalanches. Utilizing the features of this model and that of Domnik and Pudasaini (2012) model, Khattri et al. (2018) simulated interaction of flowing mixture of snow and viscous liquid with an obstacle in a small arbitrary domain. However, authors did not discuss avalanche interaction with unsymmetric obstacles.

With an objective, to obtain certain recompenses in terms of accurate modelling of rheology of flowing snow and resolution of computation difficulties, parallel to the development of depthaveraged and Navier-Stokes equations based avalanche dynamics models, a few snow Scientists are working on the application of the advanced computation techniques such as, Smoothed Particle Hydrodynamics (SPH), Moving Particle Semi-implicit (MPS), Material Point Method (MPM) and Discrete Element Modelling (DEM) techniques for the development of avalanche dynamics models. SPH is a computational fluid dynamics (CFD) mesh-free Lagrangian technique which is a useful feature for the full 3-D modelling of complex geometries. It solves Navier-Stokes equations over several discrete points which move according to the flow field. MPS is also a mesh-free Lagrangian technique similar to SPH but it can handle discontinuous kernel function also. To overcome disadvantages of purely Lagrangian methods and Eulerian methods, a Material Point Method (MPM) is introduced. MPM is a hybrid Eulerian-Lagrangian approach, which uses Lagrangian particles to track mass, momentum and deformation gradient, and adopts an Eulerian background mesh to solve and update the motion of the particles. In Discrete Element Method (DEM) model is based on the analysis of the motion of individual solid particles as compared to continuum bulk fluid approach. A few notable studies are elaborated here. A group of researchers, Lachamp et al. (2002) and Abdelrazek, Kimura, and Shimizu (2014, 2016) applied the SPH numerical method to simulate snow avalanches and other

granular materials and their interaction with the obstacles. Simulated results were compared with small-scale experiments and found in agreement. Saito et al. (2012) explored the viability of applying the MPS method to avalanches. Authors introduced the constitutive equations of Bingham fluid, dilatant fluid and the erosion-deposition process in the model and found results in agreement with the observations and experiments. Teufelsbauer et al. (2011) presented a 2-D DEM model for simulating dry granular avalanche and impact forces on the rigid obstacles in a small domain. Simulations carried out using the commercial software PFC3d were found in agreement with experiments. However, there is a need to validate this methodology in the real avalanche domain. Solowski et al. (2015), Stabilini (2019) and Li et al. (2020) calibrated and validated the Material Point Method (MPM) with laboratory experiments as well as real-scale avalanches in the 2-D domain. Using the proposed numerical approach, distinct behaviors of snow avalanches, from fluid-like to solid-like, were examined with varied snow mechanical properties. It can be noted that most of these studies have been done in the 2-D domain or on small-scale. So, it is quite challenging to extend SPH, MPS, DEM and MPM techniques to the 3-D real mountain terrain for the simulation of avalanches because of their complexity and high computational requirements.

Besides the above mentioned studies, a large number of review studies have also been carried out by a number of researchers in the field of modelling of avalanche dynamics; the prominent studies being done by Brugnot (1987), Nguyen and Boger (1992), Nettuno (1995), Harbitz (1998), Sauermoser and Illmer (2002), Salm (2004), Borstad (2005), Pudasaini and Hutter (2007) and Nishimura, Barpi, and Issler (2021). These studies mainly describe the brief history of development of snow avalanche dynamics models, uncertainties in relation to the physical assumptions made in the models and contribution of avalanche dynamics studies for reducing risk for settlements and infrastructure. Further, these review studies highlight strengths and limitations of the various approaches used for the avalanche dynamics models and further scope of improvement. An important deduction from these studies is that an increase in complexity of the dynamics models does not necessarily mean an increase in the accuracy of the simulations or a better hazard mitigation strategy.

To summarize, center of mass models and depth-averaged equations based avalanche dynamics models are relatively simple and computationally fast. For this reason, these models

are still used by a large number of practitioners in the mountain regions. On the other hand, Navier-Stokes equations based models are based on more accurate Physics and can simulate flow over sharp jumps, irregularities and interaction with the obstacles. However, these models are computationally more demanding. A hybrid application of depth-averaged and N-S equations based models seems to be an optimum solution. Recently, mesh-free techniques like SPH, MPM, and MPS are being applied for the development of avalanche dynamics models. These techniques convert continuum fluid to particles and can handle large deformations as compared to Eulerian mesh based techniques. However, these methods are computationally much more demanding and sometimes convergence problems also occur in the solution. Another advanced technique DEM which solves the motion of discrete particles and their collisions, is also being explored for the development of avalanche dynamics models. This method is more suited for modelling the motion of dry cohesionless snow. However, this method is complex to apply practically in the real mountain terrain and computationally very demanding.

2.2.2 Avalanche impact pressure, drag coefficient, and the associated parameters

Assessment of accurate avalanche impact pressures is a vital requirement for the optimum design of middle zone and runout zone avalanche control structures in the snow bound avalanche prone areas of the world. A large number of studies have been done in the past for the assessment of the avalanche impact pressures on the obstacles. In this regard, one of the most popular and oldest avalanche dynamics models in the world is by Voellmy (1955). This model approximates the avalanche impact pressure on the obstacles from the snow velocity value calculated analytically. The model is simple in the application but did not account for the unusual snow properties. Later, based on the small-scale experiments on snow blocks, Furukawa (1957) proposed an empirical equation for the estimate of the avalanche impact pressures. The equation evaluates maximum impact pressure on a structure neglecting its geometry and flow regime. After this, a large number of studies have been done on the small-scale snow chutes or slides for the modeling and measurements of avalanche impact pressure and allied parameters. Some of the prominent studies are elaborated here, e.g., Pedersen, Dent, and Lang (1979) proposed an equation for the prediction of avalanche impact forces on an 0.6 m high rectangular obstacle

based on the simulations through a modified 2-D computer code SMAC solving Navier-Stokes equations. Difference between the experimental results and the computer simulation was found in the order of $\approx 21\%$. However, authors did not elaborate on the choosing of particular values of snow properties in their model. Lang and Dent (1980) estimated avalanche impact force on instrumented rectangular obstacle made of balsa wood (0.3 m wide and 0.05 m high) through the combined application of 2-D numerical tools, AVALNCH and SMAC. Measured and simulated impact force values were found in agreement. However, corresponding impact pressures were not mentioned. Using the 2-D program code SMAC, Mead et al. (1986) simulated the impulse force on an instrumented vertical barrier considering snow as Newtonian fluid and a bi-viscous Bingham fluid. Authors demonstrated that the simulated results were in agreement with the measurements. They found kinematic viscosity as the most important snow property for the simulations. Nakamura et al. (1987) did measurements of avalanche impact pressure and other parameters on a 25 m long and 1 m wide snow chute using six load cells of varying capacities on a 0.823 m high post. Authors proposed two equations for the impact pressure calculation, one based on the normal impact force and second based on the plastic wave theory. The authors observed impact pressure values in the range of 161-358 kPa in a few experiments and corresponding values by the model based on plastic wave theory in the range of 45–203 kPa for the snow blocks hitting at a speed of about 12 m s⁻¹. Eglit, Kulibaba, and Naaim (2007) proposed an analytical model for impact pressures on an arbitrary obstacle that takes into account the snow compressibility effects. Authors proposed two equations of state for low-density and highdensity flows. Authors estimated ratio of pressure behind the shock to that of pressure in front of the shock for dense avalanches varied from 1.0 to 1.5. However, experimental validation of the proposed theory is missing. Hauksson et al. (2007) conducted a series of laboratory experiments on a 7.5 m long and 0.35 m wide chute, with glass beads of mean particle size 90 µm and bulk density $\approx 1500 \text{ kg m}^{-3}$, in order to investigate impact forces on narrow rectangular and cylindrical obstacles for rapid supercritical granular flow. The authors obtained substantially lower values of the dynamic drag coefficient as compared to the values used in case of traditional guidelines (Salm, Burkard, and Gubler, 1990) for the rectangular obstacles which needs further investigation. Oda et al. (2011) applied Bingham fluid model to simulate 2-D snow avalanche motion for an 8 m long and 0.8 m wide experimental chute facility.

Authors compared the simulated avalanche impact forces and other parameters with the measured values and found in agreement with each other. However, treatment of bottom surface needs further investigation. Aggarwal and Kumar (2012) simulated avalanche impact pressures for a 61 m long snow chute geometry but not validated with the measurements. Parallel to the small-scale studies, a large number of impact pressure studies have been done at the real scale. For e.g., Salway (1978) monitored a few real avalanche events at Roger Pass with seismic geophones placed in its track. Author measured impact pressures using four load cells, each having surface area of 645 mm², fitted on a stand and placed perpendicular to the avalanche flow. Further, correlations between the seismic and pressure signals enable approximate velocities within an avalanche to be estimated. Based on these impact pressure and velocity measurements, the author estimated effective drag coefficient in the range 2-6. McClung and Schaerer (1985) measured avalanche impact pressures at Rogers Pass in the Selkirk Mountains of British Columbia using five 645 mm² disc-shaped surface load cells mounted on a 5.2 m high steel frame. For the sake of comparative study, a large circular aluminum plate 0.5 m in diameter was also used for the impact measurements. From the analysis of the data, the authors found that the large plate gives lower avalanche impact pressure values by roughly an order of magnitude for the wet avalanches and in the order of magnitude of 2 for the moist avalanches. This is probably due to larger sized particles in the wet snow. Sovilla et al. (2008) analyzed the avalanche impact pressures, flow velocity and flow depths of five Vallee de la Sionee measurements for the dry and wet snow avalanches. The measurements were done on a 20 m high tubular pylon. Peak impact pressure values in the range of 50-800 kPa were noted in the measurements. Further, based on the impact pressure and velocity measurements, authors estimated the effective drag coefficient. Sovilla, Schaer, and Rammer (2008) reported impact pressures of eight snow avalanches measured at the Swiss avalanche test site Vallee de la Sionne. Measured pressures were compared to the existing Swiss calculation procedure. Authors concluded that the existing calculation formulas are not able to properly reproduce the measured pressure values. Faug et al. (2010) proposed a simplified 3-D analytical model for the prediction of avalanche impact forces under the steady state conditions and found results in agreement with two real sites. However, it is observed in reality that avalanche forces are highly transient in nature. So, this aspect needs further investigation. Baroudi, Sovilla, and Thibert (2011) measured

impact pressures of dry and wet snow avalanches at the Swiss Valle'e de la Sionne experimental test site using piezo and cantilever sensors. They found that the measured impact pressures can be up to eight times higher than the hydrostatic snow pressure in wet cohesive slow avalanches and are highly dependent on sensor geometry. Based on the wet snow experiments carried out at Valle'e de la Sionne on 20 m high tubular pylon, Sovilla et al. (2016) obtained avalanche impact pressures in the range of 50-500 kPa. Authors found that that for wet snow avalanches, total impact pressure is sum of inertial and gravitational components. Maggioni et al. (2019) performed avalanche impact pressure measurements on a 2.7 m high rectangular instrumented obstacle at Seehore set-up situated in Aosta Valley, Italy. Based on the five avalanche events, authors found average impact pressures in the range of 2–30 kPa. Recently, Kyburz et al. (2022) developed a granular model based on the 3-D discrete element method (DEM) numerical scheme for assessing the response of an avalanche with a rigid body and the variation of impact pressure with the shape and size of the body. Authors took circular, rectangular and triangular obstacles for the model studies. Further, authors obtained simulated impact pressures in the range of 50-500 kPa and found in agreement with the previous experimental results. A few studies have also been done for the reconstruction of the avalanche impact pressure applied on the obstacles from the deformations recorded during the impact (Thibert et al., 2008; Baroudi and Thibert, 2009; Bovet et al., 2011; Thibert et al., 2013).

From the above literature survey, it is found that a large number of studies have been done for the measurement and modelling of avalanche impact pressures on a small-scale and real-scale. However, none of these studies are complete in nature and there is no general avalanche impact pressure model till date for the estimation of impact pressures on different kinds of structures. Further, it is understandable that elaborate measurements of avalanche impact pressures with good repeatability, at a large number of real avalanche sites using different sizes of the obstacles and the sensors is really difficult. This is due to the large spatial variability in the snow properties, avalanche sizes, extents of the avalanche terrains in the order of a few kilometers, dangerous nature of avalanches and involvement of large resources (Sovilla et al. 2020). So, based on the limited measurements, it is not possible to develop a comprehensive model for the calculation of avalanche impact pressures on the obstacles. Further, scatter is found in the drag coefficients construed analytically from these real-scale pressure measurements. The

back-analysis techniques for the estimation of avalanche impact pressures on the houses, buildings etc., are valuable only in case of avalanche accidents (De Biagi, Chiaia, and Frigo, 2015; Frigo et al., 2020). However, this problem can be justly solved by doing experiments on a small-scale experimental facility like snow chute, where a large number of 'real avalanche like' experiments can be executed with better accuracy and relative ease, as compared to the experiments on a real terrain. In order to further enhance the development of comprehensive avalanche impact pressure model; there is a need to have a simulation tool, which can simulate avalanche-structure interaction process and pressure distribution on the different geometries of the obstacles, by considering the variable snow properties. A few simulation tools based on the solution of Navier-Stokes equations were developed in the past which modelled the avalancheobstacle interaction process and compared the simulated and experimental values of the avalanche impact pressures (Pedersen, Dent, and Lang, 1979; Lang and Dent, 1980; Mead et al., 1986; Bovet, Chiaia, and Preziosi, 2010, b; Oda et al., 2011; Aggarwal and Kumar, 2012). These avalanche dynamics models are 2-D in nature and did not provide the ample facts for the avalanche-obstacle interaction process. As mentioned earlier, Kyburz et al. (2022) has presented a 3-D model for the simulation of avalanche-obstacle interaction process using a discrete element model. However, in this work, authors have not modelled the avalanche-interaction process by taking into account the actual release of avalanche. They just took a small domain around the obstacle for modeling and let avalanche flow into this domain with a pre-determined velocity. So, there is a lot of possibility for upgrading the avalanche impact pressure studies.

2.2.3 Dynamic coefficient of friction of snow

Although it is apparent that several materials include rheological parameters, there is no material of widespread engineering implication that under normal situations exhibits the mystifying intricacies found in snow (Mellor, 1975). The lack of adequate experimental data for the coefficient of Coulomb dynamic friction for the flowing snow μ_k has caused significant conjecture about the frictional behavior for snow avalanches, involving the true practice of constitutive relationships applied for simulating snow avalanches. Currently, most of the researchers and practitioners across the world are approximating the value of this snow dynamic friction coefficient μ_k through the back-analysis for the real avalanche sites or small-scale snow

chutes by the application of various avalanche dynamics models, for e.g., Schaerer (1975), Martinelli Jr et al. (1980), McClung and Schaerer (1983), Ancey and Meunier (2004), Verma et al. (2004), Kocyigit and Gurer (2007), Naaim et al. (2013), Ligneau, Sovilla, and Gaume (2022), and Sanz-Ramos et al. (2023). However, these studies have dearth of objectivity and the physical basis in the selection of optimal μ_k values. It can be stated here that the real understanding of the flowing avalanches will be feasible only when all major parameters prompting avalanche dynamics models are equally validated with the measurements. Further, the knowledge of shear force and normal force components of a snow avalanche from which the dynamic coefficient of friction μ_k is assessed, is equally important for the design of snow sheds in the mountainous regions. These snow sheds play a vital role in protecting the people and vehicles from the avalanche hazards. A limited number of studies have been done in the past to measure shear and normal force components of the avalanches which lead to the consequent appraisal of the values of μ_k . To elaborate, Casassa, Narita, and Maeno (1989) found values of μ_k by sliding snow blocks over the natural avalanche slopes. They conveyed relatively much higher values of friction coefficient in the range of 0.57 to 0.84, for the snow density ρ_i varying from 60 kg m⁻³ to 340 kg m⁻³; temperature T_s of snow varying from -10.2 °C to -2.2 °C and a large band of snow grains varying from new snow to artificially compacted snow. Gleason (2002) assessed coefficient of static friction in the range of 0.53-1.76, between the snow layers with the aid of a piece of roughened plastic with a known mass fixed on a 10 cm × 10 cm portion of ply board. Temperature T_s of the snow varied from -8.0 °C to -0.5 °C during the experiments. However, author did not provide any evidence for the dynamic coefficient of friction of snow μ_k . Kern, Tiefenbacher, and McElwaine (2004) measured basal shear force and velocity profile on a 34 m long and 2.5 m wide chute. Authors measured the basal snow shear stress on the rubber mats with the piezo force gauges as ≈ 794 kPa. However, authors did not provide any evidence for the μ_k values. From the experiments conducted on a 34 m long snow chute, Tiefenbacher and Kern (2004) appraised effective μ_k for wet snow of mean density $\rho_i \approx 400$ kg m⁻³ on a rubber matted surface as 0.72 from the measured shear force and calculated normal force values. This value is considerably higher due to taking into consideration of the internal friction processes within snow. Further, authors presented the analysis in their research based on a few measurements. Platzer, Bartelt, and Jaedicke (2007) measured shear force, normal force, and coefficient of

dynamic friction μ_k for wet, dry and slush snow flows based on forty two experiments. Authors used force plates of size 0.68 m × 0.68 m, shielded with roughened aluminum sheets in their experiments. They used wet snow of density varying from 380 kg m⁻³ to 597 kg m⁻³; dry snow density varying from 211 kg m⁻³ to 364 kg m⁻³ and slush density varying from 556 kg m⁻³ to 700 kg m⁻³. They did most of the measurements on wet snow and obtained μ_k values in the range of 0.33 to 0.53. Further, they detected that dry snow avalanches have lower μ_k values than the wet avalanches and the slush flows. Authors noted that the measured coefficients of friction are much higher than the Swiss Guideline's suggestions which need further examination. Platzer, Bartelt, and Kern (2007) assessed values of μ_k varying from 0.22 to 0.55 between the dry snow and the rubber mats surface. The authors found the basal shear to be the main frictional behavior accountable for slowing down the avalanche flows. As an important inference from their studies, they did not find the velocity dependency for μ_k values in disparity to several other proposed constitutive models for the basal friction related to the snow avalanches. A few research studies have also been done in the past for the valuation of μ_k between the snow and the ski sliders made of plastic, aluminum, and steel surfaces (Colbeck, 1988; Rohm et al., 2015). In a recent study, Dong et al. (2024) carried out a series of experiments to estimate the shear force, normal force, and dynamic friction coefficient for the rock-ice avalanches. Authors found ice content and melt water as the most noteworthy parameters affecting the values of the dynamic friction coefficient. However, due to large variation in the operating conditions, these studies cannot be entirely applied in the simulation of avalanche flows. So, it can be summarized here that the limited research studies carried out in the past for the assessment of dynamic friction coefficient of snow μ_k are not complete in nature and cannot be used in the simulation of all types of avalanche flows under extensive varying conditions of snow temperature, density, surface type and the avalanche speeds.

2.3 Summary of the literature survey

A number of avalanche dynamics models based on the center of mass, depth-averaged equations and Navier-Stokes equations are in practical use for the estimation of significant avalanche flow parameters, especially for the dense flow of avalanches. These models are being continually updated. Recently, a few avalanche dynamics studies based on the advanced computation

techniques i.e., SPH, MPM, MPS and DEM have been done. It is found that each approach has its merits and demerits. It seems that due to complex dynamic properties of snow, avalanche dynamics models based on only one technique may not suffice, rather hybrid models based on a combination of the above techniques may serve the purpose better. Further, there is a need to develop a comprehensive model for the assessment of avalanche impact pressures on the obstacles/structures. For the validation of this model, measurements on the small-scale seem to be a better choice due to ease in execution and getting better accuracy and repeatability of the data. From the literature survey, it is found that limited measurements on shear force, normal force and dynamic coefficient of friction of snow are available and further experiments are required to generate new database on this important parameter.

Based on the literature survey carried out, a number of specific research gaps were identified in the field of avalanche dynamics and interaction with obstacles for the dense flow of avalanches. To elaborate, it was found that very little research work has been carried out in the areas of; development of 3-D avalanche dynamics model to capture realistic geometry of the terrain and obstacle, taking into account the velocity variation along the depth of the avalanche flow, natural avalanche stopping, simulation of air blast pressures, measurement of avalanche impact pressures on the obstacles and comparing with the model results, effective drag coefficient between the avalanche and the obstacle, coefficient of dynamic friction of snow etc. 3-D modelling is expected to make the appearance of avalanche flow and its interaction with obstacles quite realistic due to simulation of Physics of vertical velocity variations and the lateral spreading of the flowing avalanche. Further, it has been found from the literature that the knowledge of joint interactions between the avalanche flow and the obstacle is crucial to introduce a realistic load case in the structure design and then to use an adapted dimensioning and assessment method. A lot of damage has been reported in the past due to air blast pressures caused by avalanches. So, in order to address the above mentioned gaps, it was decided to develop a 3-D avalanche dynamics model for the investigation of avalanche flow and its interaction with obstacles based on the solution of Navier-Stokes equations. To fulfill this purpose, finding advantages of the small-scale over the real-scale as discussed in the earlier paragraphs, domain of a 61 m long snow chute at Dhundhi, near Manali, H.P., India was selected for the present work. For the validation of the model output, measurements on avalanche

impact pressure, coefficient of dynamic friction, debris distribution, runout distance and velocity parameters were planned on this experimental facility. Specifically, achievement of the following objectives was targeted to address some of the existing research gaps mentioned above:

- ❖ 3-D CFD modelling of avalanche flow using Navier-Stokes equations based multi-phase Eulerian model employing non-Newtonian bi-viscous Bingham fluid rheology. Results to be validated with the experiments in a small-scale experimental facility (*Snow chute, Dhundhi, H.P., India*). Results to be compared with Newtonian fluid rheology. Results also to be compared with the equivalent results obtained using world famous Voellmy-Salm avalanche dynamics model. Air blast pressures will also be simulated.
- ❖ Compile and investigate the data base on shear force and normal force measurements on snow chute, Dhundhi, India and estimate the dynamic coefficient of friction of snow based on this data.
- ❖ Investigation of measurements of avalanche impact pressures on an instrumented catch dam type structure at snow chute, Dhundhi, India. Compare the measurements with the 3-D modelling results. Air blast pressures will also be simulated. Drag coefficient of snow and obstacle will also be estimated using the CFD simulations.
- ❖ Model avalanche flow and interaction with an obstacle along a preferential flow trajectory for a real mountain site.

Chapter 3

Development of a 3-D Avalanche Dynamics Model and its Interaction with the Obstacles

3.1 Introduction

In this chapter, the development of a 3-D avalanche dynamics model is described. This model has been developed by customizing the computational fluid dynamics software ANSYS Fluent with the supplementation of various user-defined functions. This model is a multi-phase Eulerian model, comprising of snow and air phases and it solves the Navier-Stokes equations. The model is able to simulate critical avalanche flow parameters and interaction with the obstacles. Additionally, the model results were compared with the measurements.

3.2 About the study area

The present work is focussed on and around Dhundhi area, which is located at an altitude of 3030 m in the Pir Panjal range of Himachal Pradesh, India. Pir Panjal range of the Indian Himalya experiences heavy snowfall. Famous Beas Kund glaciers, from where the river Beas originates, is just 4.4 km form this place. Defence Geoinformatics Research Establishment (DGRE), one of the premier research laboratories of Defence Research and Development Organization (DRDO), has established one of its main snow and avalanche field research station at this place (Figure 3.1). This research station is located approximately 20 km away from Manali and in the close vicinity of the south portal of the recently opened, 9.02 km long Atal tunnel. This tunnel is an important link on the 498 km long Manali-Leh highway. At this site, the average cumulative seasonal snowfall is about 11 m and the winter air temperature varies from a minimum of -15 °C to a maximum of +10 °C. Till date, at this place, the maximum standing snow has gone up to 4.42 m in year 1998. Generally, seasonal snow fall occurs in this area from November to April and making the winter period. Snow remains dry for a small period and changes quickly to moist/wet snow. Around the station, there are a number of natural avalanche



Figure 3.1: A view of the (a) field research station of DGRE at Dhundhi (b) observatory for recording meteorological parameters and the snowpack information

sites. Most of the avalanches occur at this location during the period of February and March and are of wet snow type. Most of the prominent avalanche sites around Dhundhi have been controlled by means of various avalanche control structures as mentioned in sections 1.6.3–1.6.4 of Chapter 1 of this thesis.

3.3 About the experimental site

All the experimental work reported in the present work has been carried out on a 61 m long and 2 m wide snow chute at Dhundhi, Himachal Pradesh, India. This experimental facility is being used for the measurement of avalanche flow parameters i.e., velocity, impact pressure, dynamic coefficient of friction, runout distance, avalanche debris deposition. The 61 m length of the snow chute was planned keeping in view the satisfactory fluidization of the released snow mass, attainment of significant avalanche velocities, dynamic similarity between the snow chute avalanches and the full-scale avalanches. Further, the availability of a natural mountain slope of about 65 m length near the residential huts, also contributed in fixing this explicit length of the snow chute. The snow chute consists of the five sections as shown in Figure 3.2. The bottom surface of the chute is made of low-carbon steel sheets of thickness 12 mm. Size of each sheet is $2 \text{ m} \times 4 \text{ m}$ for most of the sections of the chute. The side railing of the snow chute is 1 m high and is fitted with transparent polycarbonate sheets. Alternative colours are painted at every 0.5 m interval on the bottom surface of the chute for ease in measurement of the snow flow parameters.

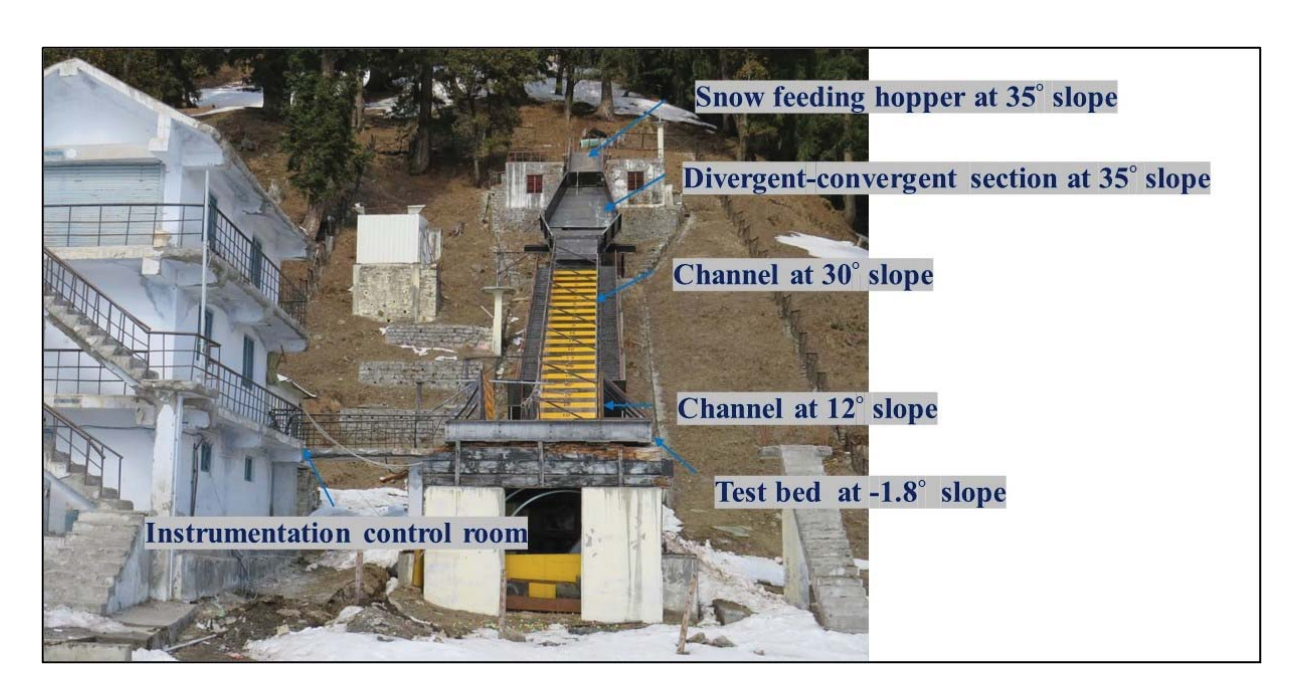


Figure 3.2: A view of the experimental facility, snow chute at Dhundhi, Himachal Pradesh, India

In the present studies, angle of the hopper has been kept secured at 35° . The length of the hopper is 5.5 m and its maximum snow filling capacity V is 11 m^3 . This is comparable to the formation zone of a natural avalanche. At the end of the hopper, a 13.5 m long diverging-converging channel $(2 \text{ m} \times 4 \text{ m tapered})$ inclined at 35° is attached to ensure the fluidization of the snow and acts like an extended portion of the formation zone of an avalanche. After this section, a 22 m long channel inclined at 30° acts as an accelerating track for the snow that acquires maximum velocity near the end of this channel. This is similar to the middle zone of an avalanche. At the end of this section, an 8 m long channel inclined at 12° is provided which warrants drop in the momentum of snow flow. This channel is similar to the runout zone of an avalanche. Finally, a 12 m long test bed inclined at an angle of -1.8° is provided at the end, on which avalanche fully comes to a stop. This section acts like an extended portion of the runout zone of a natural avalanche. So, snow chute dimensions are analogous with the natural avalanche slopes.

3.4 Development of the 3-D avalanche dynamics model

3.4.1 Assumptions in the model

The main assumptions made in the development of present model are as follows:

- i. Both snow and air are considered incompressible.
- ii. Both air and snow are supposed to have laminar flow.
- iii. Air is considered a Newtonian fluid and snow a bi-viscous Bingham fluid.
- iv. In few simulations, for the comparison purpose, snow is made to follow Newtonian fluid rheology.
- v. Angle of repose of snow is equal to its internal friction angle.

3.4.2 Main governing equations

The model mainly solves the multiphase equations for the snow and surrounding atmospheric air phases (Bovet et al., 2007). Here, phase means the inimitable state of matter like solid or fluid. The brief detail of the main flow governing equations is given below (ANSYS Inc., 2015):

The description of multiphase flow includes the concept of phasic volume fractions, denoted here by α_s for snow and α_a for air. Volume fractions characterize the space occupied by each phase, and the laws of conservation of mass and momentum are satisfied by each phase individually.

Air being in much higher quantity than snow, has been considered primary phase 'a' and snow as secondary phase 's'.

The volume V_s of a secondary phase 's' is defined as:

$$V_{\rm s} = \int_{\rm V} \alpha_{\rm s} \, \mathrm{d}V \tag{3.1}$$

where, $\alpha_{a+} \alpha_s = 1$

So, the effective density of phase 's' is $\alpha_s \rho_i$, where ρ_i is the density of the snow phase before impact on the obstacle in kg m⁻³.

Continuity equation

The volume fraction of snow phase is computed from the continuity equation:

$$\frac{\partial}{\partial t}(\alpha_s \rho_i) + \nabla \cdot (\alpha_s \rho_i \vec{v}_s) = 0 \tag{3.2}$$

Here, \vec{v}_s (m s⁻¹) is the velocity vector of snow. The solution of Equation (3.2) for the snow phase along with the condition that the volume fractions sum to one permits for the calculation of the volume fraction of the air.

Fluid-fluid momentum equations

The conservation of momentum for the secondary snow phase 's' is (ANSYS Inc., 2015):

$$\frac{\partial}{\partial t}(\alpha_{s} \rho_{i} \vec{v}_{s}) + \nabla \cdot (\alpha_{s} \rho_{i} \vec{v}_{s} \vec{v}_{s}) = -\alpha_{s} \nabla p + \nabla \cdot \overline{\tau}_{s} + \alpha_{s} \rho_{i} \vec{g} + \vec{R}_{as}$$

$$(3.3)$$

Here, p (N m⁻²) is the hydrodynamic/gauge pressure shared by both the primary and secondary phases, \vec{g} is the acceleration due to gravity in m s⁻². Further, $\bar{\tau}_s$ (N m⁻²) is the phase stress-strain tensor for snow given as (ANSYS Inc., 2015):

$$\bar{\bar{\tau}}_{s} = \alpha_{s} \, \eta_{s} (\nabla \, \vec{v}_{s} + \nabla \, \vec{v}_{s}^{T}) + \alpha_{s} \, \left(\lambda_{s} - \frac{2}{3} \eta_{s}\right) \nabla \cdot \vec{v}_{s} \bar{\bar{l}}$$

$$(3.4)$$

where, η_s (N s m⁻²) and λ_s (N s m⁻²) are shear and bulk viscosity of snow, respectively, and \bar{l} is the unit tensor. Since snow is considered incompressible, $\nabla \cdot \vec{v}_s = 0$ and so the second term vanishes.

In Equation (3.3), \vec{R}_{as} (N m⁻³) is an interaction force between the snow and air phases given as, $\vec{R}_{as} = K_{as}(\vec{v}_a - \vec{v}_s)$, where, K_{as} denotes interphase momentum exchange coefficient measured in kg m⁻³ s⁻¹. In the current work, the symmetric model has been preferred for the calculation of K_{as} as (ANSYS Inc., 2015):

$$K_{as} = \frac{\alpha_a \alpha_s (\alpha_a \rho_a + \alpha_s \rho_i) f}{\delta_{as}}$$
(3.5)

where particulate relaxation time δ_{as} measured in seconds is given as:

$$\delta_{as} = \frac{(\alpha_a \rho_a + \alpha_s \rho_i) \left(\frac{d_{a_+} d_i}{2}\right)^2}{18(\alpha_a \mu_a + \alpha_s \eta_s)} \tag{3.6}$$

Here, f is the drag function given by the following equation (ANSYS Inc., 2015):

$$f = \frac{\omega R_{ee}}{24} \tag{3.7}$$

where ω is the drag coefficient, which is a function of the relative Reynolds number R_{ee} given as (ANSYS Inc., 2015):

$$R_{ee} = \frac{\rho_{sa}|\vec{v}_s - \vec{v}_a|d_{sa}}{\mu_{sa}} \tag{3.8}$$

$$\omega = \left\{ \frac{24(1+0.15R_{ee}^{0.687})}{R_{ee}} \quad for \, R_{ee} \leq 1000 \right.$$

$$= 0.44 \quad for \, R_{ee} > 1000$$
(3.9)

For a symmetric model, mixture density ρ_{sa} (kg m⁻³) is computed from the volume-averaged properties, i.e., $\rho_{sa} = \alpha_a \rho_a + \alpha_s \rho_i$. Mixture viscosity, μ_{sa} (N s m⁻²) is calculated as, $\mu_{sa} = \alpha_a \mu_a + \alpha_s \eta_s$. Here, μ_a (N s m⁻²) is the dynamic viscosity of air.

Here, mixture particle diameter measured in meters is given as, d_{sa} =0.5 (d_a + d_i). As per the symmetric model, for a single dispersed snow phase in the air, the particle diameter of the dispersed phase d_i is equal to the particle diameter of the primary air phase d_a (ANSYS Inc. 2015). With this condition, d_{sa} becomes equal to d_i . Here d_i is set at a value of 10⁻⁵ m for all the current simulations. It is highlighted here that inter-granular collisions, cohesions etc. of snow are neglected in the present model and snow flow is essentially modeled as a continuum fluid. It can be noted that most of the avalanche flow models developed till date have followed the continuum method. Similarly, momentum equation is solved for the primary air phase.

3.4.3 Discretization and numerical solution of the model

A control-volume-based technique was used to convert the mass and momentum Equations (3.2– 3.3) to algebraic equations. Later, these algebraic equations were solved numerically. The control volume technique consists of integrating the above transport equations about each control volume yielding discrete equations that express the conservation law on a control-volume basis. In the current work, pressure-based transient solver has been chosen, as density-based solver is not well-suited with multiphase flows. Pressure-velocity coupling was solved using semi-implicit method for pressure linked equation (SIMPLE) algorithm (Patankar, 2009). For spatial discretization, first-order upwind scheme was chosen in which face value is set equal to the cellcenter value in the upstream cell. Since the mesh is hexahedral and aligned with the flow, selection of first-order scheme is realistic. For the computation of the gradients, least square cellbased gradient approach was used in which the solution is expected to vary linearly. Multi-fluid volume of fraction (VOF) model has been used along with the Eulerian model for the interface sharpening between the snow and air phases (Hirt and Nichols, 1981). For the explicit mode of calculation of volume fraction of snow and air phases, geometric reconstruction interpolation scheme was opted to enable sharp interface between the phases. Further, the Geo-Reconstruct scheme warrants time-accurate transient behavior of the VOF solution. For transient part of the

momentum equations, first order implicit formulation was preferred.

3.4.4 Solver parameters for the simulations

Computation time-step ε for all the simulations was uniformly taken as 0.001s. The under-relaxation factors for the pressure, density, body forces and momentum were taken as 0.3, 1.0, 1.0 and 0.7, respectively. The convergence criteria for the solution was set with a residual value of 0.001 for both continuity and momentum equations. The value of acceleration due to gravity \vec{g} was taken as 9.81 m s⁻². After this, the equations were initialized, snow phase patched with VOF value equal to 1.0 and the simulations run. The solution for the several parameters i.e., pressure, velocity, volume fraction etc. was automatically saved at regular intervals.

3.4.5 Domain, boundary conditions and the material properties

The 3-D geometry of the snow chute, Dhundhi was drawn in the ANSYS Workbench module by taking into account the total computation domain size as 73 m long, 2 m wide and 5 m high as shown in Figure 3.3 (ANSYS Inc., 2015). It is to be noted here that the actual length of the snow

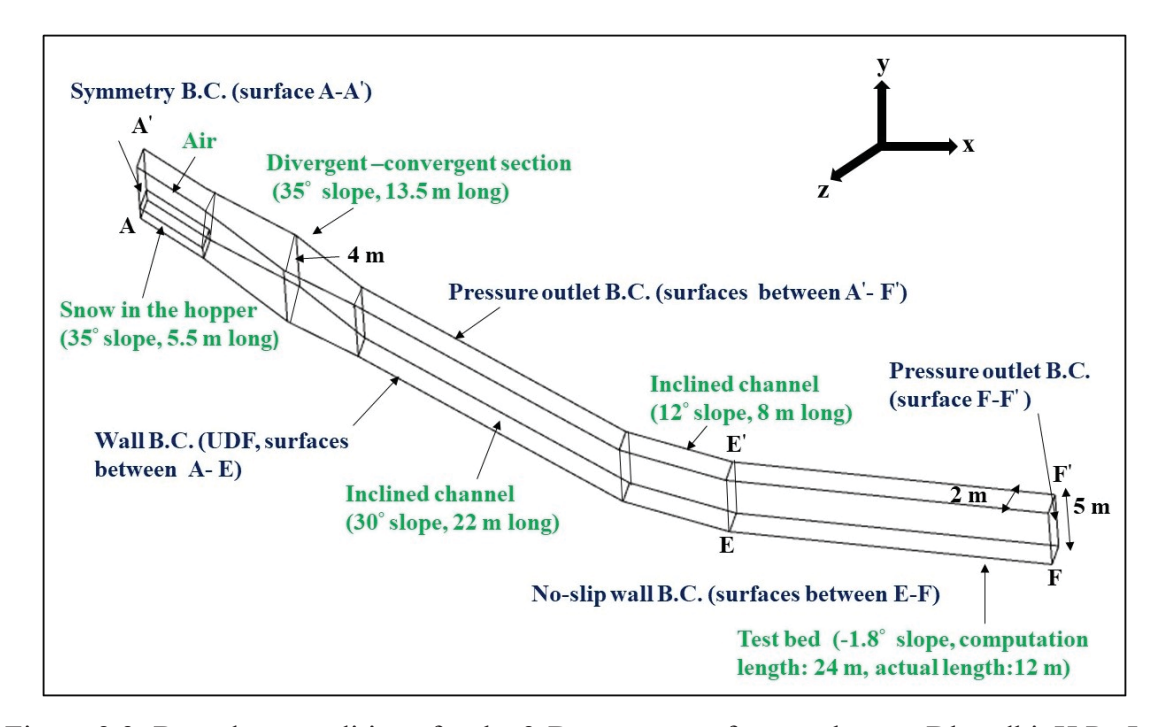


Figure 3.3: Boundary conditions for the 3-D geometry of snow chute at Dhundhi, H.P., India

chute is 61 m long. The computation domain of the chute was taken longer than the actual size to contain the simulations beyond the runout distance of 12 m. At the start of snow flow (A-A'), symmetry boundary condition was applied i.e., wall with zero shear stress. At the arbitrary drawn top surface, which is open to atmosphere, pressure outlet boundary condition was applied. At the end section of the chute also, pressure outlet boundary condition was applied. At the bottom surfaces of the snow chute except the test bed surface, user defined wall shear function was applied, the detail of which is given in the next paragraph. At the test bed surface (E-F), the noslip boundary condition was applied, as friction is maximum in the deceleration zone (Nishimura and Maeno, 1989).

3.4.5.1 Wall shear stress model

The no-slip boundary condition, in which the slip-velocity is set to zero, is widely and successfully used in many fluid flow simulations. However, a number of studies in the past have demonstrated that snow being a granular material moves with a slip-velocity at the snow-ground interface (Bovet et al., 2007; Upadhyay, Kumar, and Chaudhary, 2010; Domnik and Pudasaini, 2012). An innovative model for the calculation of wall slip-velocity has been presented by Domnik, and Pudasaini (2012). However, it was found difficult to implement this model in the current code as it requires values of x and y-components of the wall shear stress at the wall to substitute the no-slip boundary condition. Therefore, in this paper, a simple mathematical model for accounting wall slip in the x and y-directions is presented (Figure 3.4). Taking value of the wall shear stress in the z-direction as zero as the variation of avalanche flow parameters is predominantly in the x and y-directions, total wall shear stress $\tau_{s|wall}$ (N m⁻²) at the snow and chute-bottom interface along the chute flow is given below (Lang and Brown, 1980):

$$\tau_{s|wall} = (1 - W_s) \eta_s \left(\frac{\partial u}{\partial y} + \frac{\partial v}{\partial x} \right) \tag{3.10}$$

Here, W_s can be defined as the wall slip factor whose value can vary from 0 to 1. The value of W_s = 0 implies minimum slip and maximum wall shear stress values. In case of no-slip fluid wall condition, maximum wall shear stress is present. Dynamic Coulomb friction coefficient μ_k can be computed as the ratio of the snow wall shear stress $\tau_{s|wall}$ and the snow hydrodynamic pressure p

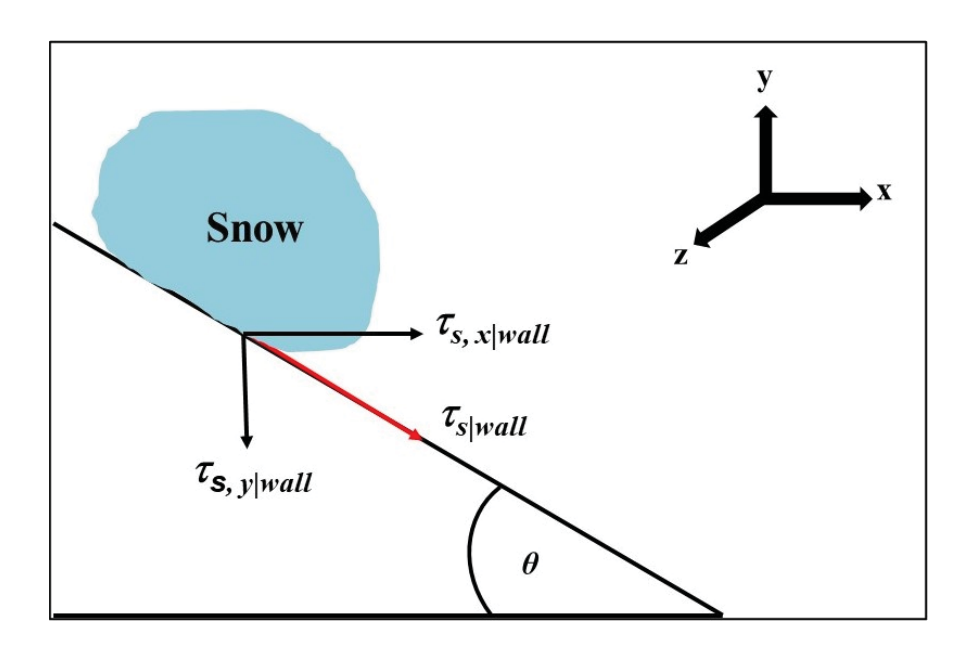


Figure 3.4: Wall shear stress components of snow on an inclined plane (here, $\tau_{s|wall}$ (N m⁻²) stands for the total wall shear stress of snow; $\tau_{s, x|wall}$ (N m⁻²) stands for the x-component of $\tau_{s|wall}$; $\tau_{s, y|wall}$ (N m⁻²) stands for the y-component of $\tau_{s|wall}$ and θ is the angle of the plane in degrees)

Here, $p = \rho_i g h_s$, where h_s is the simulated depth of the snow. So, for a constant p value at a point, it can be deduced that maximum Coulomb friction exists whenever maximum fluid wall shear stress condition is reached. With a similar analogy, $W_s = 1$ corresponds to zero wall shear stress and can be termed as maximum slip or free-slip wall condition. In this case, Coulomb friction is also zero. Values of W_s between 0 to 1 will regulate the intermediate slip at the snow& chute-bottom interface. Since program code involves components of wall shear stress in x, y, and z-directions, resolving $\tau_{s|wall}$ into x and y components, x-component of wall shear stress is given as:

$$\tau_{s,x|wall} = (1 - W_s) \,\eta_s \left(\frac{\partial u}{\partial y} + \frac{\partial v}{\partial x}\right) cos\theta \tag{3.11}$$

Similarly, y-component of the wall shear stress is given as,

$$\tau_{s,y|\text{wall}} = -(1 - W_s) \, \eta_s \left(\frac{\partial u}{\partial y} + \frac{\partial v}{\partial x} \right) \sin \theta \tag{3.12}$$

Here, θ is the angle of the slope to be used in radians. In the current work, for all the model simulations, the value of W_s is taken as 0.25. With this value, average value of the simulated dynamic Coulomb coefficient of friction between the snow chute steel surface and the snow

was estimated as 0.12. The simulated friction coefficient value is in agreement with the measurements by Aggarwal et al. (2024) who obtained the average measured value of dynamic Coulomb coefficient of friction μ_k between the snow chute steel surface and snow as 0.113. It is for this particular reason that a specific value of W_s was taken for all the simulations. On opting values of W_s other than 0.25 in the Equations 3.11–3.12, the agreement between the simulated friction coefficient and the measured values deviated significantly.

3.4.5.2 Physical properties of snow and air

The properties of air were taken constant with dynamic viscosity μ_a as 1.7894×10^{-5} N s m⁻² and density ρ_a as 1.225 kg m⁻³. Snow which is a highly intricate and dynamically fluctuating material, has been assumed as bi-viscous Bingham fluid. The constitutive equation of an ideal Bingham fluid is made up of two parts. First, if the shear stress intensity τ (N m⁻²) is below a yield stress value τ_0 (N m⁻²), no deformation takes place and material behaves as a rigid solid. Second, if τ is above this value, deformation takes place and is proportional to the amount that τ exceeds τ_0 (Figure 3.5). This model is difficult to implement because of sharp discontinuity at $\tau = \tau_0$. To

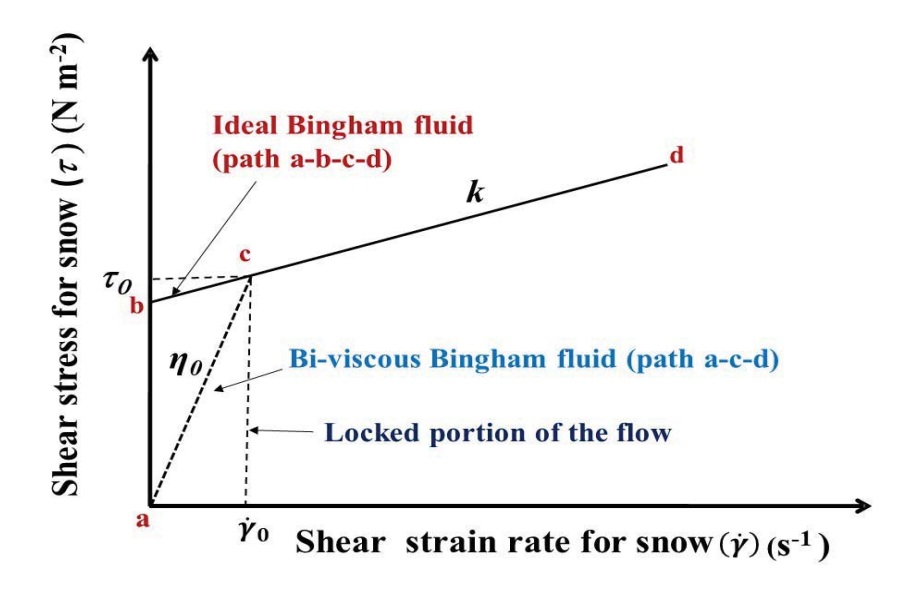


Figure 3.5: Flow rheology of snow as a bi-viscous Bingham fluid (here, τ_0 (N m⁻²) stands for the yield strength of snow; η_0 (N s m⁻²) stands for the dynamic viscosity of snow in the locked portion of the flow; k (N s m⁻²) stands for the dynamic viscosity of snow after the yield region and $\dot{\gamma}_0$ (s⁻¹) stands for the shear strain rate of snow in the locked portion of the flow)

correct this anomaly, in this paper, bi-viscous Bingham fluid model has been adopted from Dent and Lang (1982, 1983) which allows small deformations to take place according to a linear viscous flow law in the locked portion of the flow as shown by a dotted line in Figure 3.5. Theoretically, the dynamic viscosity in this region should be infinite due to very low strain rates. However, to avoid singularity, following the work of Oda et al. (2011), the dynamic viscosity η_0 used in this region was assumed a huge value of 10^4 N s m⁻². However, Oda et al. (2011) applied pure Bingham fluid model, which does not allow any strain rate in the locked region and so applied even higher values for η_0 i.e. in the order of 10^8 N s m⁻², in their research work. Further, in the current work, during the trial simulations, it was noted that for η_0 values beyond 10^4 N s m⁻², there was negligible change in the results. Following the work of Dent and Lang (1983), Alexandrou et al. (2003), and Oda et al. (2011), the effective Newtonian viscosity of snow η_8 for a bi-viscous Bingham fluid can be written as:

$$\eta_{\rm S} = \frac{\tau_0}{\dot{\gamma}} + k \left(1 - \frac{\dot{\gamma}_0}{\dot{\gamma}} \right) \tag{3.13}$$

where, $\dot{\gamma}$ (s⁻¹) is the shear strain rate after the yield region. k (N s m⁻²) is dynamic viscosity coefficient of snow after the yield region. In the present work, the value of k is taken as 0.02 N s m⁻² for all the simulations (Domnik and Pudasaini, 2012). This value is justified as snow flows like a Newtonian fluid with quite low viscosity after the yield region. Here, $\dot{\gamma}_0$ (s⁻¹) is strain rate in the locked flow regime which is computed as:

$$\dot{\gamma}_0 = \frac{\tau_0}{\eta_0} \tag{3.14}$$

The yield strength of snow, τ_0 is the function of hydrodynamic/gauge pressure p, cohesion strength, c and internal friction angle of snow, φ as written below (Oda et al., 2011):

$$\tau_0 = c + p \tan \varphi \tag{3.15}$$

In the current work, cohesion, c between snow grains is neglected. Substituting Equation (3.15) into Equation (3.13), η_s can be re-written as:

$$\eta_{s} = \frac{p \tan \varphi}{\dot{\gamma}} + k \left(1 - \frac{\dot{\gamma}_{0}}{\dot{\gamma}} \right) \tag{3.16}$$

 $\dot{\gamma}$ is related to the second invariant of rate of deformation tensor, $\overline{\overline{D}}$ as:

Chapter 3: Development of 3-D Avalanche Dynamics Model and its Interaction with the Obstacles

$$\dot{\gamma} = \sqrt{\frac{1}{2} \; \overline{\overline{D}} : \overline{\overline{D}}} \tag{3.17}$$

On simplification and after algebraic operations, Equation (3.17) in three-dimensional form is:

$$\dot{\gamma}^2 = 2\left(\frac{\partial u}{\partial x}\right)^2 + 2\left(\frac{\partial v}{\partial y}\right)^2 + 2\left(\frac{\partial w}{\partial z}\right)^2 + \frac{\partial u}{\partial y}\left(\frac{\partial u}{\partial y} + \frac{\partial v}{\partial x}\right) + \frac{\partial u}{\partial z}\left(\frac{\partial u}{\partial z} + \frac{\partial w}{\partial x}\right) + \frac{\partial v}{\partial z}\left(\frac{\partial v}{\partial z} + \frac{\partial u}{\partial y}\right) + \frac{\partial v}{\partial z}\left(\frac{\partial v}{\partial z} + \frac{\partial u}{\partial z}\right) + \frac{\partial w}{\partial z}\left(\frac{\partial w}{\partial z} + \frac{\partial u}{\partial z}\right) + \frac{\partial w}{\partial z}\left(\frac{\partial w}{\partial z} + \frac{\partial u}{\partial z}\right) + \frac{\partial w}{\partial z}\left(\frac{\partial w}{\partial z} + \frac{\partial u}{\partial z}\right) + \frac{\partial w}{\partial z}\left(\frac{\partial w}{\partial z} + \frac{\partial u}{\partial z}\right) + \frac{\partial w}{\partial z}\left(\frac{\partial w}{\partial z} + \frac{\partial u}{\partial z}\right) + \frac{\partial w}{\partial z}\left(\frac{\partial w}{\partial z} + \frac{\partial u}{\partial z}\right) + \frac{\partial w}{\partial z}\left(\frac{\partial w}{\partial z} + \frac{\partial w}{\partial z}\right) + \frac{\partial w}{\partial z}\left(\frac{\partial w}{\partial z} + \frac{\partial w}{\partial z}\right) + \frac{\partial w}{\partial z}\left(\frac{\partial w}{\partial z} + \frac{\partial w}{\partial z}\right) + \frac{\partial w}{\partial z}\left(\frac{\partial w}{\partial z} + \frac{\partial w}{\partial z}\right) + \frac{\partial w}{\partial z}\left(\frac{\partial w}{\partial z} + \frac{\partial w}{\partial z}\right) + \frac{\partial w}{\partial z}\left(\frac{\partial w}{\partial z} + \frac{\partial w}{\partial z}\right) + \frac{\partial w}{\partial z}\left(\frac{\partial w}{\partial z} + \frac{\partial w}{\partial z}\right) + \frac{\partial w}{\partial z}\left(\frac{\partial w}{\partial z} + \frac{\partial w}{\partial z}\right) + \frac{\partial w}{\partial z}\left(\frac{\partial w}{\partial z} + \frac{\partial w}{\partial z}\right) + \frac{\partial w}{\partial z}\left(\frac{\partial w}{\partial z} + \frac{\partial w}{\partial z}\right) + \frac{\partial w}{\partial z}\left(\frac{\partial w}{\partial z} + \frac{\partial w}{\partial z}\right) + \frac{\partial w}{\partial z}\left(\frac{\partial w}{\partial z} + \frac{\partial w}{\partial z}\right) + \frac{\partial w}{\partial z}\left(\frac{\partial w}{\partial z} + \frac{\partial w}{\partial z}\right) + \frac{\partial w}{\partial z}\left(\frac{\partial w}{\partial z} + \frac{\partial w}{\partial z}\right) + \frac{\partial w}{\partial z}\left(\frac{\partial w}{\partial z} + \frac{\partial w}{\partial z}\right) + \frac{\partial w}{\partial z}\left(\frac{\partial w}{\partial z} + \frac{\partial w}{\partial z}\right) + \frac{\partial w}{\partial z}\left(\frac{\partial w}{\partial z} + \frac{\partial w}{\partial z}\right) + \frac{\partial w}{\partial z}\left(\frac{\partial w}{\partial z} + \frac{\partial w}{\partial z}\right) + \frac{\partial w}{\partial z}\left(\frac{\partial w}{\partial z} + \frac{\partial w}{\partial z}\right) + \frac{\partial w}{\partial z}\left(\frac{\partial w}{\partial z} + \frac{\partial w}{\partial z}\right) + \frac{\partial w}{\partial z}\left(\frac{\partial w}{\partial z} + \frac{\partial w}{\partial z}\right) + \frac{\partial w}{\partial z}\left(\frac{\partial w}{\partial z} + \frac{\partial w}{\partial z}\right) + \frac{\partial w}{\partial z}\left(\frac{\partial w}{\partial z} + \frac{\partial w}{\partial z}\right) + \frac{\partial w}{\partial z}\left(\frac{\partial w}{\partial z} + \frac{\partial w}{\partial z}\right) + \frac{\partial w}{\partial z}\left(\frac{\partial w}{\partial z} + \frac{\partial w}{\partial z}\right) + \frac{\partial w}{\partial z}\left(\frac{\partial w}{\partial z} + \frac{\partial w}{\partial z}\right) + \frac{\partial w}{\partial z}\left(\frac{\partial w}{\partial z} + \frac{\partial w}{\partial z}\right) + \frac{\partial w}{\partial z}\left(\frac{\partial w}{\partial z} + \frac{\partial w}{\partial z}\right) + \frac{\partial w}{\partial z}\left(\frac{\partial w}{\partial z} + \frac{\partial w}{\partial z}\right) + \frac{\partial w}{\partial z}\left(\frac{\partial w}{\partial z} + \frac{\partial w}{\partial z}\right) + \frac{\partial w}{\partial z}\left(\frac{\partial w}{\partial z} + \frac{\partial w}{\partial z}\right) + \frac{\partial w}{\partial z}\left(\frac{\partial w}{\partial z} + \frac{\partial w}{\partial z}\right) + \frac{\partial w}{\partial z}\left(\frac{\partial w}{\partial z} + \frac{\partial w}{\partial z}\right) + \frac{\partial w}{\partial z}\left(\frac{\partial w}{\partial z} + \frac{\partial w}{\partial z}\right) + \frac{\partial w}{\partial z}\left(\frac{\partial w}{\partial z}\right) + \frac{\partial w}{\partial z}\left(\frac{\partial w}{\partial z}\right) + \frac{\partial w}{\partial z}\left(\frac{\partial w}{\partial$$

where u, v and w are the velocities in x, y and z-directions, respectively. A user defined function was written for Equation (3.16) and was used in the main program code.

Recently, based on a large number of measurements, Aggarwal (2022) developed a correlation between the average density of snow ρ_i (kg m⁻³) and the angle of repose of snow β (degree). The Equation (3.19) established in this work has been used to estimate the angle of repose of snow for different densities of snow measured in the experiments.

$$\beta = -13.24 \ln(\rho_i) + 117.69 \tag{3.19}$$

For granular cohesionless snow, angle of repose of snow β is fundamentally same as its internal friction angle φ (Al-Hashemi and Al-Amoudi, 2018). With this inference, internal friction angle of snow φ was estimated.

3.4.6 Mesh size dependence

The accessible hardware for running the simulations had 48 GB RAM and two Intel Xenon ® CPU X5660@2.8GHz processors (*each processor having six cores*). The program code utilizes ten cores of the workstation in the parallel computing mode. One of the simulations cases was selected for determining the optimum mesh size for the simulations. To commence with, a hex mesh of size 0.025 m was selected for the mesh generation, which could not be created due to dynamic memory allocation error. Then the mesh size was increased to 0.05 m, 0.1 m etc. Afterwards, keeping the computation time-step ε and all other parameters identical, the simulations were run for the different mesh sizes. For reference, comparison between the simulated snow velocity v_{δ} contours for the three mesh sizes at a flow time-step t = 1.5 s is given in Figure 3.6 (a–c). The complete information with different mesh sizes is given in Table 3.1. From Table 3.1, it is apparent that with the increase in mesh size, there is decrease in the

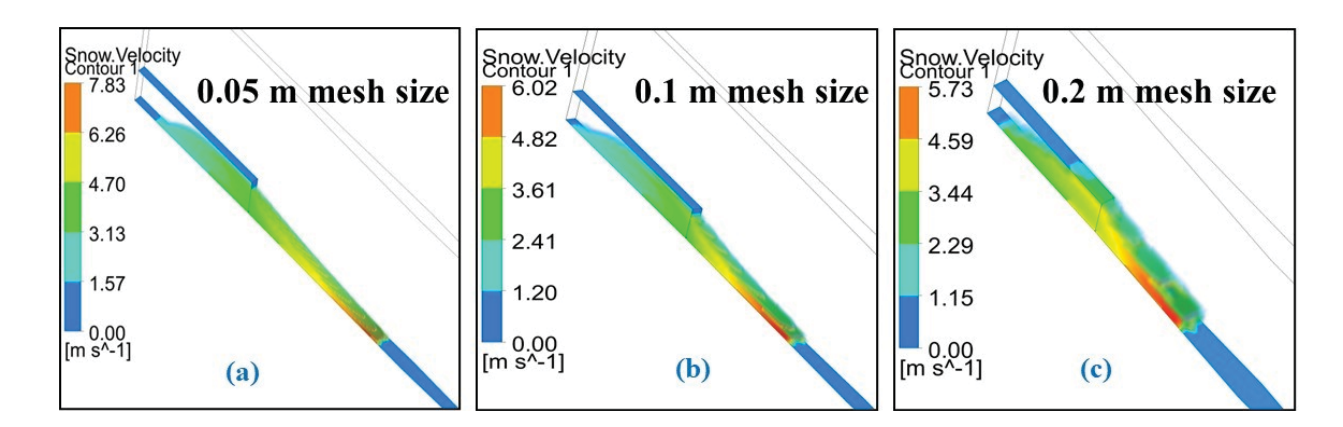


Figure 3.6: Simulated contours of snow velocity v_s at a time-step t=1.5 s, after the release of equal volume of snow from the hopper of the snow chute, Dhundhi, H.P., India and also keeping all other input conditions same, except varying the mesh sizes as (a) 0.05 m (b) 0.1 m (c) 0.2 m

Table 3.1: Effect of varying mesh size on the model simulations

Mesh size (m)	Maximum aspect ratio	Minimum orthogonal quality	Number of cells	Estimated time taken to complete the full simulation (hours)	Simulated max. snow velocity $v_{s, max}$ at $t=1.5$ s (m s ⁻¹)			
0.025	Memory allocation error while generating the mesh							
0.050	3.3220	0.8106	5792000	322.09	7.83			
0.10	3.3205	0.8110	724000	8.22	6.02			
0.20	3.3169	0.8118	90750	3.20	5.73			

computation time but simultaneously there is increase in the nonconformity in the simulated maximum snow velocity v_s , max values with respect to the mesh size of 0.05 m. Further, it can be noted that there is a substantial nonconformity between the computation flow time for the 0.05 m mesh size and others but the nonconformity between the v_s , max values and the deformation pattern, in case of 0.05 m and 0.1 m mesh sizes is not very noteworthy. So, as a trade-off between accuracy and the computation time, mesh size of 0.1 m was chosen for all the simulations reported in this thesis.

3.5 Experiments on snow chute, Dhundhi, and corresponding model simulations for significant avalanche flow parameters

For carrying out experiments on the snow chute, snow was put inside the hopper by shoveling from the neighboring unobstructed region. Further, it was confirmed that snow layers were cut in such a manner so as to ensure the uniformity of the snow type. In case of all of the simulations executed in this work, average snow density, ρ_i for the snow occupied inside the hopper was taken, that was quantified using a snow cylindrical sampler and an electronic weighing machine. The value of uncertainty in the ρ_i was found as \pm 5.0 %. Avalanche debris depth d_s was determined by a meter rod strutted at left most, center and right most points of the debris after a gap of each 1 m length towards the avalanche flow path. The value of uncertainty in d_s was found as \pm 5.0 %, as depicted by error bars in the figures to be discussed in the later paragraphs. Before the start of each experiment, other significant snow parameters like temperature of snow T_s , grains type etc. were noted. Every experiment was initiated after unlocking the hopper gate. Afterward, snow starts flowing down the chute under the effect of gravity. The brief detail of the experiments carried out during the period 2018-2020 on snow chute, Dhundhi is given in Table 3.2. Corresponding CFD simulations were performed by taking into account the 3-D geometry of the snow chute, Dhundhi as described earlier in Figure 3.3. In case of one of the experiments conducted on 5 March, 2018, observed snow avalanche mass variation at various time steps is shown in Figure 3.7. The corresponding simulation was performed for this experiment as shown in Figure 3.8, depicting the variation of simulated snow avalanche mass at the same time-steps. It can be noted from the simulated result that at a time-step t=4.5 s, avalanche flow starts retarding and at t=8 s, velocity of the snow v_s tends to almost zero and avalanche debris is formed. Further, for this case, the point-wise comparison between the observed and the simulated avalanche debris depth d_s at the test bed of the snow chute is shown in Figure 3.9. It should be noted here that for the point-wise comparison, only central values of the debris are considered. It can be observed that snow starts depositing earlier in the experiment with respect to the simulated snow mass. Overall, there is an agreement among experimental and simulated debris profiles.

Table 3.2: Summary of the experiments for finding significant avalanche flow parameters at snow chute, Dhundhi, Himachal Pradesh, India

Date of experiment	Amount of snow in the hopper, $V(m^3)$	Avg. snow density in the hopper, ρ _i (kg m ⁻³)	Snow type ^a	ISCG ^a code	Avg. avalanche debris density, ρ _f (kg m ⁻³)	Status of obstacle in the avalanche Path
4 March, 2018	5.5	467	Melt forms	MFcl	523	No obstacle
5 March, 2018	11	602	Melt forms	MFcl	662	No obstacle
7 March, 2018	5.5	462	Melt forms	MFcl	568	1 m high × 2 m wide catch dam type obstacle
21 February, 2019	11	280	RG	RGlr	339	No obstacle
25 February, 2019	11	332	RG	RGlr	398	No obstacle
25 Jan, 2020	11	207	RG	RGlr	300	1 m high × 2 m wide catch dam type obstacle

Note: "Fierz et al. (2009). The international classification for seasonal snow on the ground



Figure 3.7: Observed snow avalanche mass at various time-steps t of the flow during the experiment on 5 March, 2018 at snow chute, Dhundhi, H.P., India

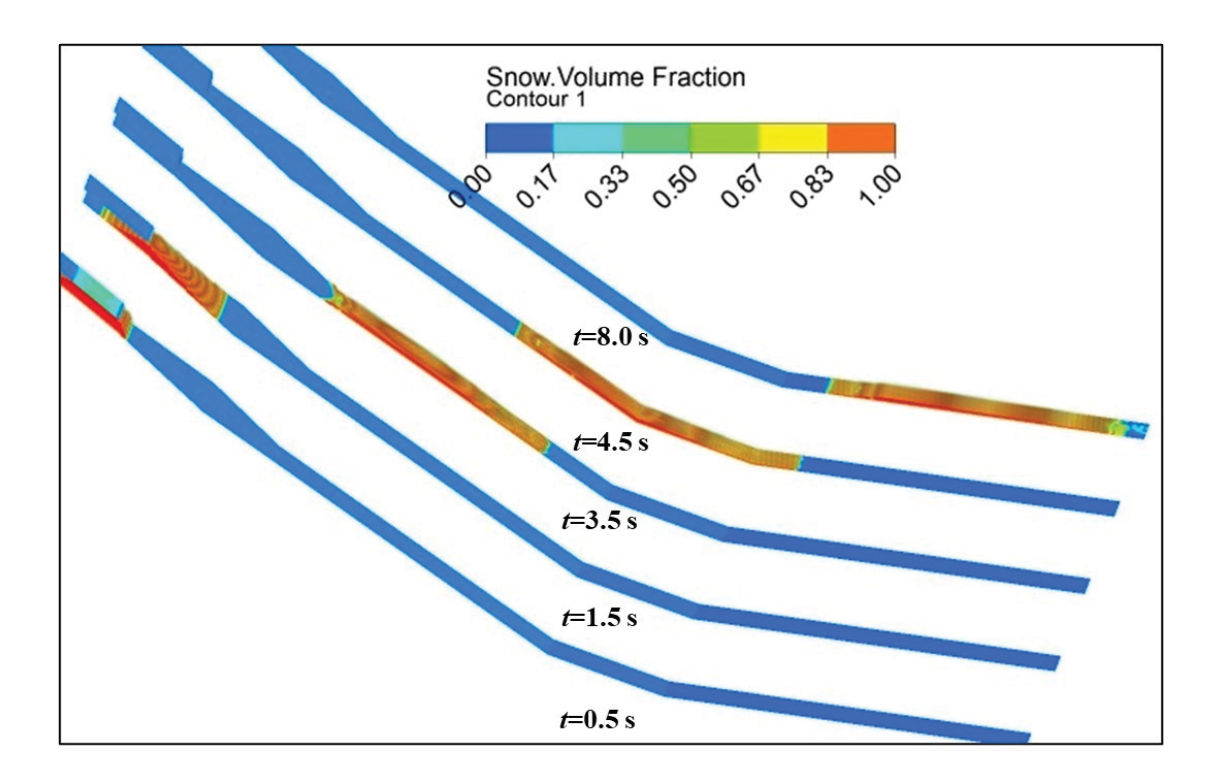


Figure 3.8: Simulated contours of snow avalanche mass corresponding to the experiment on 5 March, 2018 at snow chute, Dhundhi

The root mean square error (RMSE) between the observed and simulated d_s values is 0.167. The mean reason for the discrepancy between the experimental and simulated values is that snow is simulated as a bi-viscous Bingham fluid while in reality; snow is having combined behavior of solid granules and the fluid. Consequently, stopping and elongating behavior of the flowing snow is different in the observed case as compared to the simulation.

In Figure 3.10 (a), considering snow as a Newtonian fluid with dynamic viscosity as 0.02 Pa s, simulation of avalanche flow velocity v_s at various time-steps t is shown. It can be seen that at t=4.5 s, avalanche mass is moving at $v_s \approx 18$ m s⁻¹ and is ready to move out of the snow chute domain. However, contrary to this, when snow was simulated as a bi-viscous Bingham fluid, it starts retarding at a time-step of t=4.5 s and beginning to form the avalanche debris as shown in Figure 3.10 (b). So, it is clear from these results that snow as a Newtonian fluid does not stop on the test bed in contrary to actually observed in the experiments. So, no avalanche debris is

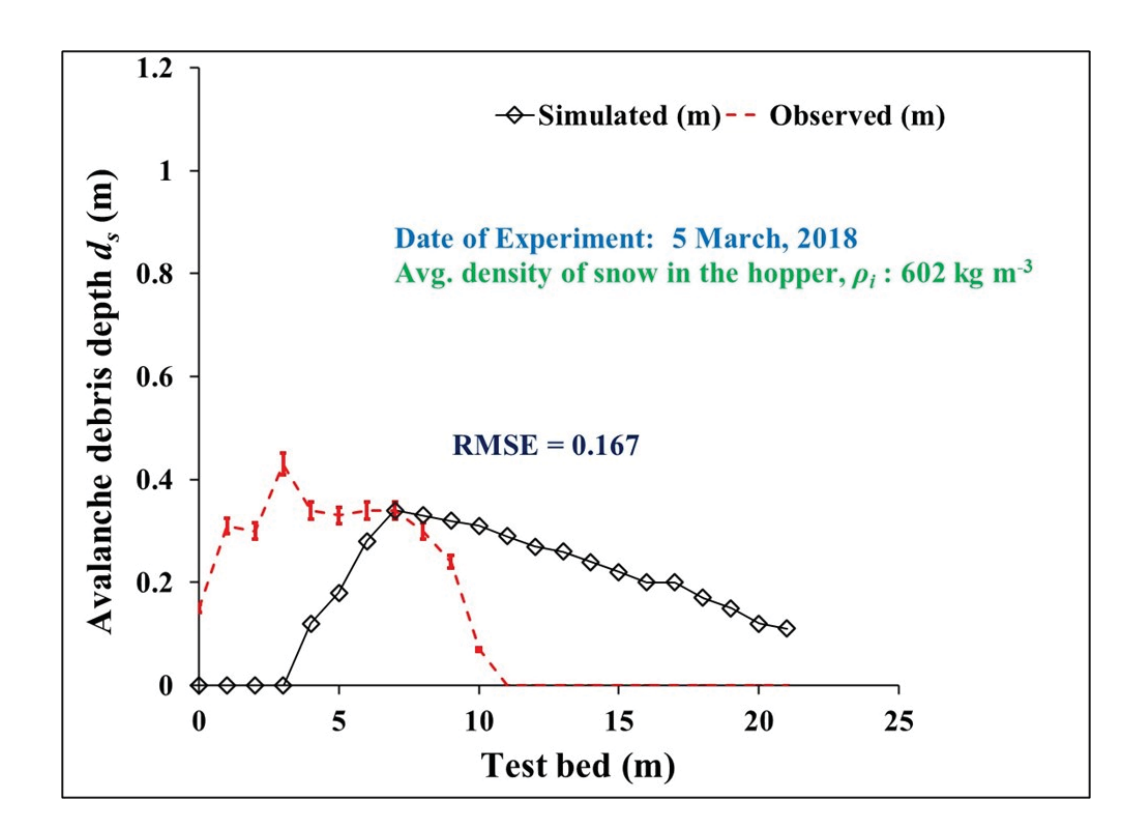


Figure 3.9: Point-wise comparison between the observed and simulated snow avalanche debris depth d_s for the experiment on 5 March, 2018 at snow chute, Dhundhi

formed in this case. This indirectly proves that a Newtonian fluid cannot capture accurately the avalanche flow rheology. It should be noted here that from this point onwards, snow is modelled as a bi-viscous Bingham fluid only in all the simulations presented in the thesis.

Similar to the experiment conducted on 5 March, 2018, point-wise comparison between the observed and the simulated avalanche debris depth d_s , in case of other experiments, is shown in Figures 3.11–3.15. It can be seen from the results that there is significant match between the observed and the simulated values of d_s . Further, it can be noted that this agreement is better when obstacle is present in in the path of the avalanche.

Duration of snow flow time t from the hopper to test bed section till the avalanche debris is formed, varied in the range of 8.0-8.5 s in all the simulations that is in accordance with the real duration of flow movement, as noted from the experiments which is $\approx 7.5-8.5$ s.

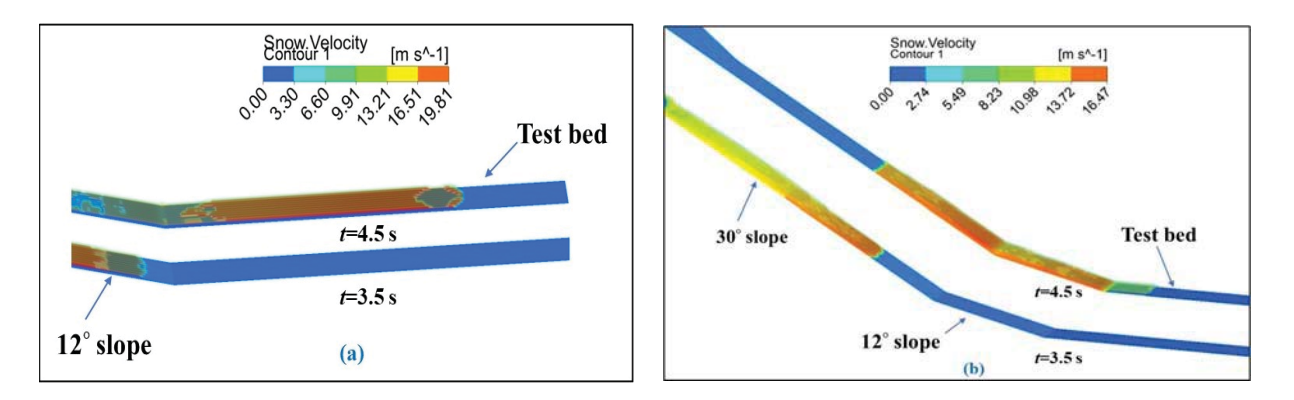


Figure 3.10: Simulation of snow velocity near the test bed of the snow chute, Dhundhi corresponding to the experiment on 5 March, 2018, when snow is assumed as a (a) Newtonian fluid (b) bi-viscous Bingham fluid

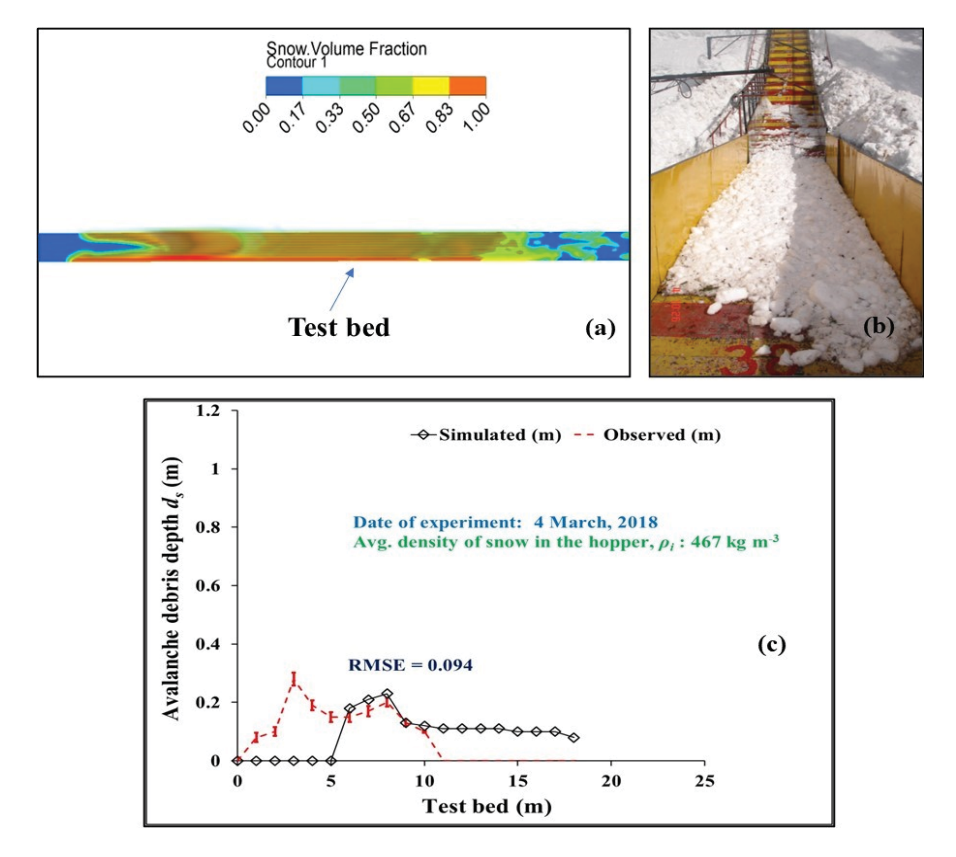


Figure 3.11: Profile of snow avalanche debris depth d_s for the experiment on 4 March, 2018 at the test bed area of the snow chute, Dhundhi (a) simulated (b) observed (c) observed vs. simulated point-wise data

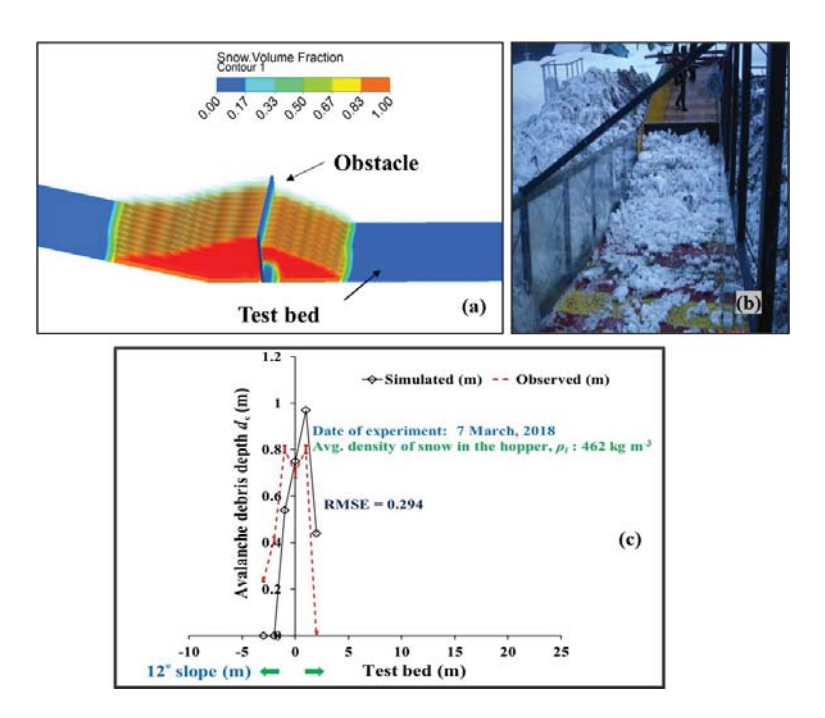


Figure 3.12: Profile of snow avalanche debris depth d_s for the experiment on 7 March, 2018 at the test bed area of the snow chute, Dhundhi (a) simulated (b) observed (c) observed vs. simulated point-wise data

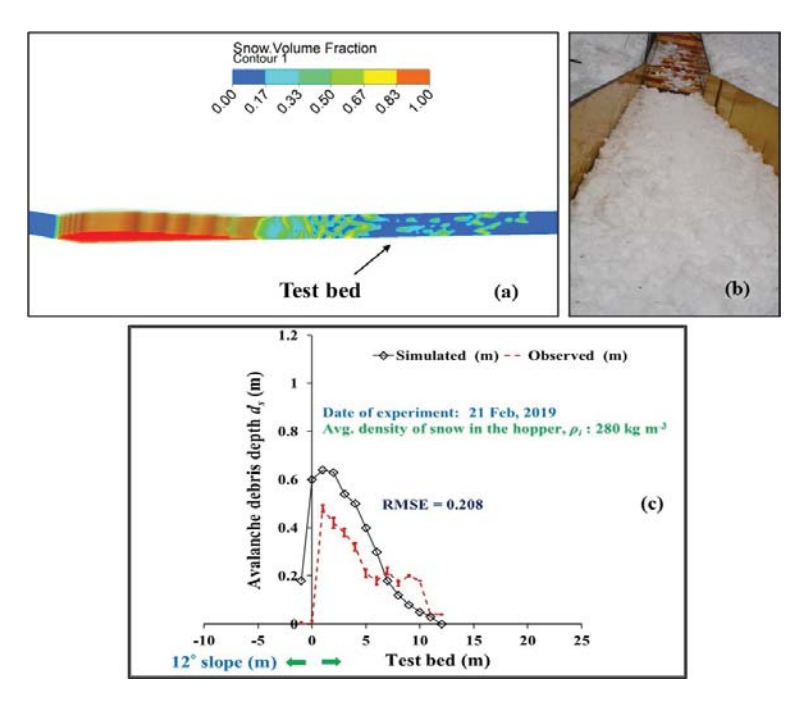


Figure 3.13: Profile of snow avalanche debris depth d_s for the experiment on 21 Feb, 2019 at the test bed area of the snow chute, Dhundhi (a) simulated (b) observed (c) observed vs. simulated point-wise data

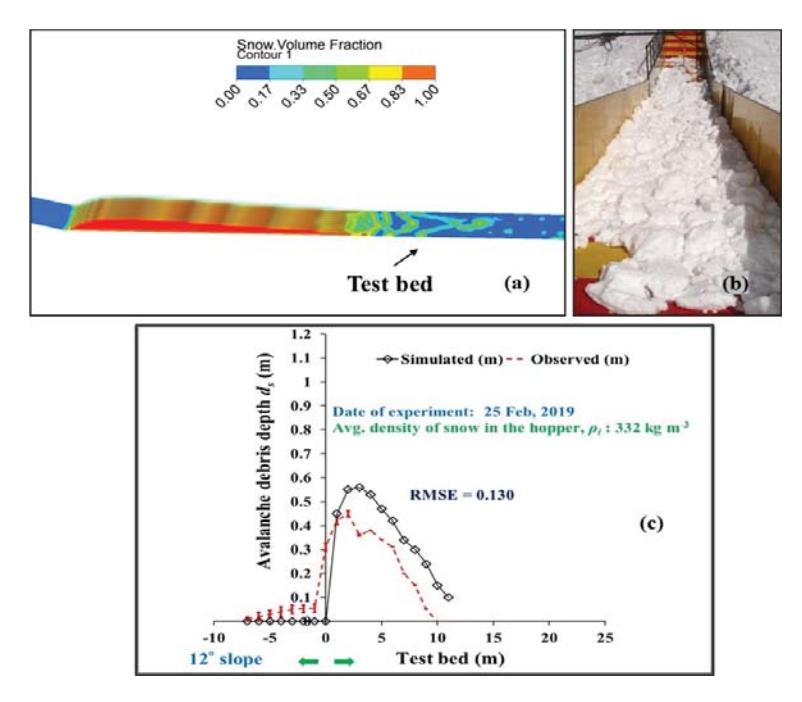


Figure 3.14: Profile of snow avalanche debris depth d_s for the experiment on 25 Feb, 2019 at the test bed area of the snow chute, Dhundhi (a) simulated (b) observed (c) observed vs. simulated point-wise data

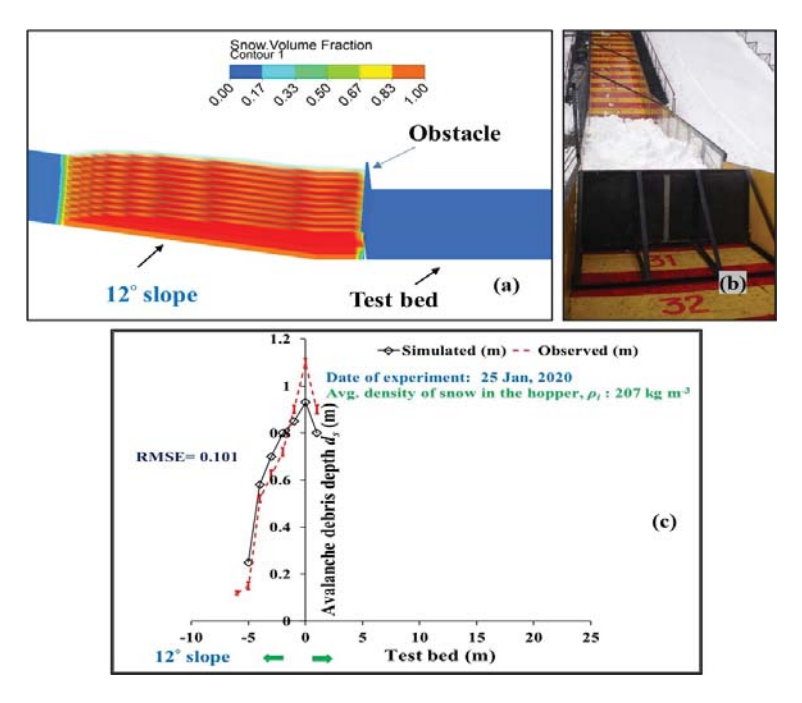


Figure 3.15: Profile of snow avalanche debris depth d_s for the experiment on 25 Jan 2020 at the test bed area of the snow chute, Dhundhi (a) simulated (b) observed (c) observed vs. simulated point-wise data

Figure 3.16 depicts the variation of simulated avalanche velocity at various time-steps t. In order to evaluate the performance of the present model, simulated avalanche front velocity v_{fr} at the end of 12° slope of the chute was extracted from the simulated results, for all the experiments conducted as per Table 3.2. Afterwards, these values were compared with the estimated avalanche front velocities from the video recordings of the experiments and the Voellmy-Salm model as shown in Figure 3.17. v_{fr} was assessed from the video movies recorded through a 16 MP camera for the experiments conducted mentioned previously. Just to elaborate, flow was paused in the videos and time to travel the distance marked with alternate colors at 1 m interval was noted. So, this distance and time ratio gave the average v_{fr} values. For computation of v_{fr} in case of Voellmy-Salm model, paper by Salm, Burkard, and Gubler (1990) was referred.

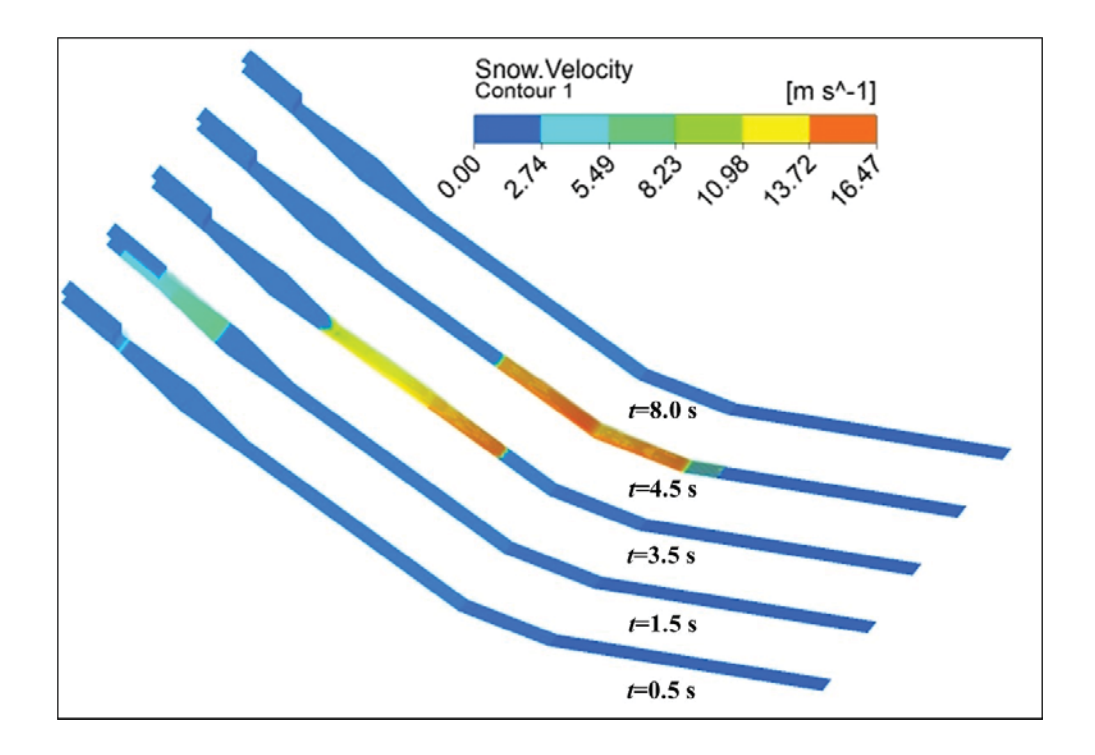


Figure 3.16: Simulation of snow velocity v_s at different time steps t for the experiment conducted on 05 March, 2018

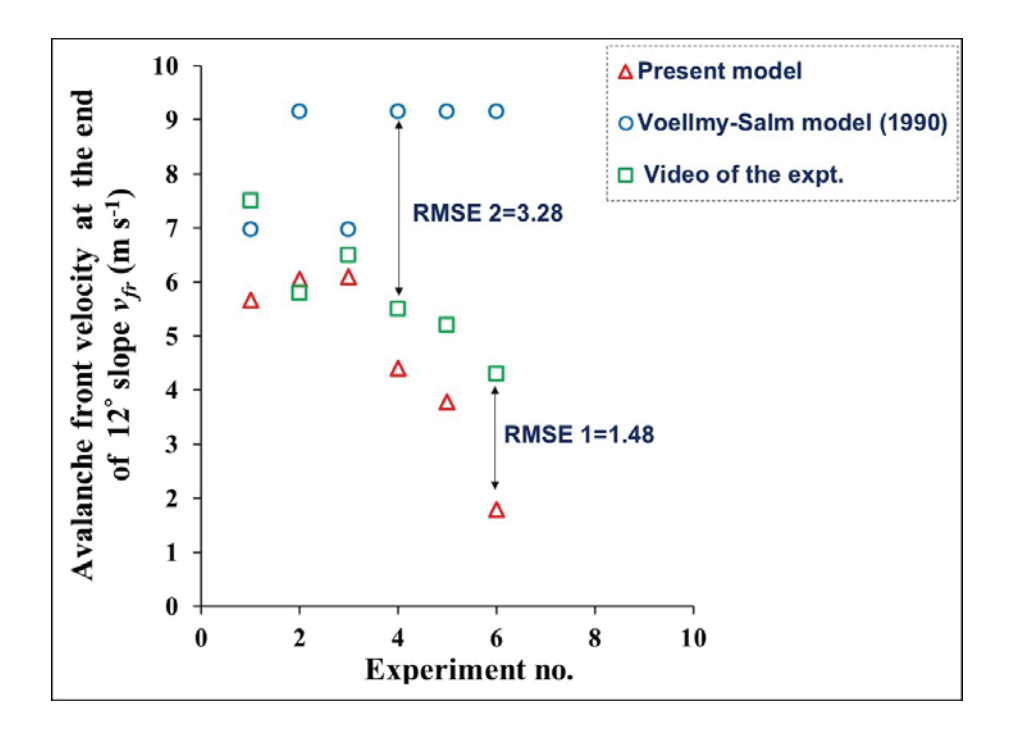


Figure 3.17: Point-wise comparison between the simulated and estimated avalanche front velocities v_{fr} at the end of 12° slope of the snow chute

Figure 3.17 depicts that RMSE 1, the root mean square error between the v_{fr} values; simulated by the model and those noted from the videos of the experiments, is much lesser than RMSE 2, the root mean square error between the v_{fr} values; from the videos of the experiments and those estimated from the Voellmy-Salm method.

Figure 3.18 (a) shows the vertical variation of snow velocity v_s within the flowing snow as the flow is exiting the snow hopper. It can be noted that this profile is almost parabolic in nature. However, as the flow proceeds, the velocity profile becomes almost linear as shown in Figure 3.18 (b) for the 30° and 12° sloped sections. So, avalanche flow can be considered like a plug flow in this case. This result agrees with Kern, Tiefenbacher, and McElwaine (2004) who also observed plug flow over the depth of the flowing snow in their chute experiments, except in the vicinity of the rubber mats. Since, in the current work, surface of chute is of steel, plug flow is observed throughout the snow depth.

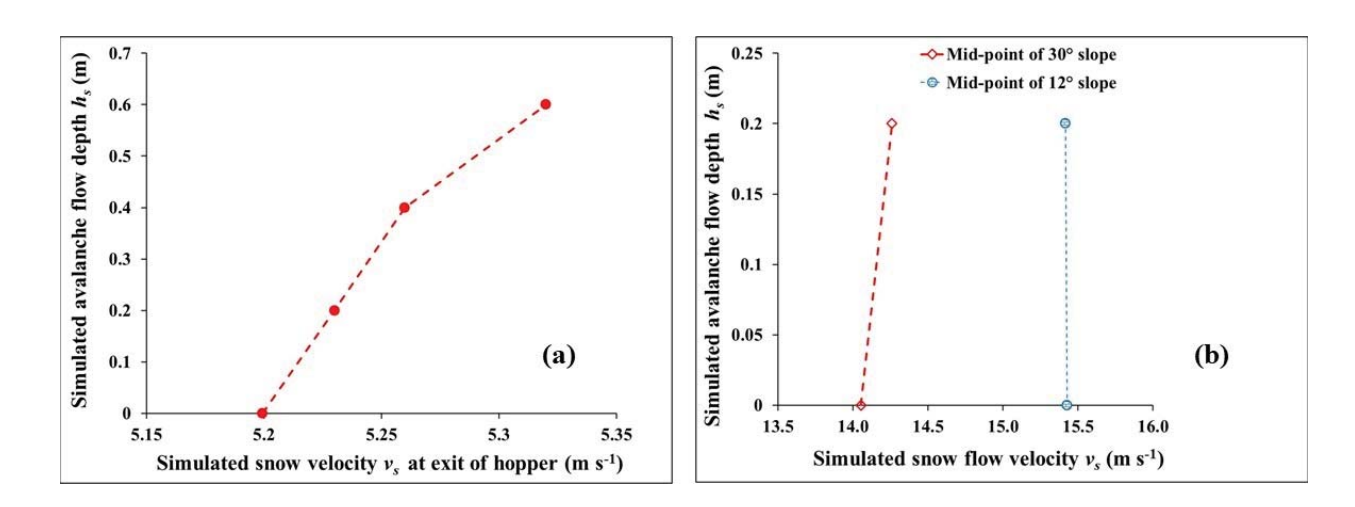


Figure 3.18: Variation of the simulated snow velocity v_s profile (a) at the hopper exit (b) on 30° and 12° slopes

In Figure 3.19 (a), variation of snow dynamic viscosity η_s is shown at various time-steps. It can be seen from this figure that η_s is quite high when snow has just started moving from the hopper; at intermediate time-step t=3.5 s, when snow is moving at high velocity, η_s becomes very low and at t=8.0 s i.e., when complete avalanche mass stops and forms the debris, η_s again becomes very high like a solid. These results are as per the expectations as a snow avalanche has also mixed behavior of fluid and a solid. Similar trend is observed in case of snow strain rate $\dot{\gamma}$ values as shown in Figure 3.19 (b).

In Figure 3.20, transient variation of snow slip-velocity v_s , slip is shown along the length of the chute. It can be seen from the results that v_s , slip is low at the start of the flow, when the flow is developing as well as when flow is coming to a halt. In the middle portion, v_s , slip is high and flow is almost like a plug flow. The simulated values are in satisfactory agreement with the measured v_s , slip values on the Dhundhi snow chute by Upadhyay et al. (2010) on the 30° slope of the chute.

Figure 3.21 depicts contours of air velocity v_a at time-steps t=3.5, 8.0 s. It can be noted from this result that air blast moves over and ahead of the moving snow and keeps on moving even when avalanche mass has stopped fully. This result matches the practical observations for real avalanches which prove that air blast reaches earlier in the runout zone than the moving snow

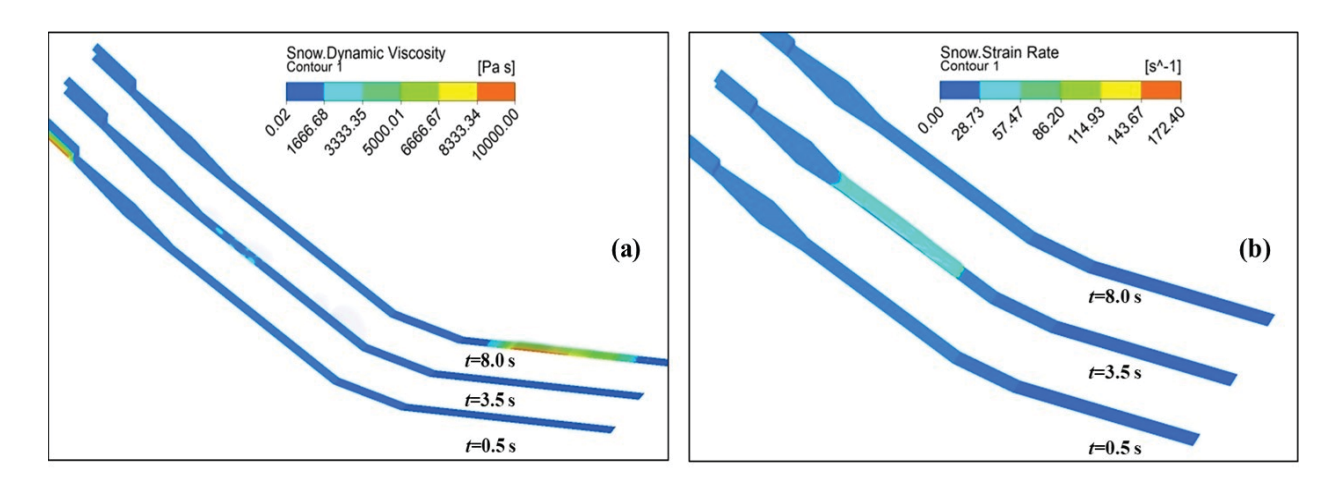


Figure 3.19: Transient variation of the simulated (a) snow dynamic viscosity η_s (a) snow strain rate $\dot{\gamma}$

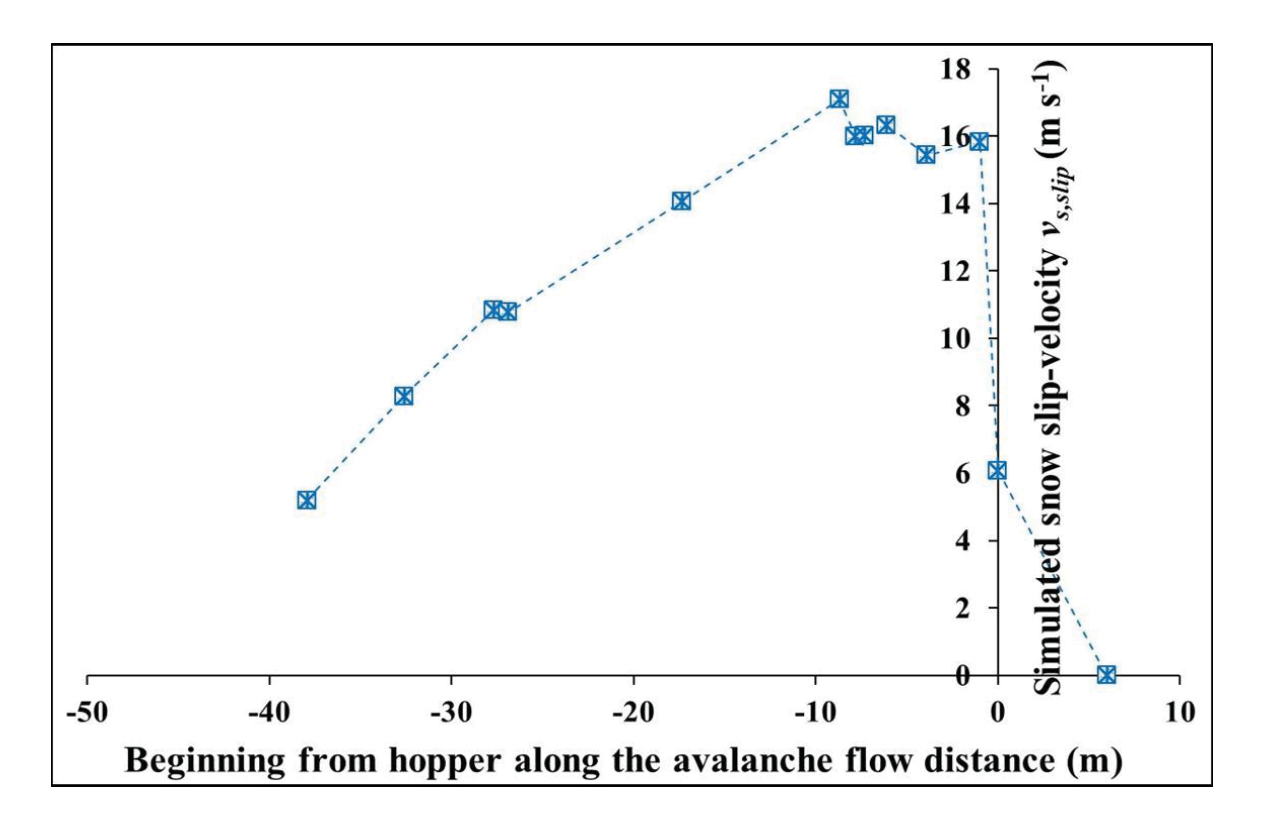


Figure 3.20: Variation of simulated snow slip-velocity $v_{s, slip}$ all along the length of the snow chute

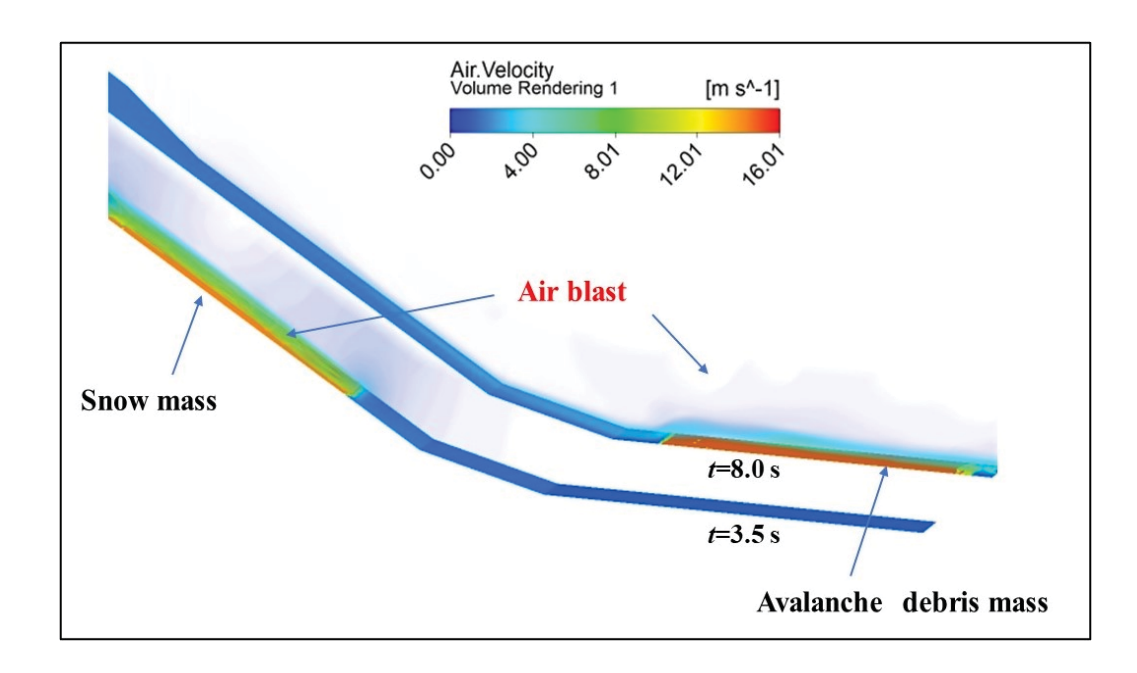


Figure 3.21: Simulated contour of air blast velocity v_a (m s⁻¹) over the snow mass

and also keeps on moving for a longer distance.

3.6 Dynamic similarity of the chute experiments with the real-scale avalanches

The phenomenon of snow avalanches is gravity-driven. Dimensional analysis shows that the law of similitude requires the Froude number $F_r = \frac{v_s}{\sqrt{gh_s}}$ of the flow to be invariant under conversions to the laboratory scale. Figure 3.22 depicts that F_r exhibited by the flow lie in the range 10–15, in the accelerating region of the chute, which are almost overlying with the range of F_r exhibited by the real-scale avalanches, and thereby warrants a dynamic similarity between the experimental runs and the natural snow avalanches (Faug, Naaim, and Fourriere, 2007; Sheikh, Verma, and Kumar, 2008). Lang and Dent (1980) in their research work showed that small-scale modelling of snow avalanches is feasible for the geometric, kinematic, and dynamic similarity based upon the numerical equality of the Froude number F_r between the prototype and

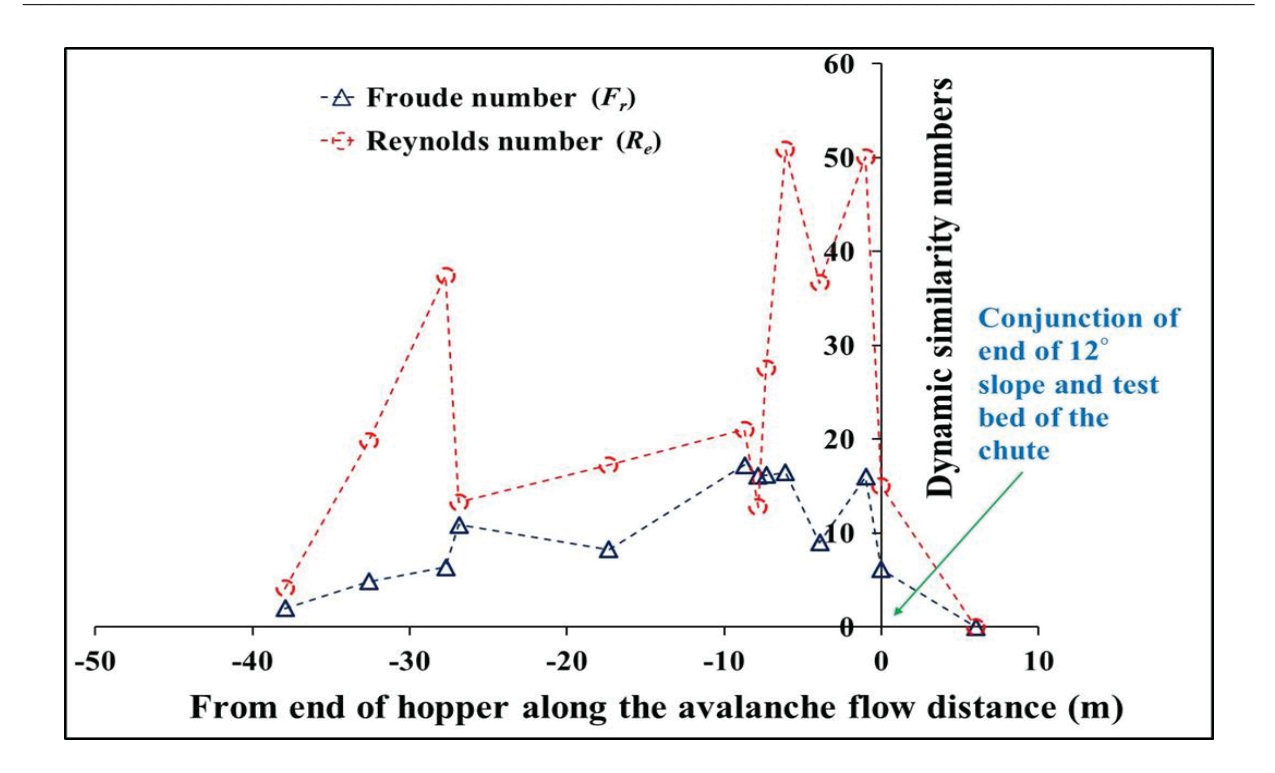


Figure 3.22: Variation of simulated Reynolds number R_e and Froude number F_r of the flowing snow shown as a function of distance, just after the snow is released from the hopper of the snow chute, Dhundhi, H.P., India, for the demonstration of the dynamic behavior of the chute avalanches versus real avalanches

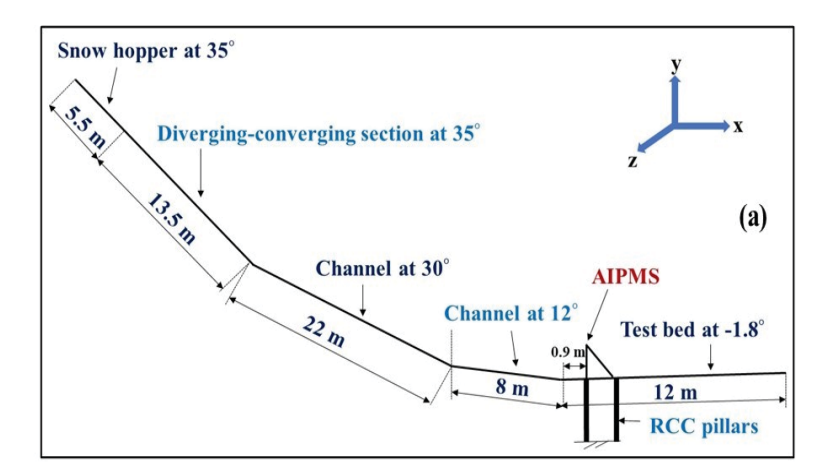
the model avalanches. Authors obtained a Froude number value of 9.6 for the prototype avalanche and 11.2 for the small-scale avalanche. However, this similarity of F_r between the real and small-scale avalanches may not hold for the complete gamut of the avalanches and is no proof that the similarity is due to the same fundamental effects (Sovilla et al., 2008). In the current work, as shown in Figure 3.22, Reynolds number R_e of the avalanche flow ranged from 20 to 39.

3.7 Measured vs. simulated avalanche impact pressures

3.7.1 About the avalanche impact pressure measurement system (AIPMS)

An avalanche impact pressure measurement system (briefly AIPMS in this thesis) has been developed to measure maximum avalanche impact pressure up to 250 kPa, on the snow chute

(elaborated in section 3.3) at Dhundhi, H.P., India. AIPMS essentially encompasses four single axis piezoelectric load cells fitted at an interval of 0.20 m on a stainless-steel plate of size 1 m \times 0.25 m. Two low-carbon steel side plates, each of 0.20 m width were additionally attached to this steel plate on its left and right sides. The schematic of AIPMS is shown in Figure 3.23. The vertical load of the complete impact plate assembly is shifted to four reinforced concrete cement (RCC) pillars through a low-carbon steel base frame, and shear load is taken by a rigid mild steel structure fitted on the back of plate assembly. The RCC concrete pillars, each of size 0.3 m \times 0.3 m \times 2.5 m and matching foundation measuring 1 m deep for the system were designed and constructed by taking in to account both static load as well as bending force due to oblique



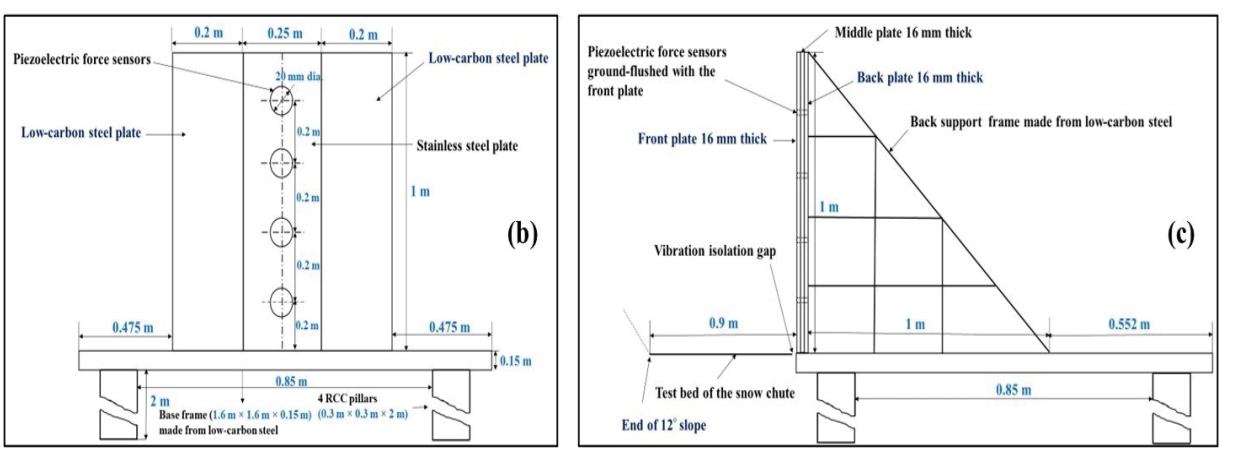


Figure 3.23: Schematic of the avalanche impact pressure measurement system (*AIPMS*) showing (a) its position at a distance of 0.9 m from the end of 12° slope of the snow chute (b) its front plate facing the avalanche (c) its side view showing the back support detail

avalanche forces. In order to isolate the sensor assembly from the noise and vibrations coming from the snow chute body, a uniform gap of 10 mm was provided all around between the base frame and snow chute plates as represented in Figure 3.23 (c). The force sensors were calibrated by PCB Inc., USA, in their laboratory. Before fitting sensors on the plate, the working of the force sensors was confirmed by putting some identified load on them and noting the output of the sensor through data acquisition and display system. Each load cell is overlaid with a circularshaped steel shroud of area 314.28 mm². Neoprene washers were provided around each force sensor to avert ingress of snow/ice through the front plate of the impact assembly. Someresearchers in the past have used impact pressure load cells having bulging surfaces (Jaedicke et al., 2008; Baroudi, Sovilla, and Thibert, 2011; Sovilla et al., 2016). This arrangement of sensors may cause error in the pressure readings when big lumps of snow hit the sensor surface. In the present measurement system, in order that force sensors measure avalanche impact force proportional to its top surface area, the top surfaces of the four force sensors were ground flushed with the instrumented plate. This warrants accurate translation of avalanche impact force values to the equivalent avalanche impact pressures. The output of the four piezoelectric load cells is connected via four co-axial low noise cables having each a length of 20 m, to a signal conditioner which converts the acquired charge from the sensors into the equivalent voltages. Because of the ambient temperature at site going below sub-zero temperatures, some of the temperature sensitive components like DAQ, signal conditioner and DC power supply were kept inside a temperature control enclosure which can maintain the desired air temperature around these components. Signal conditioner is further interfaced to the Data Acquisition System (DAQ). Signal conditioner is given DC power supply through an AC adaptor while DAQ is directly powered by an accurate DC power supply source. Finally, the output of the DAQ is interfaced with a laptop, in which a customized LabVIEW code was installed for data acquisition, display, storage and analysis of the data. Data sampling rate of the system is 1000 Hz. The complete assembly of the AIPMS is exhibited in Figure 3.24.

3.7.2 Experiments conducted using avalanche impact pressure measurement system (AIPMS)

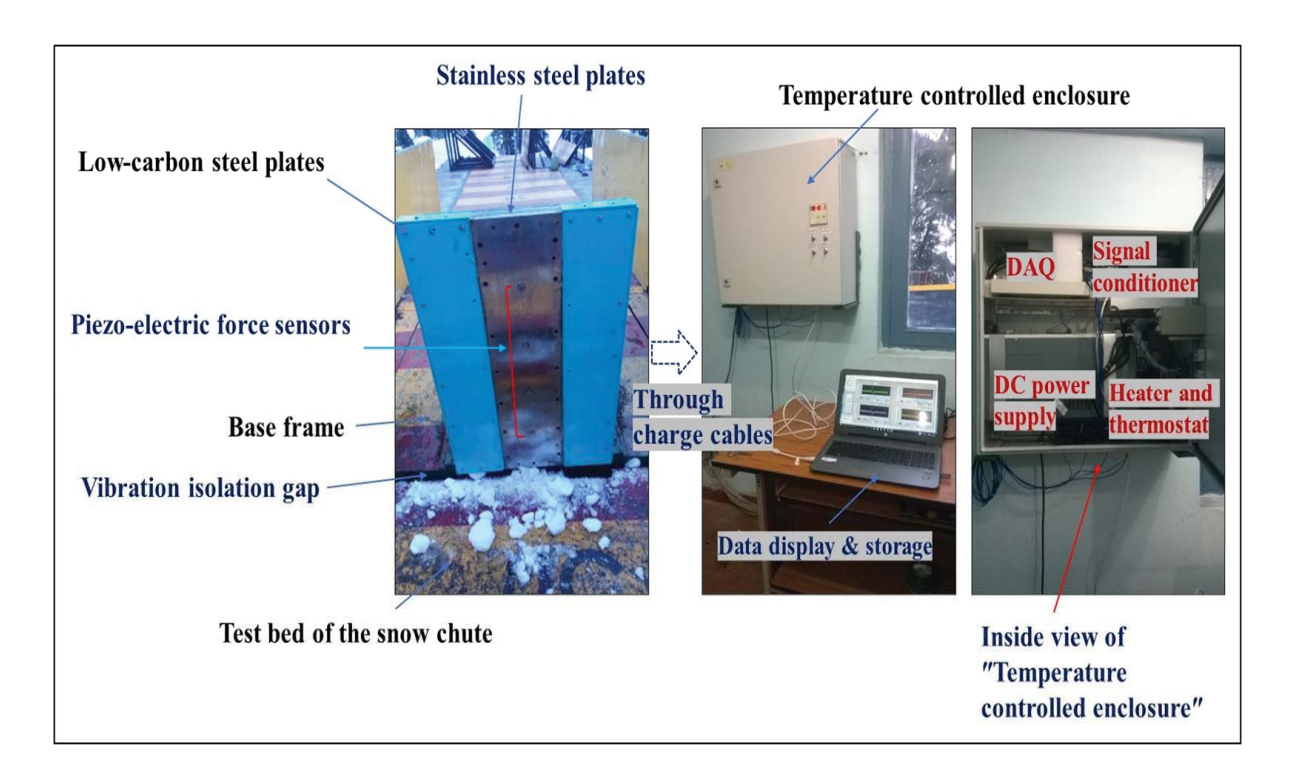


Figure 3.24: A view of the avalanche impact pressure measurement system (*AIPMS*) installed on snow chute, Dhundhi, H.P., India

A total of seven experiments were executed during the period 2020–2021 on the AIPMS to measure avalanche impact pressure P_m values, as summarized in Table 3.3. For the experiments, unobstructed snow was manually filled in the hopper from the nearby area. Although care was taken, still minor compaction of the snow happened during the experiments, due to throwing of the shoveled snow in the hopper. Before opening gate of the hopper, snow temperature T_s (°C) and density ρ_i (kg m⁻³) values were measured at the bottom, middle and top portion of the hopper. These values of T_s and ρ_i were averaged before use in the calculations. Figure 3.25 depicts the interaction of snow chute avalanches with AIPMS during the experiments. In order to comprehend the effect of change in obstacle configuration on the avalanche impact pressures, few experiments were executed after blocking of snow from both the sides of the AIPMS. Detail of one such experiment performed on 15 March, 2021 (E2) is shown in Figure 3.26.

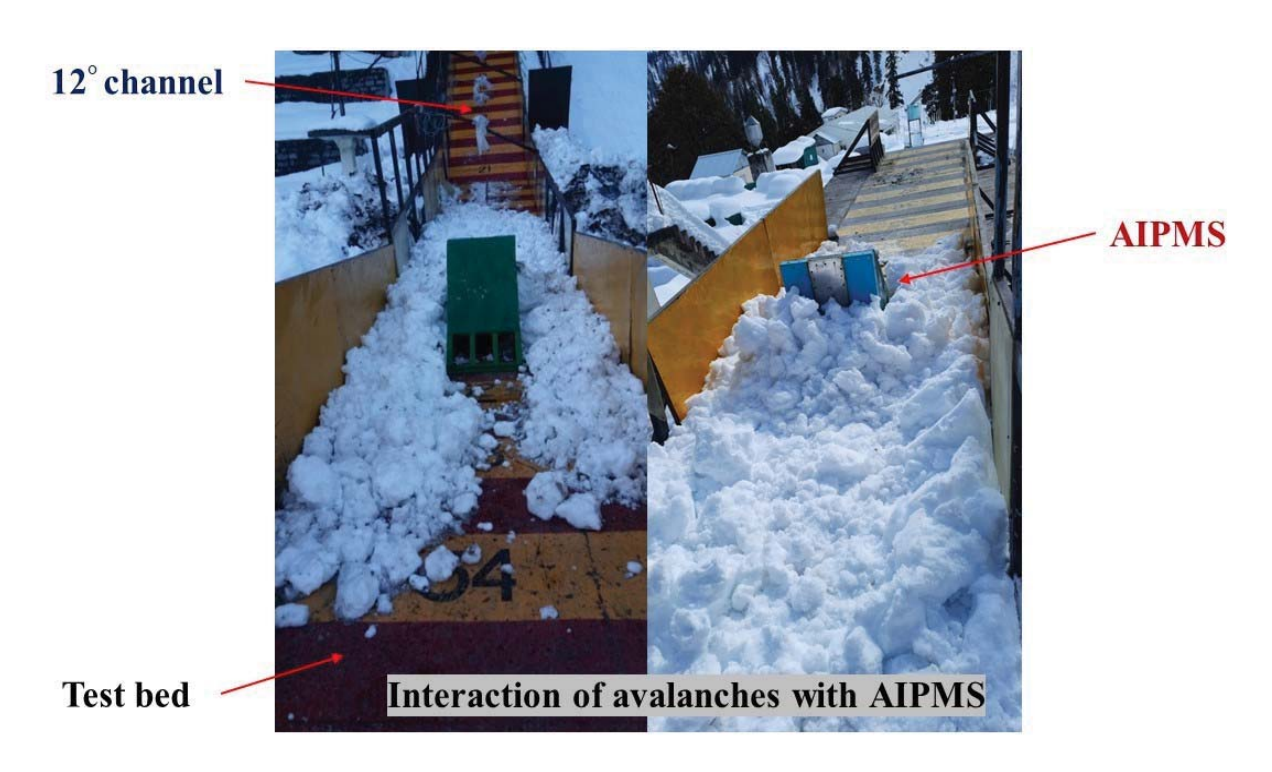


Figure 3.25: A view of the interaction of the snow avalanches with AIPMS at snow chute, Dhundhi (H.P., India)

3.7.3 Comparison between the simulated and the measured avalanche impact pressures

In Figure 3.27, flow of simulated avalanche mass and its interaction with AIPMS at various flow time-steps t is shown. Figure 3.28 (a) depicts contours of snow velocity v_s , at a time-step t=5.2 s. It can be seen from this figure that frontal velocity v_{fr} of the avalanche flow becomes zero at the instrumented structure and its dynamic pressure P_d is converted to the hydrodynamic/gauge pressure p. The contours of the simulated snow total pressure P_s are shown in Figure 3.28 (b). Further, it is stated here that P_s is the sum of P_d and p i.e., $P_s = \frac{1}{2}\rho_i v_s^2 + p$. It is clarified here that simulated snow total pressure is same as the simulated avalanche impact pressure. The observed flow of the avalanche mass at various time-steps t during the experiment executed on

Table 3.3: Summary of the experiments for the measurement of avalanche impact pressure P_m at snow chute, Dhundhi, Himachal Pradesh, India

Date of expt.	Volume of snow in the hopper, V , (m^3)	Avg. density of snow in the hopper, ρ _i (kg m ⁻³)	Avg. density of snow near AIPMS after hitting, ρ _f (kg m ⁻³)	Types of snow grains	ISCG ^a code	Liquid water content in the snow	Avg. temp. of snow, T_s (°C)	Natural /Sieved snow
14 Feb, 2020	11	325	445	Rounded grains	RGlr	M	-1.0	Natural
17 Feb, 2020	11	415	550	Melt forms	MFcl	M	-0.5	Natural
23 Feb, 2020	11	445	545	Melt forms	MFcl	M	-0.5	Natural
15 March, 2021 (E1)	11	578	635	Melt forms	MFcl	М	0.2	Natural
15 March, 2021 (E2)	11	582	640	Melt forms	MFcl	М	0.2	Natural
18 March, 2021	11	565	602	Melt forms	MFcl	M	-0.3	Natural
19 March, 2021	11	542	576	Melt forms	MFcl	M	0.4	Natural

Note: : ^aFierz et al. (2009). The international classification for seasonal snow on the ground



Figure 3.26: Measurement of the avalanche impact pressures P_m by AIPMS after complete blocking of the avalanche flow from the sides with barriers (Experiment E2 on 15 March, 2021)

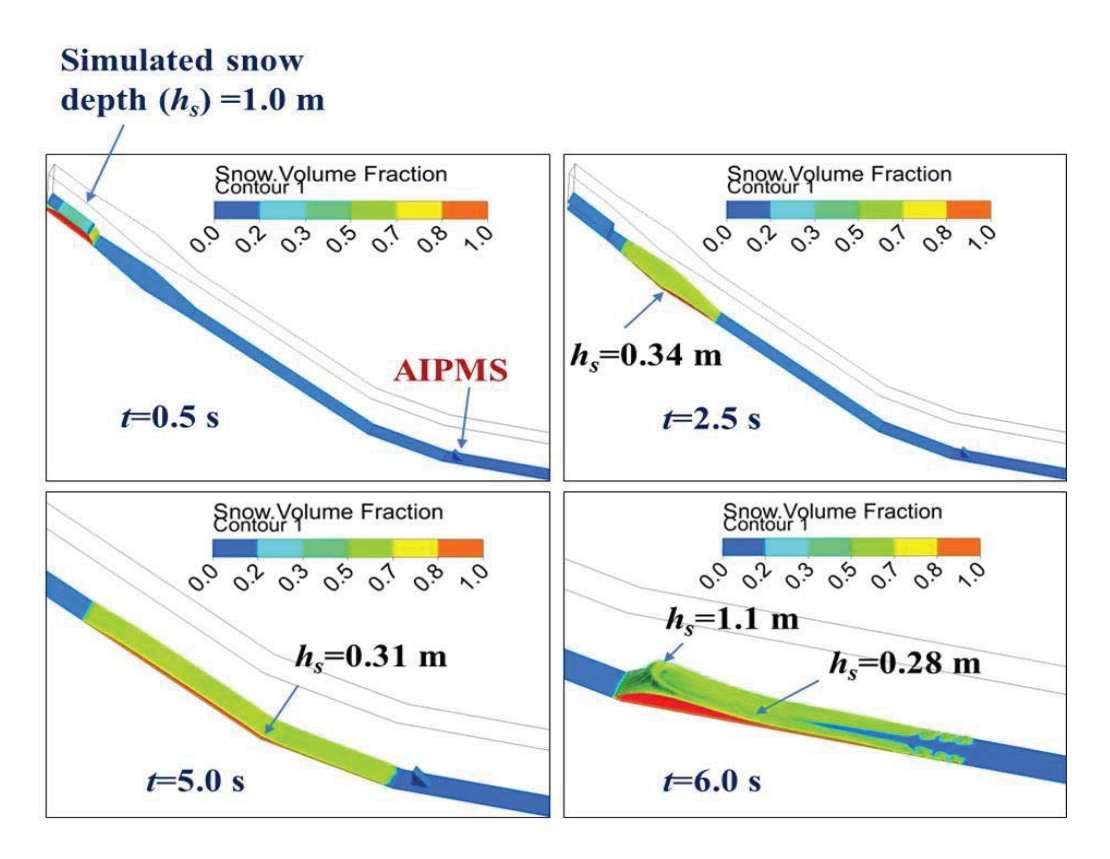


Figure 3.27: Simulation results on experiment on 17 Feb, 2020 for avalanche flow mass and its interaction with AIPMS at various time-steps *t* of the flow

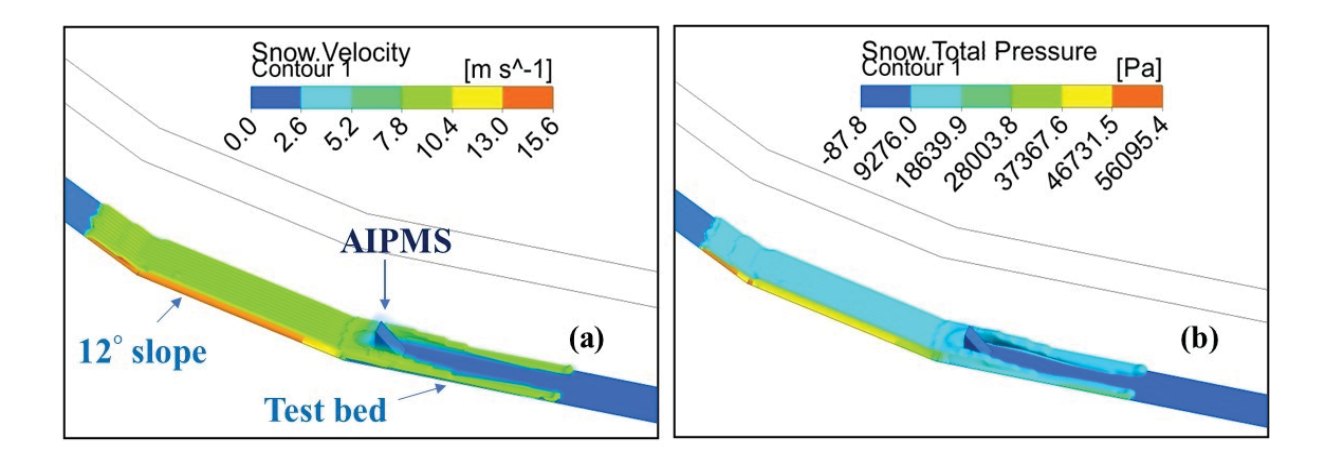


Figure 3.28: At a time-step t = 5.2 s, simulated (a) snow velocity v_s (b) snow total pressure (impact pressure) P_s (Experiment on 17 Feb, 2020)

17 Feb, 2020 is depicted in Figure 3.29. On comparing the simulated avalanche snow depths h_s with experimentally observed snow depths h_e at the explicit points marked in the figures, it is discovered that both the values are of the same order. In Figures 3.30–3.31, comparison between instantaneous measured P_m and simulated avalanche impact pressures P_s at 0.2 m depth and 0.6 m depth of the AIPMS is depicted. In most of the experiments reported in this work, snow did not touch the force sensor located at 0.8 m depth of the AIPMS and so only extreme variation of pressures at 0.2 m depth and 0.6 m depth is reported here. In all these experiments, avalanche can flow from the sides of the AIPMS as shown earlier in Figure 3.25. It can be noted that there are noteworthy deviations between the P_m and P_s values as represented by root mean square error (*RMSE*) on these figures, in the range of 5.26–18.93. In a few cases, there is a time-lag also between the P_m and P_s values. In virtually all the cases reported, there are variations in the P_m values for a short duration while P_s values remain almost constant for a longer duration of time. The main reason for these nonconformities seems to be domination of granular solid behavior of snow in the observed snow chute avalanches in comparison to the dominant fluid behavior in the simulated chute avalanches. Since moist snow is used in the experiments, it is also likely that in

Experimental snow depth $(h_e)=1.0$ m



Figure 3.29: Observation of the avalanche flow and its depth at the significant points on the snow chute at various flow time-steps *t* during the experiment carried out on 17 Feb, 2020

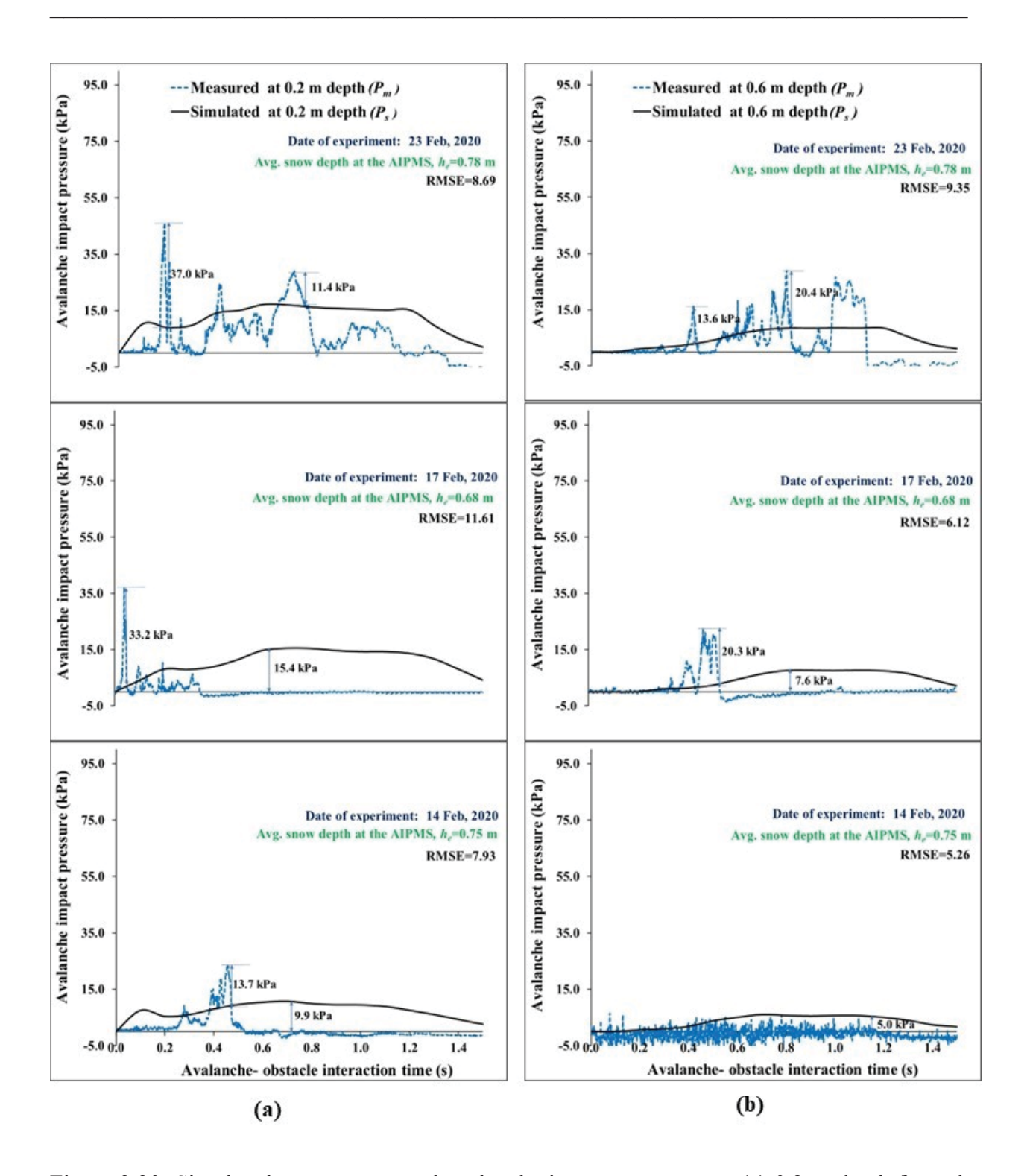


Figure 3.30: Simulated versus measured avalanche impact pressures at (a) 0.2 m depth from the snow chute test bed surface (b) 0.6 m depth from the snow chute test bed surface (Experiments on 14 Feb, 2020; 17 Feb, 2020 and 23 Feb, 2020)

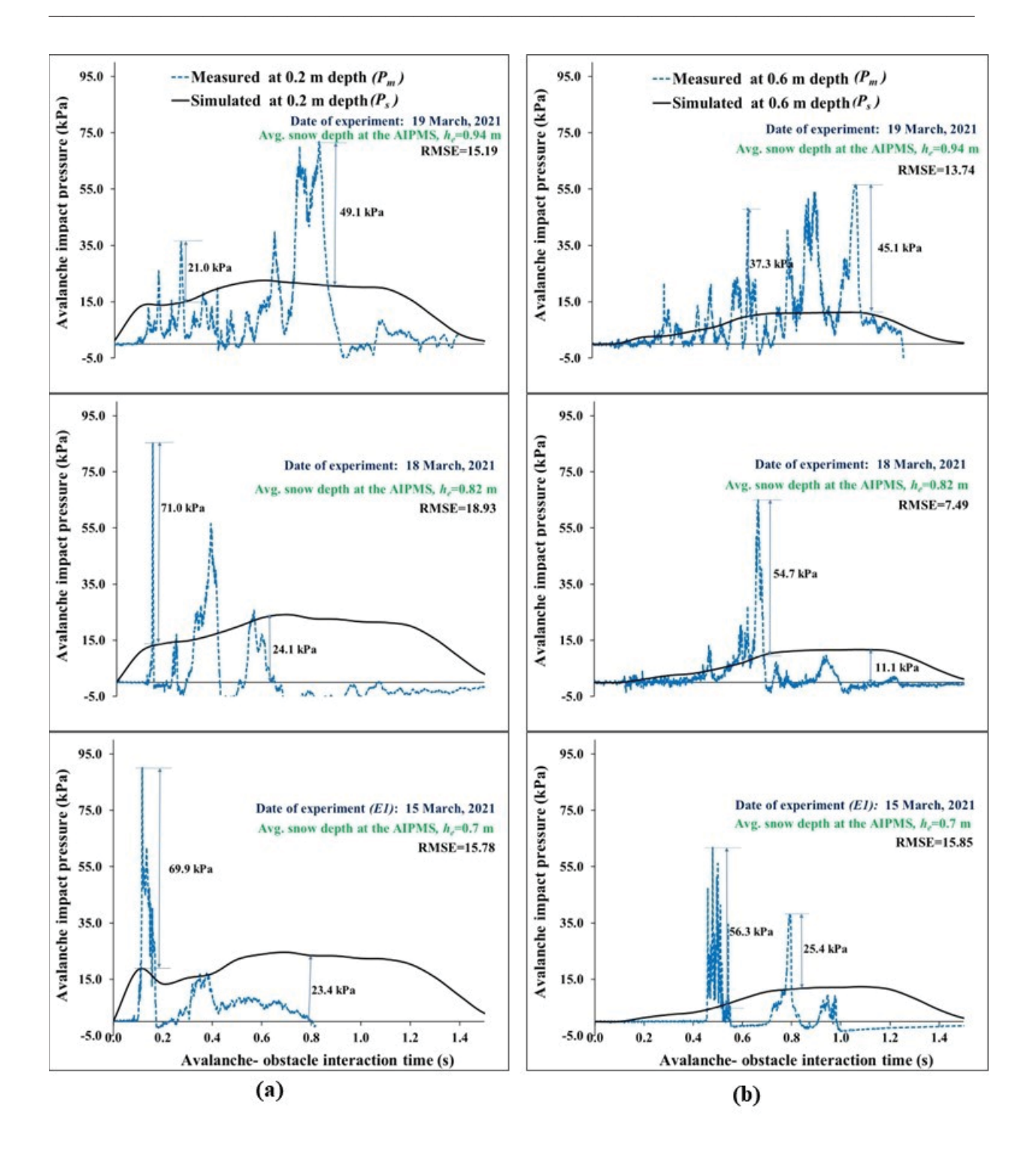


Figure 3.31: Simulated versus measured avalanche impact pressures at (a) 0.2 m depth from the snow chute test bed surface (b) 0.6 m depth from the snow chute test bed surface (Experiments on 15 March, 2021 (E1);18 March, 2021 and 19 March, 2021)

some cases, large masses of non-fluidized snow may have hit the impact sensors resulting in large pressure values. Further, compressibility of snow seems to be another reason for the much larger P_m values than the P_s ones (Eglit, Kulibaba, and Naaim, 2007). Subsequently, a large snow mass deposits in front of the impact pressure sensors exerting higher impact pressures as compared to the simulated ones in which a large avalanche mass passes around the AIPMS structure (Caccamo et al., 2011; Faug, Caccamo, and Chanut, 2012). Another reason for high variations in the measured pressure values is high sampling rate of 1000 Hz at which this data was attained. In order to evaluate the reasons for the deviations between the P_m and P_s values, a comparison was drawn between the peak measured pressure $P_{m, max}$ values and the corresponding peak simulated pressure values $P_{s, max}$ values at 0.2 m depth as shown in the Table 3.4. Since $P_{m, max}$ values are observed at the bottom most part of the AIPMS, only values at 0.2 m depth are selected in this Table. On quantitative analysis, it can be seen that ratio R_p between $P_{m, max}$ and $P_{s, max}$ values steadily increase with the increase in initial density of snow ρ_i which is anticipated because with the increase in ρ_i , solid behavior of the snow increases which remains only partly described in the simulations. The average value of this ratio R_p comes out to be 2.94, which means that $P_{m, max}$ values are roughly three times higher than the $P_{s, max}$ values. It is clear that the

Table 3.4: Ratio R_p of the peak values of the measured avalanche impact pressures $P_{m, max}$ and simulated avalanche impact pressures $P_{s, max}$

Sr. no.	Avg. density of snow before impact, ρ _i (kg m ⁻³)	Peak value of the simulated impact pressure, $P_{s, max}$ (kPa)	Peak value of the measured impact pressure, $P_{m, max}$ (kPa)	Ratio $R_p = \frac{P_{m, max}}{P_{s, max}}$
1.	325	10.77	23.60	2.19
2.	415	15.45	37.20	2.41
3.	445	17.23	46.00	2.67
4.	542	22.59	71.90	3.18
5.	565	24.20	84.90	3.51
6.	578	24.57	90.26	3.67
		Av	verage value of the ratio R_p :	2.94

present simulations consider the incompressible snow density effects in the results and thus are able to capture only approximate dynamic behavior of the avalanches. However, in the measurements, snow microscopic properties like grains cohesion, formation of network of grain chains, snow blocks formation due to moisture and compressibility of snow are playing their role in an intricate manner. Due to these reasons, there is a time-lag also between the $P_{s, max}$ and $P_{m, max}$ values in the results. In spite of all these limitations, it is proposed here to use the ratio R_p for the further approximate analysis of the results.

Figure 3.32 shows the comparison between the P_m and P_s values when avalanche flow is completely blocked from both the sides (as shown earlier in Figure 3.26). In this case, it can be seen that P_m values are similar to the case when the flow was open from the sides. The peak $P_{s, max}$ value is also similar to the case when the flow was open from both the sides of the AIPMS. However, the P_s values remain on a higher side for a much longer time on the obstacle. This is due to the blocking of the snow due to which P_s remains higher for a longer time. It seems that that the main mechanism for higher P_m values in case of high-density moist snow avalanches is the large-sized blocks of snow hitting the obstacle. Thus, in case of high-density avalanches, the confinement and unconfinement of the flow does not seem to play substantial role in affecting the impact pressure values.

3.7.4 Estimation of the effective drag coefficient and corrected peak impact pressures for the moist snow

The fluid drag coefficient C_d for the snow and obstacle was assessed from the following equation (Som and Biswas, 2008):

$$C_d = \frac{F_d}{\frac{1}{2}\rho_i A_p v_{sf}^2} \tag{3.20}$$

Here, F_d (N) is the drag force computed on the frontal projected area A_p of the AIPMS which is computed as the summation of pressure force over the obstacle faces i.e., $F_d = \sum_{i=1}^n p_i A_i$. In the present case, value of A_p is computed as 0.65 m², and v_{sf} (m s⁻¹) is the average free stream snow velocity i.e., velocity far away from the obstacle. It can be seen from Equation (3.20) that the value of v_{sf} should be known in advance for the valuation of C_d for the variable value of the drag

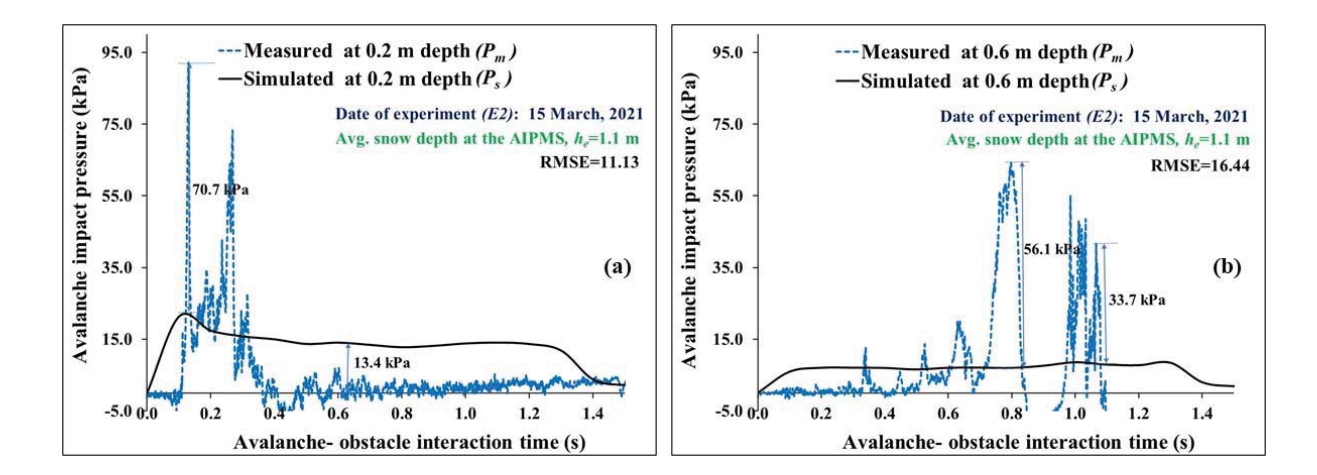
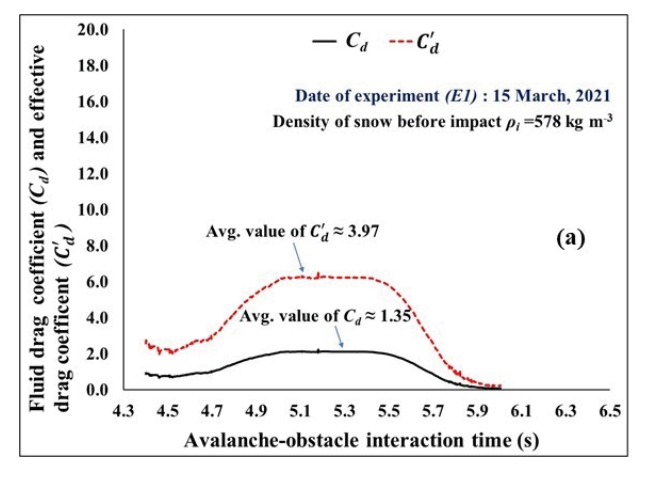


Figure 3.32: Simulated versus measured avalanche impact pressures after complete blocking of flow from the sides with the barriers at (a) 0.2 m depth from the snow chute test bed surface (b) 0.6 m depth from the snow chute test bed surface (Experiment E2 on 15 March, 2021)

force F_d . So, in order to evaluate v_{sf} value, snow velocity v_s was noted at a flow time interval of t=0.1 s during the avalanche-AIPMS interaction process at a 0.8 m distance away from the center of the AIPMS in the z-direction at a depth of 0.4 m from the snow chute surface and the values attained were averaged out. Afterwards, simulation was re-run for the avalanche-AIPMS interaction process by feeding the required value of v_{sf} in Equation (3.20), obtained from the initial simulation and results for drag coefficient C_d attained, as shown in Figure 3.33 (a–b). From this figure, it is obvious that initially values of C_d increase with flow time as the F_d increases on the obstacle, remains constant for some time, and finally decreases towards zero. It can be further noted that the maximum value of C_d is almost double in case of ρ_i = 325 kg m⁻³ as compared to the case of ρ_i = 578 kg m⁻³. Further, the average value of the C_d was estimated as 1.35 in case of ρ_i = 578 kg m⁻³ and 2.90 in case of ρ_i = 325 kg m⁻³. This result indicates that in case of slower moving avalanches, value of C_d is higher than the fast moving avalanches. In the present case, the average value of the C_d considering both the extreme cases is \approx 2.13 But we have seen in the previous paragraphs that there is a strong deviation between the P_s and the P_m values. It means that C_d is not adequate to account for the nonconformities between the two



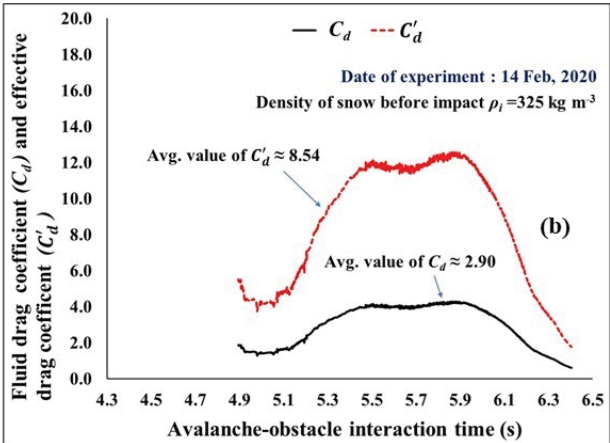


Figure 3.33: Variation of simulated fluid drag coefficient C_d and the corresponding effective drag coefficient C'_d during the avalanche flow-obstacle interaction process in case of the experiments conducted on (a) 15 March, 2021 (E1, $\rho_i = 578 \text{ kg m}^{-3}$) (b) 14 Feb, 2020 ($\rho_i = 325 \text{ kg m}^{-3}$)

values. The point, which needs attention here, is that the concept of C_d is borrowed from the fluid mechanics theories. However, snow in the form of an avalanche has both fluid and solid granular properties, which conjointly affects the values of the avalanche impact pressure on the obstacles. To take into account the solid, granular and compressibility effects of snow, it is proposed here that peak avalanche impact pressure P_i for a dense flow of avalanche on any structure in the avalanche path can be estimated from the following equation,

$$P_i = \frac{1}{2} C_d' \rho_i \, v_{sf}^2 \tag{3.21}$$

 C'_d = effective drag coefficient which can be considered $\sim R_p$ C_d

Otherwise, P_i can be estimated as $P_i = R_p P_{s,max}$. Figure 3.33 (a–b) also depicts the variation of values of C'_d . It can be seen that basically, the trend of variation of C_d and C'_d values remains the same. These results agree with the works of Naaim et al. (2008) and Sovilla et al. (2008) who obtained lower values of C'_d with increasing F_r . Further, the network of chain forces formed inside the dead zone might lead to augmentation of drag coefficients in low-velocity regimes (Faug, Caccamo, and Chanut, 2012). These deductions are also in agreement with the recent

work of Kyburz et al. (2022) where the authors have taken the effective drag coefficient C'_d as the product of obstacle geometry factor and flow regime factor. In the flow regime factor, the authors have considered solid, granular, and fluid properties of the snow. However, it is true that most of the authors in the past have used C'_d values for estimating avalanche impact pressures without modelling the actual structure-avalanche interaction process. In the present case, average C'_d values vary in the range 3.97–8.54. This range of values agrees with the deductions of Salway (1978) who based on their limited field measurements measured drag coefficient values in the range ≈ 4 –12. Our results agree with Sovilla et al. (2016) also, who accounted for the massive impact pressures values by fitting large C_d and ζ values for the dynamic pressure component and the hydrodynamic/gauge pressure component, respectively.

3.7.5 Comparison of simulated impact pressures with the other models

The peak pressures obtained in the current simulations and measurements were compared with the other existing models to comprehend the scatter in the different models. It is stressed here on the use of peak avalanche impact pressure values for the design of safe avalanche control structures in consensus with the observations of Eglit, Kulibaba, and Naaim (2007). The comparison between the output of present proposed model P_i and few prominent models for the estimation of peak avalanche impact pressures is shown in Figure 3.34. It can be noted here that in all the above mentioned models (Voellmy, 1955; Furukawa, 1957; Sovilla et al., 2016), velocity of the block of snow, v_s was estimated from the Voellmy-Salm model (Salm, Burkard, and Gubler, 1990) as 8.52 m s⁻¹. Further, for the impact pressure calculation by Voellmy model, drag coefficient C_d value of 2.13 was used.

From the results, it is obvious that there are substantial deviations between $P_{m, max}$ values and $P_{s, max}$ values estimated by various empirical models. This establishes that the hydraulics-based models can give only rough estimates for the avalanche impact pressure values. However, there is minimum root mean square error $(RMSE) \approx 10.74$, between the output of the present proposed model P_i and $P_{m, max}$ values that reveals better ability of the existing model as compared to the existing models. In order to further improve the direct agreement between the model and measurements, snow microstructural properties like porosity, cohesion, moisture content etc.,

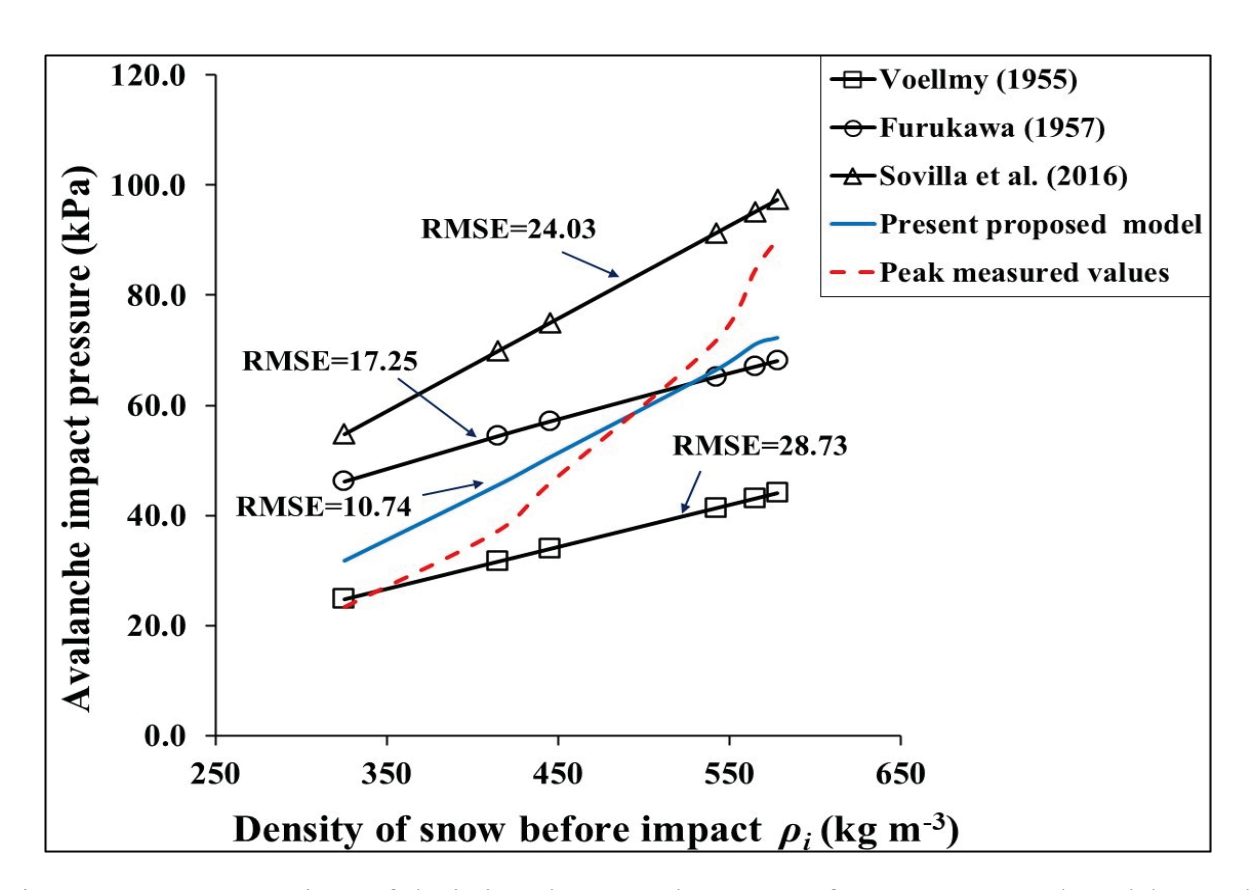


Figure 3.34: A comparison of deviations between the output of present proposed model P_i and other well-known models for the estimation of peak avalanche impact pressures on the obstacles (here, deviations for the above models are calculated with reference to the peak measured avalanche impact pressures $P_{m, max}$ in the current experiments)

along with the compressibility of snow need to be included in the future models.

3.8 Conclusions

A 3-D model based on N-S equations approach for the simulation of avalanches and interaction with the obstacles has been developed. All the significant avalanche flow parameters i.e., velocity, avalanche debris depth, air blast pressure, viscosity, runout distance etc. have been simulated through the model. From the present investigation, it is noticed that the postulation of non-Newtonian fluid model and the wall-slip is crucial in capturing the rheology of the

avalanche. A realistic interaction of avalanche flow with a catch dam kind of geometry was also considered which is not possible with the conventionally used depth-averaged models (Teufelsbauer et al., 2009). The simulated avalanche debris depth values were determined to be in acceptable conformity against the experimental observations with an average RMSE of 0.166. Good agreement was found between the simulated and observed avalanche front velocities with a RMSE of 1.48. Further, the present model was extended to simulate transient variation of avalanche impact pressures on an Instrumented structure. The simulated impact pressures were compared with the measured values attained through a locally developed avalanche impact pressure measurement system. Most of the prevailing studies have used 2-D models for the simulation of the avalanche flow parameters. However, the present 3-D model captured the realistic avalanche flow structure interaction process with least assumptions. The nonconformities between the measured and simulated avalanche impact pressures for the dense flow of avalanches have been deliberated and accounted for. The RMSE between the present proposed model and the measured data is found minimum i.e., nearly 10.74, as compared to the existing prominent models for the assessment of avalanche impact pressure on the obstacles. Further, it is found that fluid drag coefficient C_d alone is not adequate to simulate the avalanche impact pressure on an obstacle in the avalanche path. However, the proposed effective drag coefficient C'_d found to vary in the range 3.97-8.54, that considers the solid, granular, and compressible properties of the snow into account, can better account for the deviations between the simulated and the measured avalanche impact pressures. The present model can be easily extended for the simulation of avalanche impact pressures and related parameters, in the real mountain terrain also. Therefore, the present study can provide useful inputs for improving the design guidelines for the middle zone and runout zone avalanche control structures in the mountainous areas. However, there is a lot of scope for further improvement. In the near future, if snow is modelled as a granular multiphase material with cohesive, compressible properties etc., in place of a continuum incompressible fluid, then the model results can be enhanced to a great extent.

Chapter 4

Estimation of Dynamic Coefficient of Friction of Snow

4.1 Introduction

In this chapter, a new database for the shear force and normal force components of the avalanches and derived values of the dynamic coefficient of friction μ_k between the steel surface of snow chute, Dhundhi, India and the flowing snow avalanche are presented. The measurements were carried out using a three component piezoelectric load cells based dynamometer. Lastly, the measurements were also compared with the published literature. The main motivation behind these experiments was to apply the measured μ_k values for the validation of avalanche dynamics model presented in Chapter 3 of this thesis. With the application of measured μ_k values, uncertainty in the model simulations is likely to be reduced.

4.2 About the measurement system

The measuring system for dynamic coefficient of friction of snow μ k, which consists of a 'Kistler' make 9255B model dynamometer, 20 m long charge cable, eight-cables junction box, four-channel amplifiers and data acquisition and display units is shown in Figure 4.1. The dynamometer includes four number piezoelectric force sensors which are three component type and mounted under heavy preload between two plates of size 260 mm \times 260 mm. Each sensor contains three pairs of quartz plates, one for sensing the force along z-direction, whereas other two sensing force along x and y-directions. The input avalanche force can be split into three orthogonal components. Positive or negative charges are obtained at the connections based on the force direction. Positive charges produce negative voltages at the output of charge amplifier and vice-versa. The dynamometer has a rigidity > 2.0 kN μ m⁻¹ and an adequately high natural frequency of ≈ 2.0 kHz. The measuring accuracy of the system is $\pm 0.5\%$. The fine resolution of

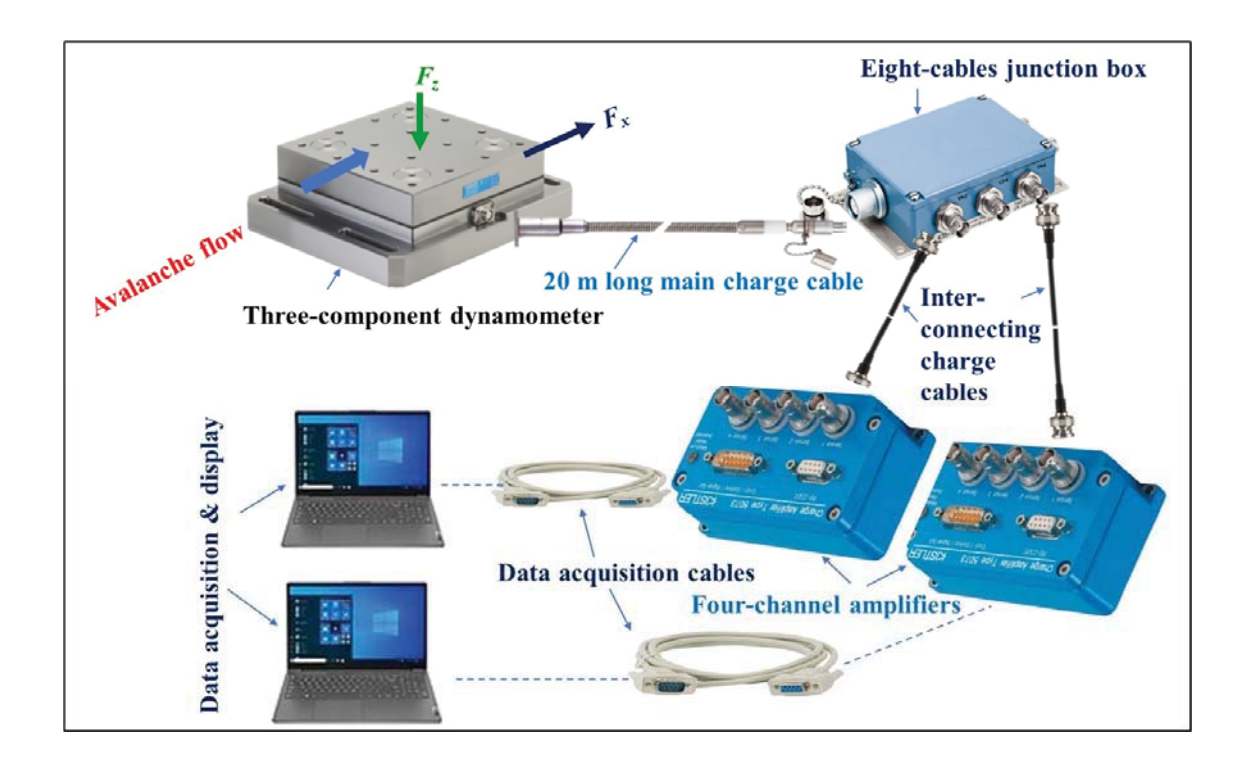


Figure 4.1: Measuring system for shear force (F_x) and normal force (F_z) components of an avalanche

 \pm 0.25% assured the measurement of minimum dynamic changes in the force. The calibration of the dynamometer was done in the factory premises of Kistler Instrumente AG, Switzerland. The dynamometer has a measuring sensitivity of -8.0 pc N⁻¹ for the net shear force of the flowing avalanche F_x (N) in the x-direction and F_y (N) in the y-direction. For net normal force F_z (N) in the z-direction, dynamometer has a sensitivity of 3.7 pc N⁻¹. Further, the output signals of dynamometer are sent to two, four-channel charge amplifiers which convert the dynamometer charge signals into output voltages proportional to the forces sustained. The proportionate voltages produced are attained and displayed on two laptops in real time.

4.3 Installation of the measurement system

The dynamometer mentioned above was installed on a vibration-proof fixture, at a distance of

0.5 m from the end of 30° slope and ground-flushed with the 12° sloped section of the 61 m long and 2 m wide snow chute located at Dhundhi field research station (please refer section 3.3 of Chapter 3 of this thesis). Further, 12° sloped section was chosen for installing the dynamometer as practically, snow sheds are normally constructed at the unification of the end of the avalanche track zone and the roads or low sloped zone of the avalanche path. To isolate transmission of side vibrations to the body of the dynamometer via snow chute sheets, a uniform gap of 10 mm was provided all around the dynamometer. This gap was subsequently filled with soft rubber gasket to thwart the ingress of snow. Figure 4.2 (a) shows a view of the snow chute at Dhundhi indicating the location of the snow friction coefficient μ_k measurement system. Figure 4.2 (b–c) explains the details about the μ_k measurement system.

4.4 Measurement/computation procedure

The acquired peak voltages from the dynamometer were transformed into the corresponding force components by multiplying the voltage values with the respective force conversion factors. Each amplifier gives maximum output of 10 V corresponding to the maximum force. Keeping the expected force range in mind during the snow chute experiments, for acquiring force



Figure 4.2: (a) A view of the snow chute at Dhundhi, Himachal Pradesh, India (b) close view of the dynamometer installed on 12° slope of the snow chute (c) a view of the data acquisition and display details of the snow dynamic coefficient of friction μ_k measurement system

component values in the x-direction, 10 V was set to maximum force of 2 kN i.e., 1 V=200 N. Similarly, for attaining force values in the z-direction, 1 V was set equal to 400 N. After accomplishing the individual force components, the net forces were computed as explained below:

The net shear force of the flowing avalanche F_x (N) in the x-direction i.e., along the avalanche flow direction is calculated as:

$$F_x = F_{x12} + F_{x34} \tag{4.1}$$

Here, F_{x12} and F_{x34} are the measured force components in the x-direction. The net shear force F_y in the lateral direction is not described here as the snow chute flow is confined from the lateral sides.

The net normal avalanche force $F_z(N)$ is computed as the summation of force components in the z-direction i.e., perpendicular to the plane of avalanche flow as given below:

$$F_z = F_{z1} + F_{z2} + F_{z3} + F_{z4} \tag{4.2}$$

Where F_{z1} , F_{z2} , F_{z3} and F_{z4} are the measured force components in the z-direction

Figure 4.3 (a–b) demonstrates the sample graphs acquired on the display screens for the voltage values corresponding to force components in the x, y and z-directions. From these graphs, voltage values were attained and converted into their equivalent force components, from which net force values were calculated. In order to test the accuracy of the dynamometer, a person with known weight stood on its top surface and the equivalent F_z force computed from the attained data. Agreement between both the two readings confirmed that the dynamometer was properly calibrated. Dynamic coefficient of friction μ_k for the chute-steel surface was assessed from the following equation:

$$\mu_k = \frac{F_\chi}{F_Z} \tag{4.3}$$

4.5 Results and discussion

For executing the experiments, snow was filled inside the hopper of the snow chute to its maximum capacity V of 11 m³ by shoveling from the adjoining undisturbed regions. Further, uniformity of the snow samples cut was warranted in the experiments. However, minor

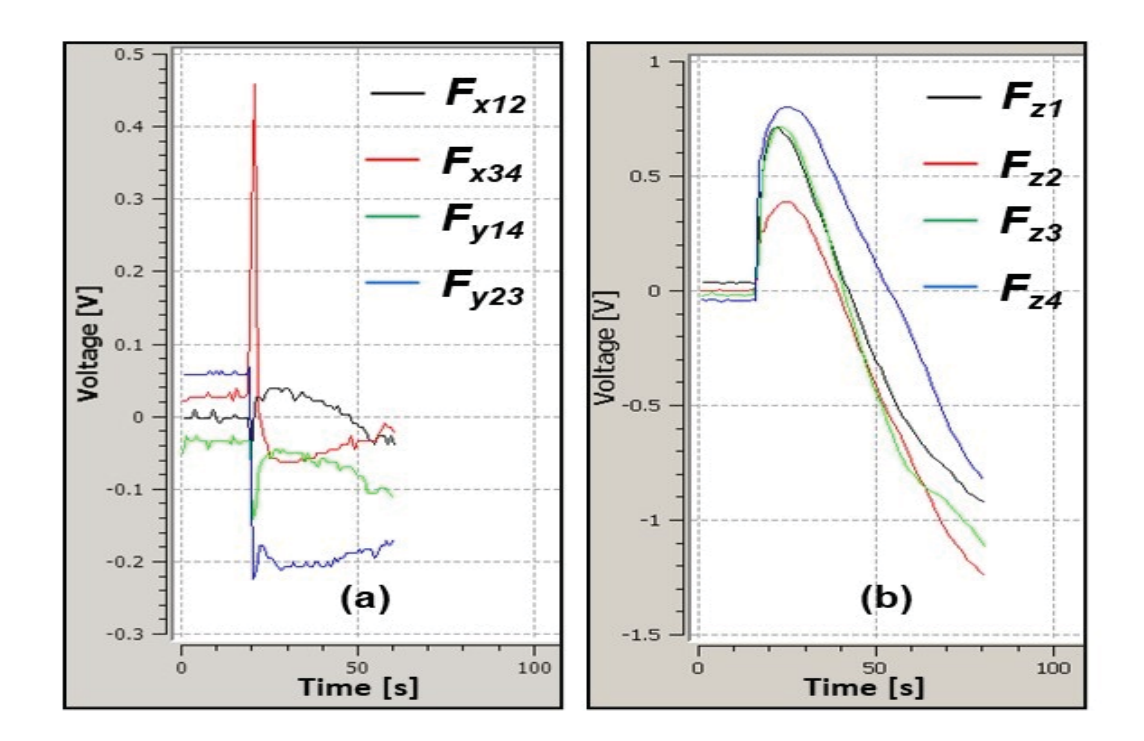


Figure 4.3: Display of voltage values on the computer screens during an experiment at snow chute, Dhundhi, H.P., India corresponding to (a) shear force F_x , F_y components and (b) normal force F_z components

compaction of the snow happened in the hopper during the shoveling of the snow. In case of all the experiments accomplished in the current work, average density ρ_i was considered for the snow occupied inside the hopper. For measuring ρ_i , a 100 cm³ snow cylindrical sampler was gently pushed horizontally within the snowpack, excess snow removed with a snow cutting plate and tapping on it. Weight of the snow measured in grams divided by the sample volume gave the snow density ρ_i . Before using this electronic machine for snow, it was tested for measuring the density of water. Since, water density was measured with \pm 5.0 % uncertainty, it can be assuredly stated that present density measurements for snow are also with \pm 5.0 % uncertainty. For recording force measurements, μ_k measurement system was switched on, reset, and run a few seconds before the release of snow from the hopper during each experiment. The instant avalanche hit the dynamometer, as clarified in the previous paragraphs, F_x , F_y , and F_z force

component graphs (as voltage signals) were captured on the computer screens, saved and after that, peak values of the force components at a specific instant extracted from these graphs. The main source of fault is, not resetting the data acquisition software, before the start of each experiment. Resetting confirms that no residual charge is left on the load cells. If this is not done, sometimes absurd values of the force are recorded, which had to be removed from the present database. The comprehensive summary of the experiments executed during the period 2017-2020 at snow chute, Dhundhi is given in Table 4.1. For the sake of clarity, it is revealed here that the order of present shear force F_x and normal force F_z values is same as that of Platzer, Bartelt, and Jaedicke (2007). However, the range of variation of F_x values in the current experimental work is lesser as compared to these authors's work. On the other side, the range of variation of the current normal force F_z values is more as compared to this reported work. Most probably, the reason for this nonconformity may be that Platzer, Bartelt, and Jaedicke (2007) used rubber mats on the chute surface in their experiments while in the present work, steel surface has been used on the chute. Based on the experimental force data shown in Table 4.1, average value of μ_k is estimated as 0.113. This database can be important for improving and calibrating the avalanche dynamics models explicitly for high-density wet snow conditions. Further, based on these measurements, the variation of shear force F_x and normal force F_z with snow density ρ_i is shown in Figure 4.4 (a–b). Figure 4.4 (a) shows the variation of shear force F_x with the density of snow ρ_i . It can be noted that initially, there is an increase in the values of F_x with the increase in ρ_i but after reaching the value of $\rho_i \approx 500.0$ kg m⁻³, there is decrease in the value of F_x with the further increase in the value of ρ_i . This is possibly due to the fact that with the increase in the ρ_i values, snow grains coalesce together to form a smother surface, and thus shear friction decreases. This indirectly also implies that very high-density (> 500 kg m⁻³) snow avalanches may cover much larger runout distances as compared to the low-density snow avalanches. However, as expected, the normal force F_z values increase with ρ_i values due to increase of the vertical load on the load cells as depicted in Figure 4.4 (b). For the same motives, value of snow dynamic coefficient of friction μ_k decreases with the increase in the values of ρ_i with a coefficient of determination $R^2 \approx$ 0.97 (Figure 4.5). However, based on back-analysis for a large number of avalanche events

Table 4.1: Summary of the measurements for shear force F_x and normal force F_z components of an avalanche during the period 2017–2020 at snow chute, Dhundhi, Himachal Pradesh, India

Date of experiment	Snow density, ρ _i (kg m ⁻³)	Snow type ^a	Temperature of snow T_s (°C)	Net shear force along the avalanche flow direction, F_x (N)	Net normal force perpendicular to the avalanche flow, F_z (N)	Dynamic coefficient of friction between snow-steel interface, (μ_k)
February 10, 2017	280	RG	-1.2	59.09	376.90	0.157
February 11, 2017	290	RG	-1.1	64.75	415.17	0.156
February 27, 2017	393	RG	-0.8	105.02	758.12	0.139
February 27, 2017	313	RG	-0.7	76.59	499.86	0.153
February 28, 2017	297	RG	0.5	68.53	441.44	0.155
February 28, 2017	373	RG	-1.3	84.29	559.46	0.151
February 29, 2017	330	RG	-0.7	99.77	698.85	0.143
March 4, 2018	467	MF	0.0	113.67	946.78	0.120
March 4, 2018	588	MF	0.0	91.30	1151.27	0.079
March 5, 2018	602	MF	0.0	85.78	1166.60	0.074
March 5, 2018	591	MF	-0.7	84.10	1170.66	0.072
March 6, 2018	606	MF	-0.5	69.86	1196.64	0.058
March 6, 2018	636	MF	-0.5	90.17	1154.70	0.078
March 6, 2018	622	MF	-0.3	76.85	1185.50	0.065
March 7, 2018	517	MF	-0.5	109.92	1046.93	0.105
March 7, 2018	458	MF	-0.4	113.53	926.42	0.123
March 9, 2018	457	MF	-0.5	114.60	924.11	0.124
March 11, 2018	571	MF	-0.5	97.18	1130.34	0.086
March 15, 2018	320	RG	-0.8	79.87	524.71	0.152
March 16, 2018	533	MF	-0.5	107.09	1074.32	0.100
March 17, 2018	493	MF	-0.5	112.69	1001.61	0.113
March 18, 2018	600	MF	0.0	77.80	1183.77	0.066
March 19, 2018	620	MF	0.0	86.61	1164.52	0.074
February 14, 2019	417	RG	-0.4	109.68	824.60	0.133
February 15, 2019	383	RG	-0.5	102.55	728.93	0.141
February 15, 2019	457	RG	-0.5	113.50	924.11	0.123
February 16, 2019	390	RG	-0.8	104.31	749.46	0.139
February 17, 2019	407	RG	-0.5	107.96	797.52	0.135
February 18, 2019	508	MF	-0.5	111.17	1030.53	0.108
March 5, 2020	510	MF	-0.4	105.60	1085.60	0.097
March 6, 2020	540	MF	-0.5	112.27	1034.24	0.109
March 7, 2020	596	MF	0.0	88.22	1160.24	0.076
,		Average value of μ_k		0.113		
				Standa	0.032	
					eximum value of μ_k	0.157
					inimum value of μ_k	0.058

Note: ^aFierz et al. (2009). The international classification for seasonal snow on the ground

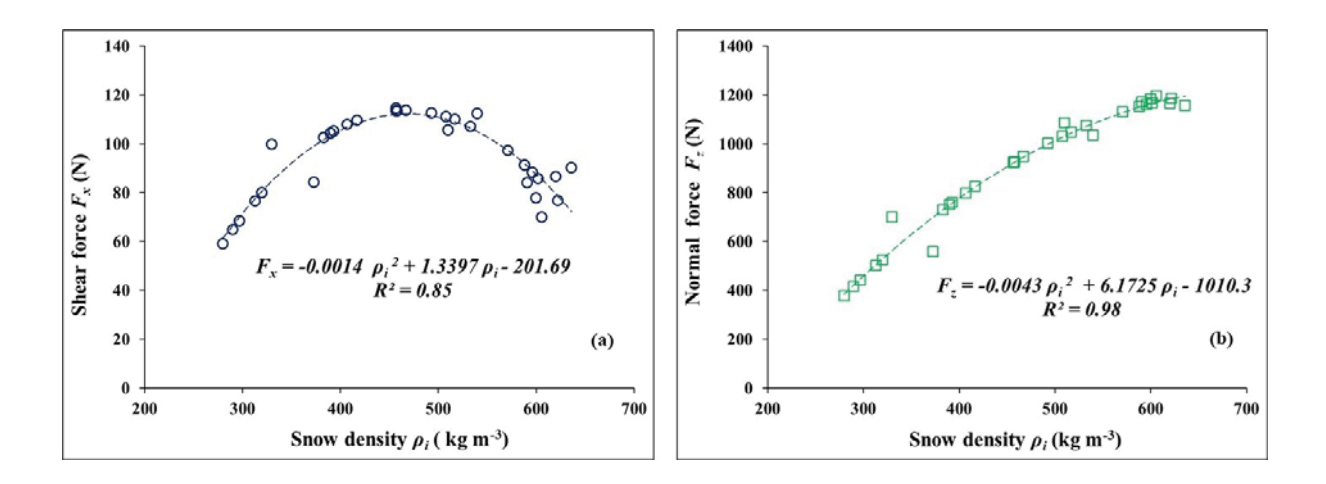


Figure 4.4: Variation of (a) shear force F_x (N) with snow density ρ_i (kg m⁻³) (b) normal force F_z (N) with snow density ρ_i (kg m⁻³)

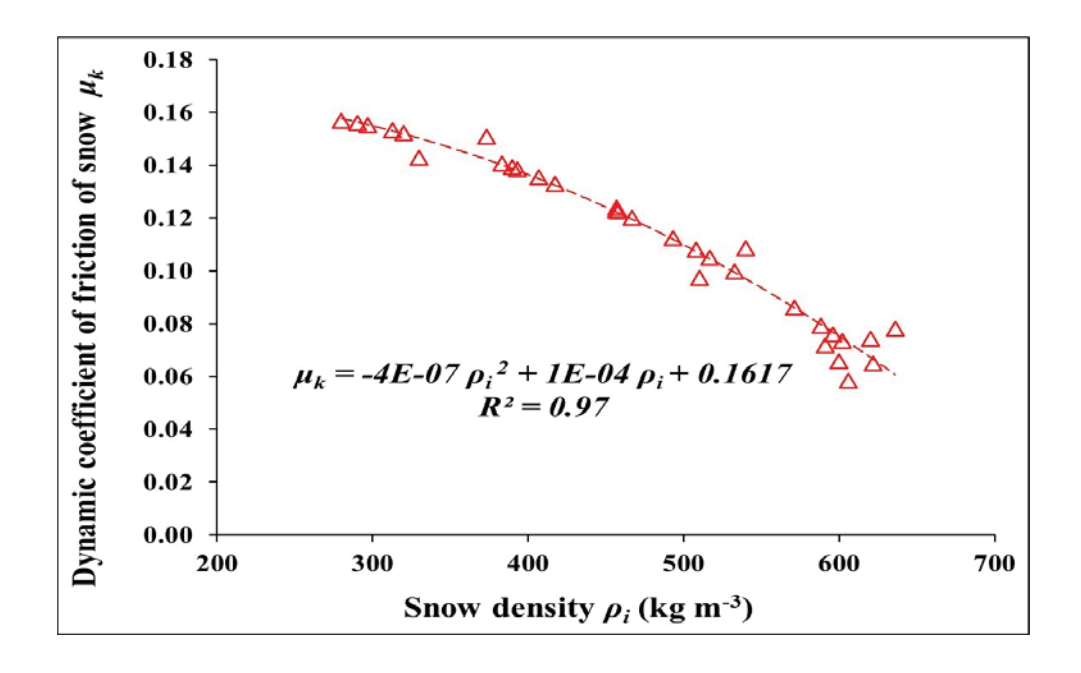


Figure 4.5: Variation of dynamic coefficient of friction of snow μ_k with its density ρ_i (kg m⁻³)

Naaim et al. (2013) found increase in the values of the static snow friction coefficient up to a snow density ρ_i of 200 kg m⁻³. For values of $\rho_i > 200$ kg m⁻³, the authors did not witness any trend. However, present database has got ρ_i values > 200 kg m⁻³. Current results are in good agreement with Mellor (1975) who presented value of μ_k for the steel and snow surface in the range of $\approx 0.12-0.32$ under wide varying conditions of temperature T_s of snow. Authors also noted that with the increase in temperature T_s of snow, there is decrease in the values of μ_k and vice-versa. Differing this result, Platzer, Bartelt, and Jaedicke (2007) found values of μ_k for wet snow avalanches higher than the dry snow avalanches. Naaim et al. (2013) also noticed increase in the values of the snow friction coefficient with the increase in temperature T_s of snow. However, these authors found decrease in the values of the friction coefficient with the increase in liquid water content. From these contradictory observations, it seems that the liquid water content seems to be playing the crucial role in increasing or decreasing the values of μ_k . Colbeck (1988) hypothesized that three friction mechanisms; dry, lubricated and capillary dominate between the snow and the ski slider at different water film thicknesses. The snow dynamic friction is high when the thickness of the water film is inadequate to prevent ploughing by solidto-solid contacts. As the water film thickens and solid-to-solid interactions become less frequent, the slider has to overcome only the viscous resistance of the water film between the supporting snow grains and the slider and so the friction decreases. With further increase in water film thickness, capillary attraction between the snow grains and the slider increases and causes increase in the friction. Possibly due to this reason, friction is high in case of very wet snow. With further analysis, it is found that present measured dynamic friction μ_k values are much lower than obtained by Platzer, Bartelt, and Jaedicke (2007) and Platzer, Bartelt, and Kern (2007). As indicated earlier, the main reason for this appears to be the rubber mats which the authors used at the chute surface in their experiments. Present results are also in accordance with Verma et al. (2004) who assessed value of μ_k in the range ≈ 0.10 to 0.22 for wet snow of density in the range of 250 to 450 kg m⁻³, through the calibration of an avalanche dynamics model with the experimental values of avalanche velocity and runout distance at snow chute, Dhundhi, India. However, the present research could not take into account the effect of avalanche speed on the

value of μ_k in the experiments. Platzer, Bartelt, and Kern (2007) also did not find any dependence of μ_k values on the avalanche speeds but Schaerer (1975) found that μ_k varies inversely with the speed of the avalanche. Differing this observation, McClung and Schaerer (1983) found that μ_k increases with the speed of the avalanche. Ancey and Meunier (2004) found the dependency of μ_k on the avalanche speed in an intricate manner. So, due to large variability in the observations, this aspect also requires further investigation.

4.6 Conclusions

In the current work, a limited set of experiments has been executed for the measurement of shear force and normal force components of high-density wet snow avalanches on a small-scale. Based on these measured values, average value of the dynamic coefficient of friction of snow μ_k has been estimated as 0.113 with a standard deviation of 0.032. Due to dynamic similarity between the snow chute flow and the real avalanches, the measured force values and the estimated friction values can be applied for validating, calibrating the avalanche dynamics models and enhance the design accuracy of the avalanche control structures like snow sheds etc. for the different mountain terrains. Practically, the present friction database has been effectively used in validating one avalanche dynamics model. However, the present work has got certain restrictions. There is a need to make the present friction measurement system more manageable by providing real-time storage of the experimental data on the computers. Further, in the present work, dynamic friction coefficient for high-density wet snow has been obtained between the steel-snow interface. So, this data base may have restricted applications in validating the avalanche dynamics models in the avalanche velocity range of ≈ 14 to 17 m s⁻¹. Additional experiments can be done in the near future for obtaining extensive database for the snow dynamic friction coefficient by fixing surfaces of diverse materials on the bed of the snow chute. Further, in the present research, quantification of liquid water content was not done. So, in the future experiments, there is a need to measure the liquid content within snow for getting better perception in the complex variation of μ_k . Further, the effect of variable avalanche speeds on the values of dynamic coefficient of friction of snow needs to be extensively studied in the near

future. In spite of all these restrictions, the present work has got vital significance as executing experiments on the real avalanche sites for the measurements of these parameters is rather hazardous and challenging.

Chapter 5

Simulation of Avalanche Flow Interaction with an Instrumented Tower at a Real Avalanche Site

5.1 Introduction

In this Chapter, an attempt has been made to simulate avalanche flow interaction with an Instrumented Tower installed in the path of a prominent avalanche site named MSP-10 at Dhundhi which is approximately 20 km away from Manali, Himachal Pradesh, India. For the simulations, the 3-D avalanche dynamics model developed in the current thesis (*Chapter 3*) is applied for the simulation of significant avalanche flow parameters, in the 2-D domain of the avalanche site mentioned here.

5.2 Brief description of the study site

Dhundhi is located at a latitude of 3030 m in the Pir Panjal range of Indian Himalaya. At this location, a prominent avalanche site named as MSP-10 exists. Average slope θ of the formation zone of MSP-10 site is 34.2°; approximate length of 700 m. Formation zone has an approximate snow fracture area of 15000 m². Middle zone has an average slope of 20.8° and approximate length of 850 m. Runout zone has an average slope < 12° and approximate length of 600 m. For the estimation of snow fracture depth h_d (m) of the early winter avalanche, last thirty years, three days maximum increment in standing snow $\Delta h_{ss, max}$ (cm) observed at Dhundhi field observatory during the period of December to March was used (Figure 5.1). Afterwards, $\Delta h_{ss, max}$ value was multiplied with the specific avalanche site correction factors for the slope, altitude and wind drift, to get the corrected value of h_d which is given by the following equation (Buhler et al., 2018):

$$h_d = 0.01 * (\Delta h_{ss, max} \cos (28 * \Pi/180) + (A_d - 2800) * 0.05 + 30) * 0.291/ (\sin (\theta * \Pi/180) - 0.202 * \cos (\theta * \Pi/180))$$
 (5.1)

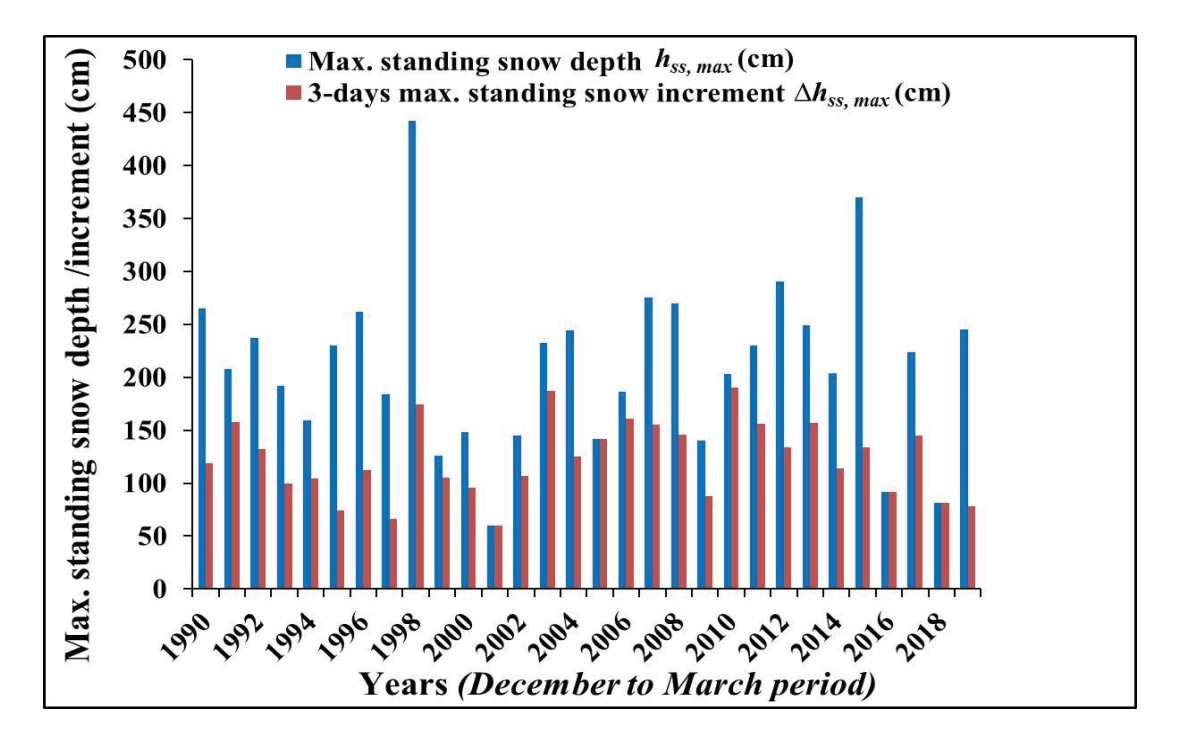


Figure 5.1: Observation of maximum standing snow depth $h_{ss, max}$ and three days maximum increment $\Delta h_{ss, max}$, for the months December–March (1990–2019) at Dhundhi field observatory, H.P., India

Here, A_d is the average altitude of the formation zone of MSP-10 avalanche site which is estimated as 3411 m. With these considerations, estimated value of h_d for early winter avalanches is 1.7 m. For the later spring avalanches from April onwards for the estimation of snow fracture depth h_d , maximum standing snow in the month of April was considered as shown in Figure 5.2 which was later on multiplied with the avalanche site correction factors as described in Equation (5.1). With these considerations, estimated value of h_d for late winter avalanches is 2.2 m.

5.3 Application of the model developed in current work

For the simulations work, the avalanche dynamics model developed in Chapter 3 of this thesis was applied in the 2-D domain of the MSP-10 avalanche site elaborated in section 5.2 above. In this work, to capture the correct rheology of the avalanche, snow was considered a bi-viscous

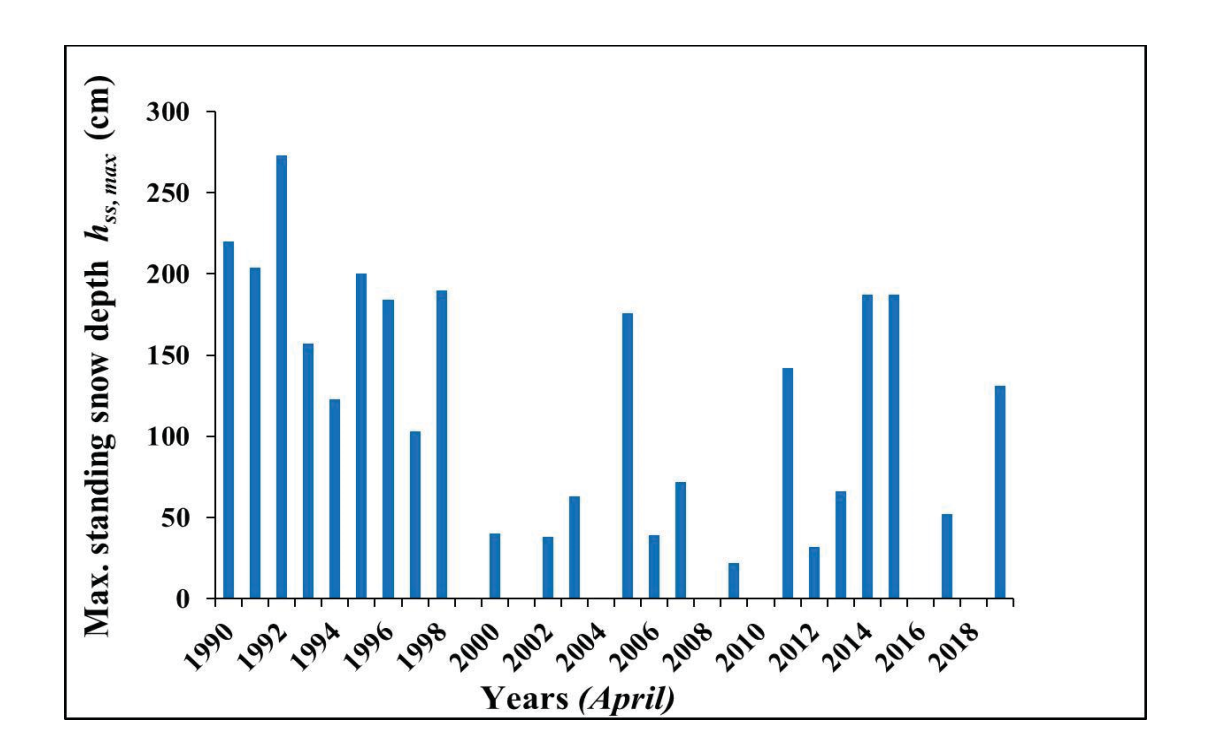


Figure 5.2: Observation of maximum standing snow depth $h_{ss, max}$, in the month of April (1990–2019) at Dhundhi field observatory, H.P., India

Bingham fluid (Lang et al., 1985). Due to the granular nature of snow, the usual no-slip wall boundary condition at the ground surface of MSP-10 avalanche site was replaced with a wall shear stress model. Later on, user defined functions for the bi-viscous Bingham fluid model for snow and wall shear stress models were hooked to the main program code as elaborated in sections 3.4.4.1 and 3.4.4.2 of this thesis.

5.4 Domain, meshing and boundary conditions

In order to draw the computation domain for MSP-10 avalanche site, an elevation profile was drawn in the preferential avalanche flow direction through the Google Earth software (Figure 5.3). Based on this elevation profile data, domain for MSP-10 site along with the Instrumented

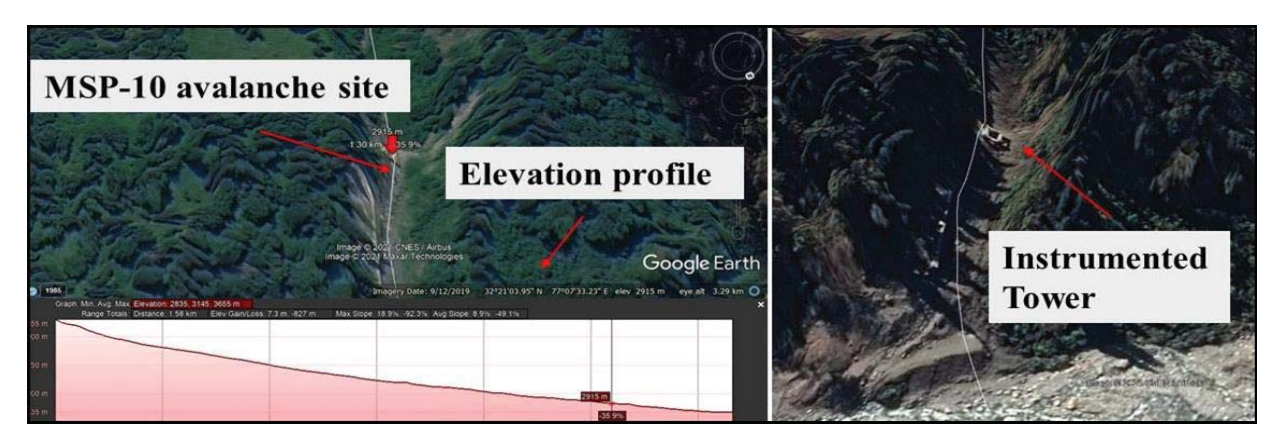


Figure 5.3: Drawing of elevation profile along the preferential avalanche flow direction for MSP-10 avalanche site at Dhundhi, H.P., India

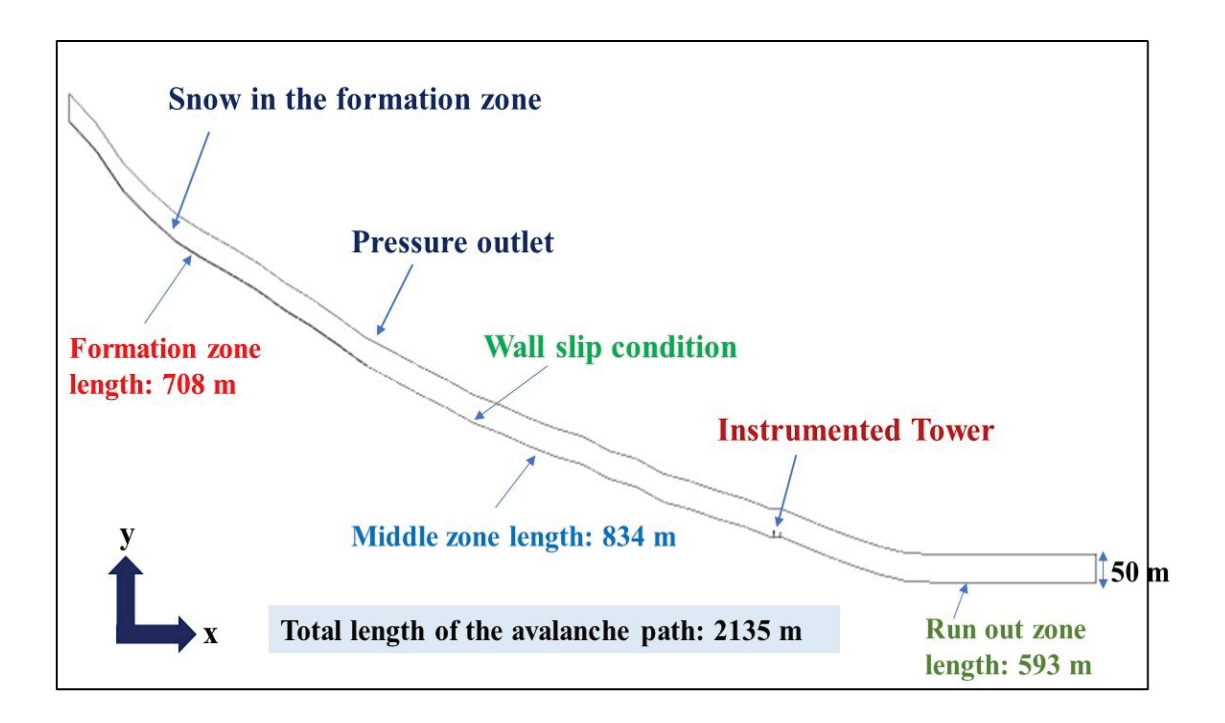


Figure 5.4: Geometric domain for MSP-10 avalanche site with Instrumented Tower at Dhundhi, H.P., India

Tower was drawn in the CAD package of the ANSYS Fluent software as shown in Figure 5.4. Actual close view of the Instrumented Tower at MSP-10 site is shown in Figure 5.5 (a).

Chapter 5: Simulation of Avalanche Flow Interaction with an Instrumented Tower at a Real Avalanche Site

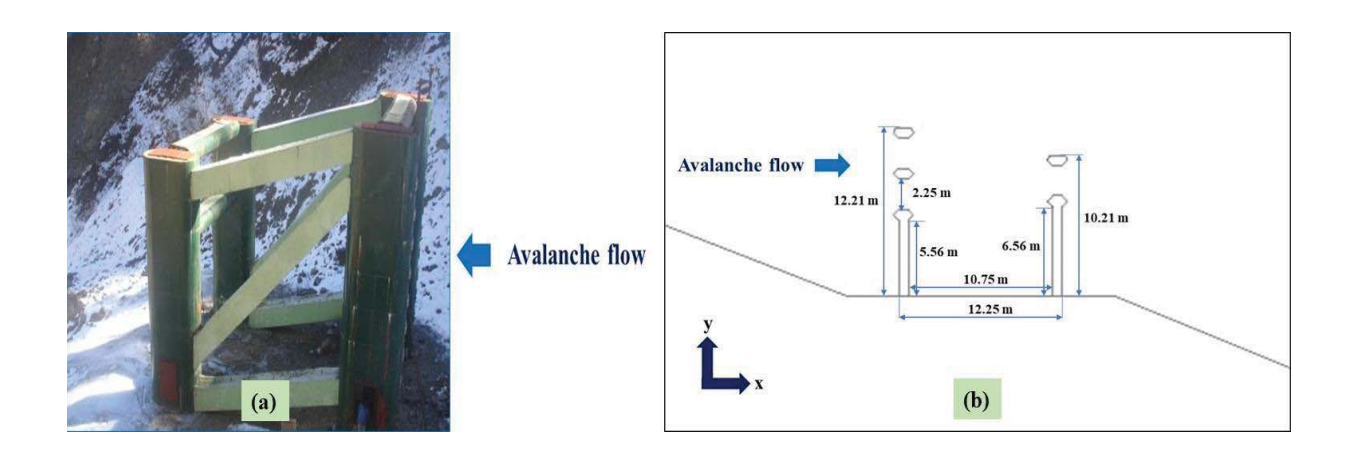


Figure 5.5: Instrumented Tower at MSP-10, Dhundhi, H.P., India (a) a close view of the real structure at the site (b) 2-D simplified geometry used for the CFD model simulations

However, for the modelling and simulation purpose, the geometry of the Instrumented Tower was drawn in a 2-D simplified manner as shown in Figure 5.5 (b). The complete domain was meshed with uniform 0.5 m quad mesh. The mesh had minimum orthogonal quality of 0.52, maximum aspect ratio of 5.14 and total number of cells as 427473. A computation time-step ε of 0.001 s was used in all the simulations and default convergence criteria was used for the residuals for solving the mass and momentum equations.

5.5 Results and discussion

For carrying out simulations, three extreme cases (C1, C2 & C3) of the initial snow conditions in the formation zone of the avalanche have been considered in the present work. In the first case C1, density of snow $\rho_i = 200 \text{ kg m}^{-3}$ and fracture depth of snow $h_d = 1.7 \text{ m}$ were considered. h_d was computed through Equation (5.1) as described earlier also. This low-density snow is considered based on the triggering of fresh snow avalanches for which the most suitable period is from December to March. In the second case C2, snow is assumed ρ_i as 200 kg m⁻³ and fracture depth h_d as 6.0 m. Thus, value of h_d is taken considering snow mixing from the sides of the formation zone of the avalanche and adding to the depth of the snow. In the third case C3, snow

is assumed of density ρ_l of 400 kg m⁻³ and fracture depth of snow h_d as 2.22 m as computed through Equation (5.1). This high-density snow is considered, based on the triggering of late winter spring snow avalanches for which the most suitable period is the April month. Wall-slip factor W_s has been considered as 0.25 in all the simulation cases mentioned above. Here, W_s indirectly represents the Coulomb friction between the snow and the ground surface. In the first case Cl, simulation of avalanche flow interaction with the Instrumented Tower at various timesteps t is shown in Figure 5.6. It can be observed that at t=45 s, large avalanche debris mass deposits before the tower and some of the snow mass jumps over the tower and keeps on moving in the runout zone of the avalanche. The simulated results of most significant avalanche flow parameters i.e. snow volume fraction ($avalanche\ mass$), snow velocity v_s (m s⁻¹) and snow total pressure P_s (Pa) ($avalanche\ impact\ pressure$) in all the three cases at time-steps t=35 s and t=45 s are shown respectively in Figure 5.7 and Figure 5.8. It can be observed form these results that at

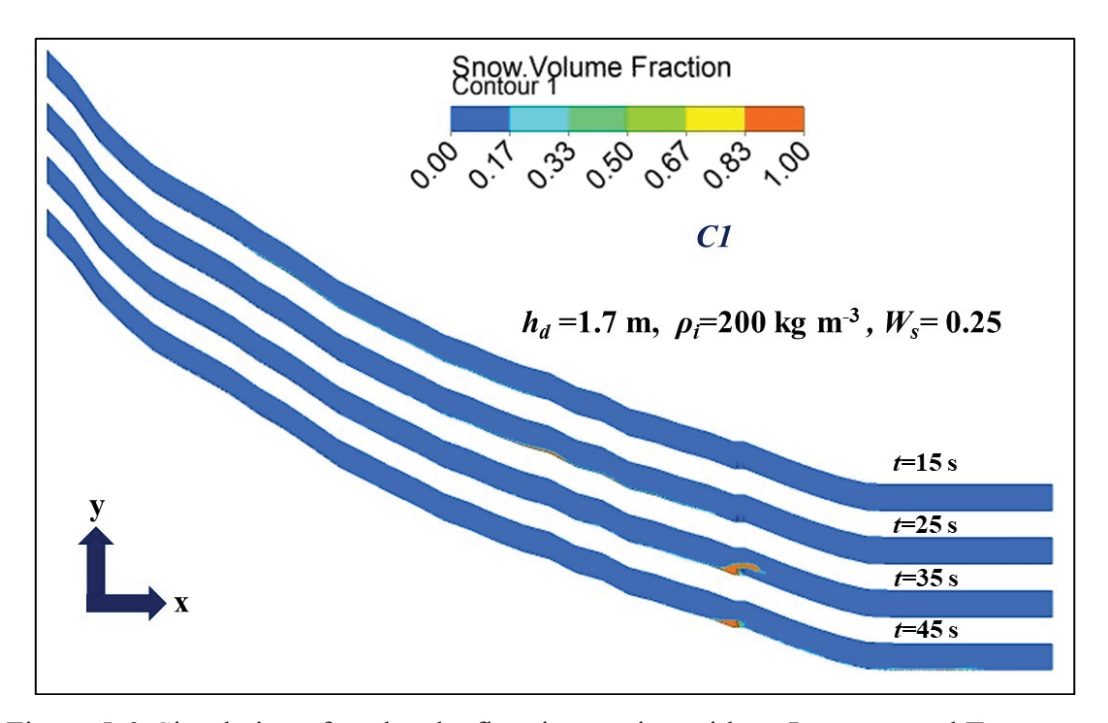


Figure 5.6: Simulation of avalanche flow interaction with an Instrumented Tower at MSP-10 avalanche site, Dhundhi, Himachal Pradesh, India at various time-steps t of the flow for snow density $\rho_i = 200 \text{ kg m}^{-3}$ and snow fracture depth $h_d = 1.7 \text{ m}$ (Case CI)

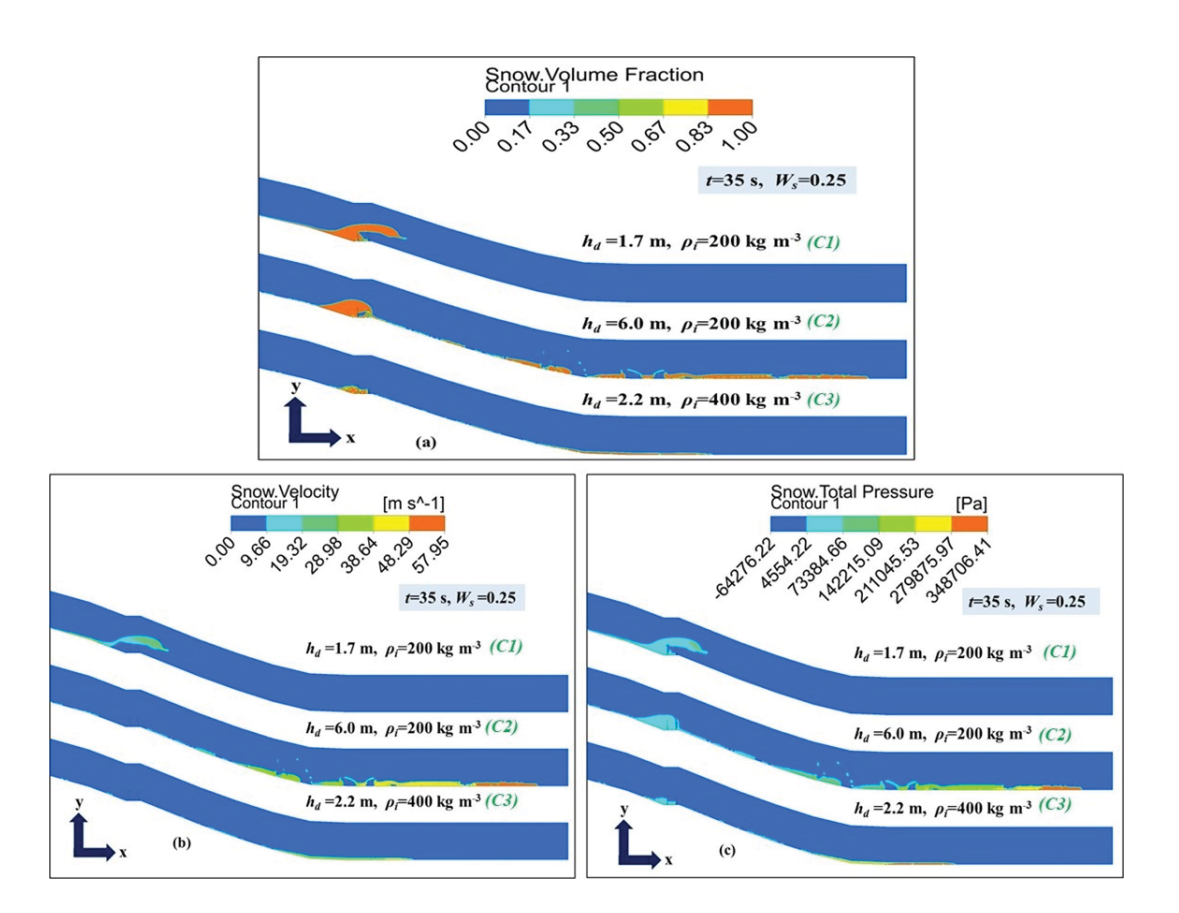


Figure 5.7: Simulation of (a) snow volume fraction (b) snow velocity v_s (m s⁻¹) (c) snow total pressure P_s (Pa), in the three cases (C1, C2 & C3) having different snow density ρ_i (kg m⁻³) and fracture depth h_d (m) in the formation zone of the avalanche, at a time-step t=35 s and wall slip factor W_s =0.25

t=35 s, some of the snow avalanche mass is jumping over the Instrumented Tower in case C1 while at the same time-step, in cases C2 and C3, avalanche mass is moving ahead in the runout zone. This is probably due to higher snow depth in case of C2 and higher snow density ρ_i in case of C3. It is interesting to note that magnitude of snow total pressure P_s (avalanche impact pressure) is almost similar in all the three cases, which is approximately 50 kPa. It can be seen from Figure 5.8 that a large snow mass fully stops before the Instrumented Tower at a time-step t of 45 s. The value of this debris is highest in case C2 and lowest in case C3. Due to higher snow

Chapter 5: Simulation of Avalanche Flow Interaction with an Instrumented Tower at a Real Avalanche Site

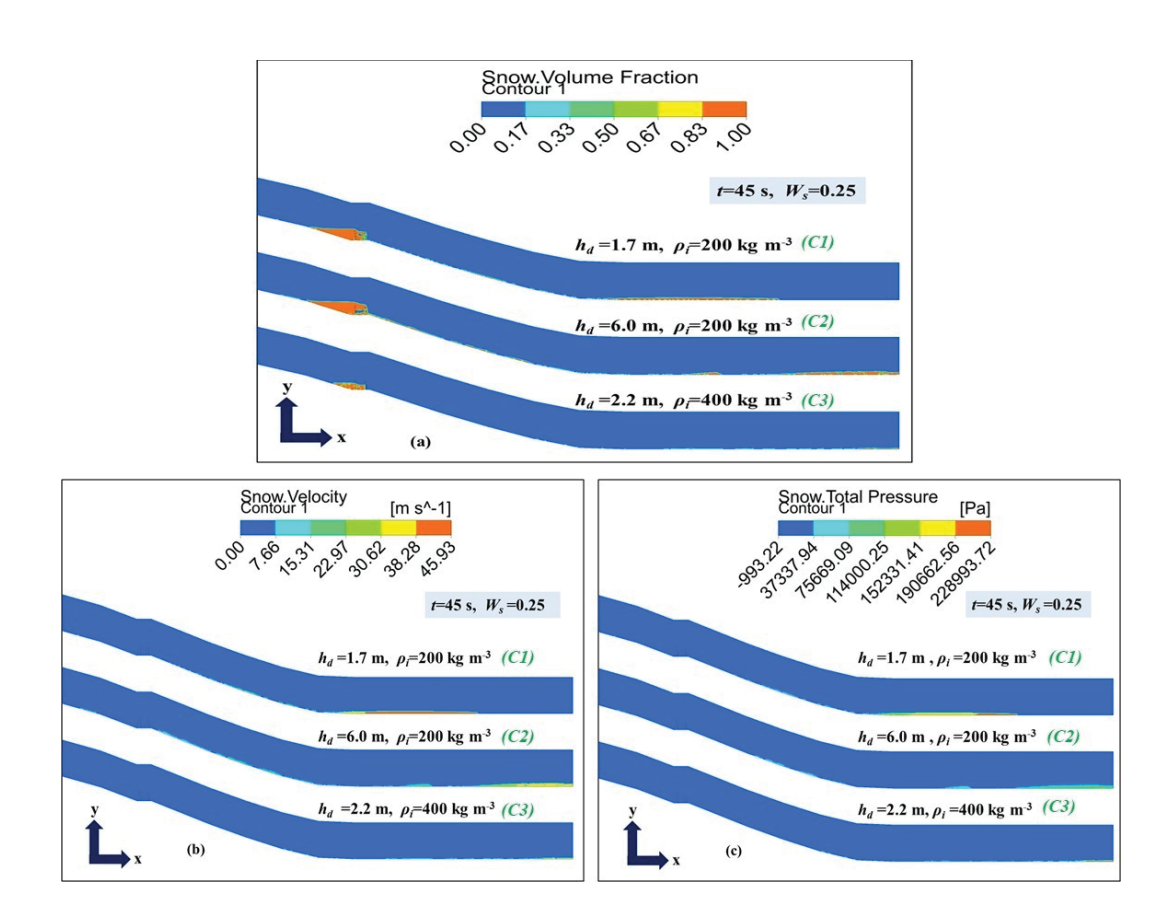


Figure 5.8: Simulation of (a) snow volume fraction (b) snow velocity v_s (m s⁻¹) (c) snow total pressure P_s (Pa), in the three cases (C1, C2 & C3) having different snow density ρ_i (kg m⁻³) and fracture depth h_d (m) in the formation zone of the avalanche, at a time-step t=45 s and wall slip factor W_s =0.25

density in case C3, snow moves with a higher velocity and so snow deposition before the Tower is lesser in this case. At this time-step, there is no dynamic loading on the Instrumented Tower as can be seen from the snow total pressure contours shown in Figure 5.8 (c). For the sake of clarity, the zoomed views of the snow velocity contours and snow total pressure at the same time-step t are shown in Figure 5.9 and Figure 5.10, respectively. These simulated results are in agreement with the ground observations of avalanche debris deposition around the Instrumented

Chapter 5: Simulation of Avalanche Flow Interaction with an Instrumented Tower at a Real Avalanche Site

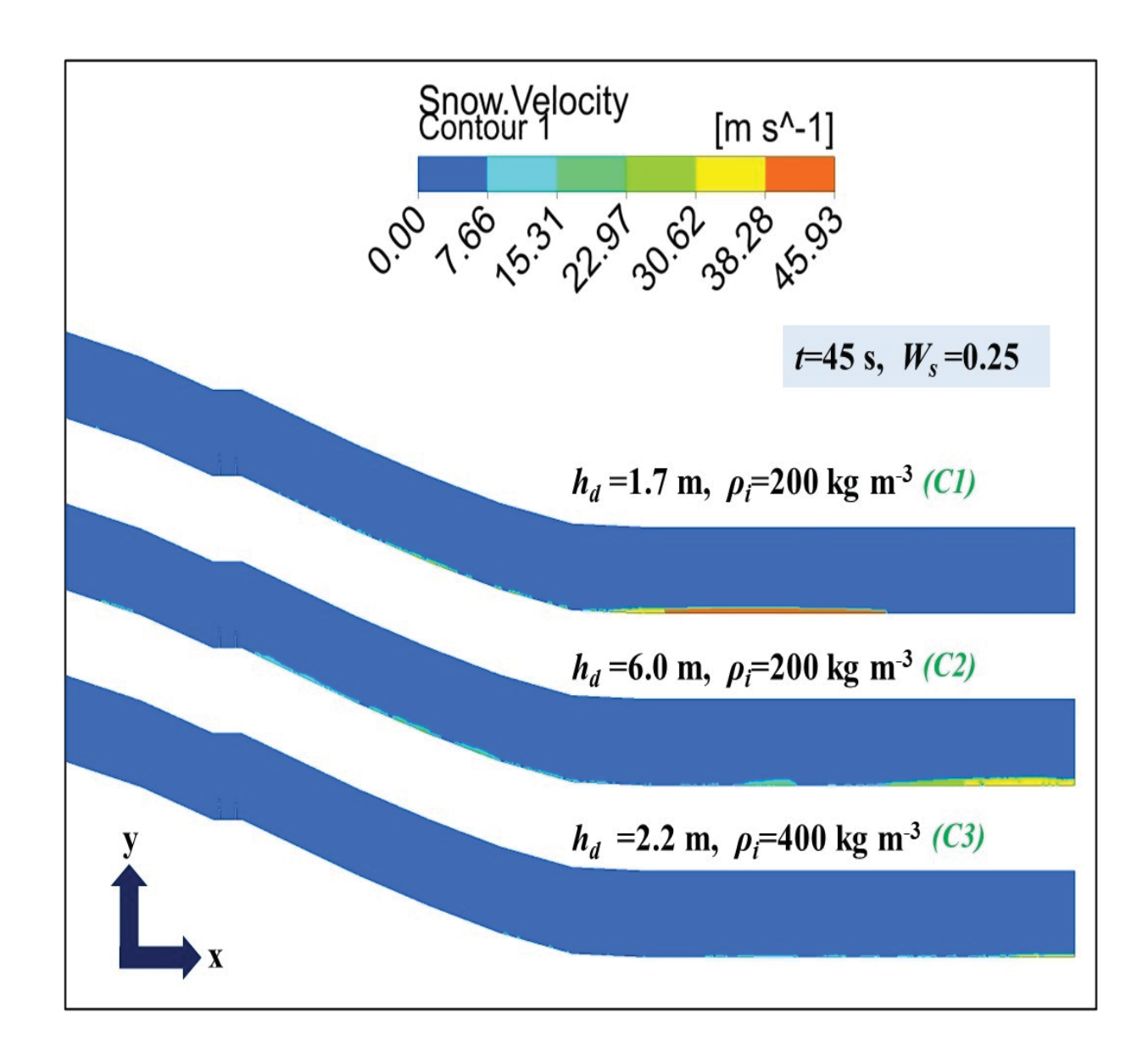


Figure 5.9: A zoomed view of simulation of snow velocity v_s (m s⁻¹), in the three cases (*C1*, *C2* & *C3*) having different snow density ρ_i (kg m⁻³) and fracture depth h_d (m) in the formation zone of the avalanche, at a time-step t=45 s and wall slip factor W_s =0.25

Chapter 5: Simulation of Avalanche Flow Interaction with an Instrumented Tower at a Real Avalanche Site

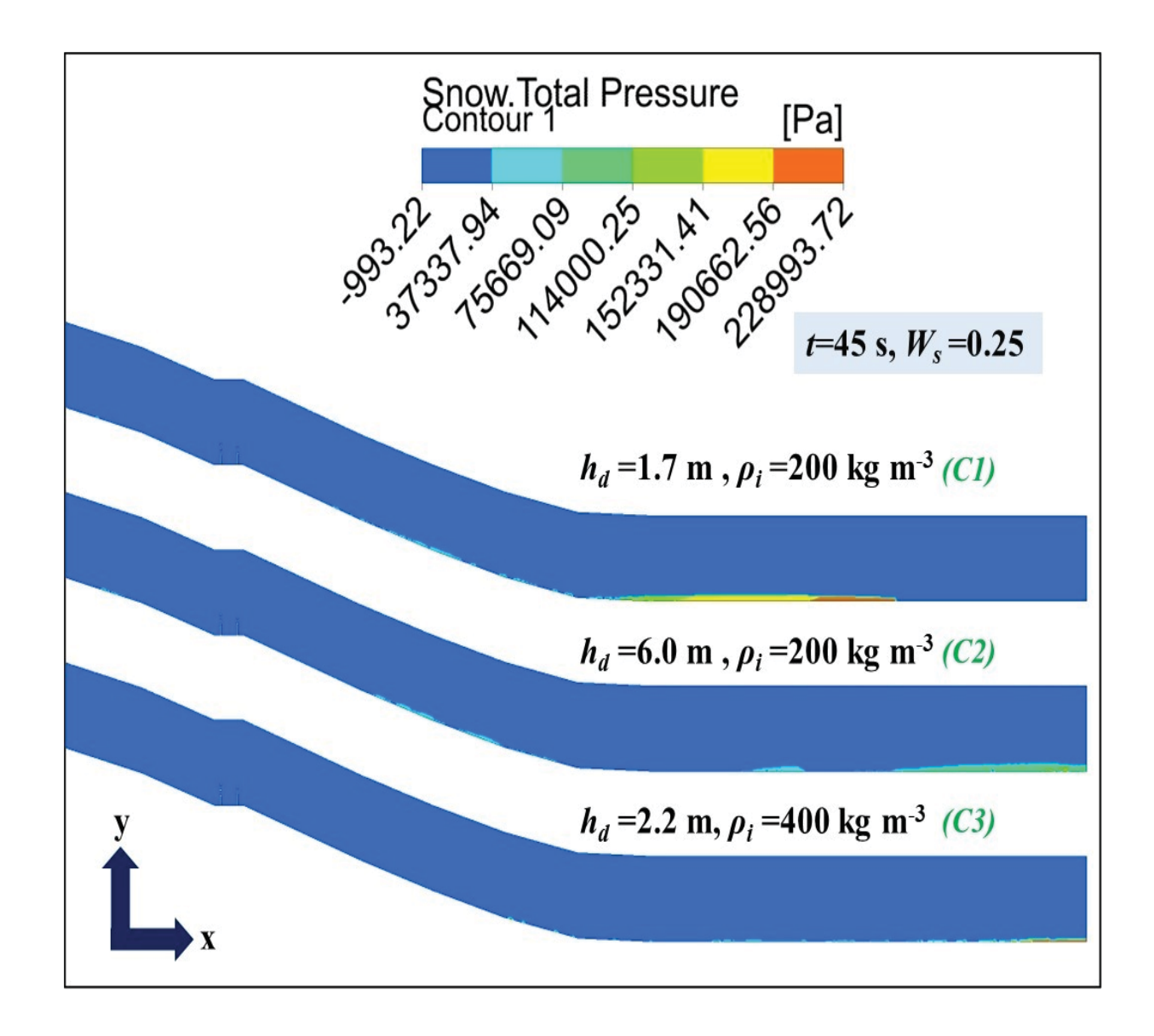


Figure 5.10: A zoomed view of simulation of snow total pressure P_s (Pa), in the three cases (C1, C2 & C3) having different snow density ρ_i (kg m⁻³) and fracture depth h_d (m) in the formation zone of the avalanche, at a time-step t=45 s and wall slip factor W_s =0.25

Tower as shown in Figure 5.11. However, there are deviations between the simulated avalanche debris around the Instrumented Tower and the observed profile. The main reason for this is that the present model has considered snow as a bi-viscous Bingham fluid. Although this model captures the rheology of snow quite well still this model does not take into account the granular behavior of snow like compressibility, snow grains cohesion, moisture content etc.

5.6 Conclusions

A two-dimensional model based on the solution of Navier-Stokes equations has been applied for the simulation of avalanche flow interaction with an Instrumented Tower structure installed at MSP-10 avalanche site, Dhundhi. Model is able to capture the overall avalanche flow interaction



Figure 5.11: Observations of snow deposition around the Instrumented Tower at MSP-10 avalanche site, Dhundhi, Himachal Pradesh, India during the winter period, just before the avalanche occurrence and after the avalanche occurrence

Chapter 5: Simulation of Avalanche Flow Interaction with an Instrumented Tower at a Real Avalanche Site

process with this tower structure quite convincingly. This model has a potential for the application in various kinds of mountain terrains. However, still the model has a number of limitations. The presented model does not take into account the snow compressibility, grains cohesion, moisture content of snow etc. which needs to be incorporated in the improved version of the model. Further, due to hazardous nature of the avalanches, only limited observations could be made. So, although a challenging task, still there is a need to collect more observed data for the occurrence of the avalanches for the validation of the model in the mountain regions.

Chapter 6

Conclusions and Future Scope

The objectives set in this thesis have been achieved with satisfaction. The main achievements of the present work are mentioned below:

- A 3-D model based on the solution of Navier-Stokes equations based approach for the simulation of avalanches and interaction with the obstacles has been developed.
- All the significant avalanche flow parameters i.e. velocity, avalanche debris depth, air blast pressure, viscosity, runout distance etc. have been simulated through the model.
- From the present investigation, it is found that the assumption of non-Newtonian fluid model and the wall-slip is crucial in capturing the rheology of the avalanche.
- A realistic interaction of avalanche flow with a catch dam kind of geometry was also studied which is not possible with the conventionally used depth-averaged models.
- The simulated avalanche debris depth values were determined to be in satisfactory conformity against the experimental observations with an average RMSE of 0.166.
- Good agreement was found between the simulated and observed avalanche front velocities with a RMSE of 1.48.
- One locally developed experimental facility was used to measure transient variation of the avalanche impact pressures.
- In order to get broad understanding of the subject, measured impact pressures were compared with the simulated values obtained through the present 3-D avalanche dynamics model.
- The RMSE between the present proposed model and the measured data is found minimum i.e., nearly 10.74, as compared to the existing prominent models for the estimation of avalanche impact pressure on the obstacles.

- The proposed effective drag coefficient C'_d found to vary in the range 3.97–8.54, that considers the solid, granular, and compressible properties of the snow into account, can better account for the deviations between the simulated and the measured avalanche impact pressures.
- Based on a substantial number of measurements, a new database for the shear force and normal force components of the avalanches and derived values of the dynamic coefficient of friction between the steel surface of snow chute, Dhundhi, India and the flowing snow has been generated. Based on all the measurements, average value of the dynamic coefficient of friction for snow-steel surface is estimated to be 0.113 with a standard deviation of 0.032. This database was applied in the model proposed in the current work.
- The present model was extended for the simulation of avalanche flow interaction with an Instrumented Tower structure installed at MSP-10 avalanche site, Dhundhi.
- Model is able to capture the overall avalanche flow interaction process with this tower structure quite convincingly. However, due to hazardous nature of the MSP-10 site, only limited observations could be made for the model validation.

To conclude, it can be emphasized here that the 3-D avalanche dynamics model developed in the present thesis, has a potential for the application in various kinds of mountain terrains. However, the model does not take into account the snow compressibility, grains cohesion, moisture content of snow etc. which needs to be incorporated in the improved version of the model (Kulibaba and Eglit, 2008; Favier et al., 2009). So far, a limited number of researchers have ventured into this area but slowly this topic is gaining momentum as understanding of avalanche rheology, interaction with the obstacles, compressibility of snow, snow grains cohesion, collisions etc. is very important for the accurate assessment of avalanche flow parameters and the avalanche impact pressures. In the near future, more research work can be taken up for incorporating the snow grains cohesion, collisions and compressibility effects in the avalanche dynamics models. Further, experimental work can be taken up to understand the effect of surface roughness on the dynamic friction coefficient of snow. Also, in future work, a more powerful computer can be used to speed up the study and carry out a more detailed investigation on the full-scale avalanches.

References

Abdelrazek, A. M., Kimura, I., Shimizu, Y. (2014). Numerical simulation of snow avalanches as a Bingham fluid flow using SPH method. *River Flow 2014 – Schleiss et al. (Eds)*, Taylor & Francis Group, London. https://doi.org/10.1201/b17133-210

Abdelrazek, A. M., Kimura, I., Shimizu, Y. (2016). Simulation of three-dimensional rapid free-surface granular flow past different types of obstructions using the SPH method. *Journal of Glaciology* 62(232):335–347. https://doi.org/10.1017/jog.2016.22

Aggarwal, R. K., Kumar, A. (2012). 2-D computational fluid dynamics model of avalanche flow interaction with an obstacle for snow chute at Dhundhi. *International Symposium on Cryosphere and Climate Change*, 2–4 April, Manali, India.

Aggarwal, R.K. (2022). New experimental investigation into the angle of repose of snow, *Journal of Cold Regions Engineering* 36(2). https://doi.org/10.1061/(ASCE)CR.1943-5495.0000276

Aggarwal, R.K., Das, R., Gusain, H.S. (2024). New database for the estimation of dynamic coefficient of friction of snow. *Open Geosciences* 16(1):20220639. https://doi.org/10.1515/geo-2022-0639

Alexandrou, A.N., Menn, P.L., Georgiou, G., Entov, V. (2003). Flow instabilities of Herschel–Bulkley fluids. *Journal of Non-Newtonian Fluid Mechanics* 116:19–32. https://doi.org/10.1016/S0377-0257(03)00113-7

Al-Hashemi, H.M., Al-Amoudi., O. (2018). A review on the angle of repose of granular materials. *Powder Technology* 330:397–417. https://doi.org/10.1016/j.powtec.2018.02.003.

Ancey, C., Meunier, M. (2004). Estimating bulk rheological properties of flowing avalanches from field data. *Journal of Geophysical Research* 109:F01004. https://doi.org/10.1029/2003JF000036

ANSYS Inc. (2015). *User manual of ANSYS Fluent 15.0 software*. Southpointe 275, Technology Drive, Canonsburg, USA.

Baroudi, D., Sovilla, B., Thibert, E. (2011). Effects of flow regime and sensor geometry on snow avalanche impact-pressure measurements. *Journal of Glaciology* 57(202):277–288. https://doi.org/10.3189/002214311796405988

Baroudi, D., Thibert, E. (2009). An instrumented structure to measure avalanche impact pressure: Error analysis from Monte Carlo simulations. *Cold Regions Science and Technology* 59:242–250. https://doi.org/10.1016/j.coldregions.2009.05.010

Bartelt, P., Salm, B., Gruber, U. (1999). Calculating dense snow avalanche run-out using a Voellmy fluid model with active/passive longitudinal straining. *Journal of Glaciology* 45 (150):242–254. https://doi.org/10.3189/S002214300000174X

Borstad, C.P. (2005). Dynamic modelling of extreme speed profiles of dry flowing avalanches. *Master's Thesis*, The University of British Columbia.

Bovet, E., Chiaia, B., De Biagi, V., Frigo, B. (2011). Pressure of snow avalanches against buildings. *Applied Mechanics and Materials* 82:392–397. https://doi.org/10.4028/www.scientific.net/amm.82.392

Bovet, E., Chiaia, B., Preziosi, L. (2010, a). A new model for snow avalanche dynamics based on non-Newtonian fluids. *Meccanica* 45:753–765. https://doi.org/10.1007/s11012-009-9278-z

Bovet, E., Chiaia, B., Preziosi, L. (2010, b). Interaction avalanche-obstacle: a first attempt of comparison between a real case study and numerical simulations. *Proceedings of the International Snow Science Workshop: 17-22 October, Lake Tahoe*, California.

Bovet, E., Preziosi, L., Chiaia, B., Barpi, F. (2007). The level set method applied to avalanches. *Excerpt from the Proceedings of the COMSOL Users Conference:23–24 October, Grenoble,* France.

Brugnot, G. (1987). Avalanche zoning, dynamics and control. Recent work done in France. Avalanche Formation, Movement and Effects (Proceedings of the Davos Symposium, September 1986). IAHS Publ. no. 162.

Brugnot, G., Pochat, R. (1981). Numerical simulation study of avalanches. *Journal of Glaciology* 27(95):77–88. https://doi.org/10.3189/S0022143000011242

Buhler, Y., von Rickenbach, D., Stoffel, A., Margreth, S., Stoffel, L., Christen, M. (2018). Automated snow avalanche release area delineation – validation of existing algorithms and proposition of a new object-based approach for large-scale hazard indication mapping. Natural Hazards Earth System Sciences 18:3235–3251. https://doi.org/10.5194/nhess-18-3235-2018, 2018.

Caccamo, P., Faug, T., Bellot, H., Naaim-Bouvet, F. (2011). Experiments on a dry granular avalanche impacting an obstacle: dead zone, granular jump and induced forces. *WIT Transactions on The Built Environment* 115:53–62. https://doi.org/10.2495/FSI110061

Casassa, G, Narita, H, Maeno, N. (1989). Measurements of friction coefficients of snow blocks. *Annals of Glaciology* 13:40–44. https://doi.org/10.3189/S0260305500007618

Christen, M., Kowalski, J., Bartelt, P. (2010). RAMMS: numerical simulation of dense snow avalanches in three-dimensional terrain. *Cold Regions Science and Technology* 63:1–14. https://doi.org/10.1016/j.coldregions.2010.04.005

Colbeck, S.C. (1988). The kinetic friction of snow. *Journal of Glaciology* 34(116):78–86. https://doi.org/10.3189/S0022143000009096

Dent, J.D., Lang, T.E. (1980). Modeling of snow flow. *Journal of Glaciology* 26(94):131–140. https://doi.org/10.3189/S0022143000010674

Dent, J.D., Lang, T.E. (1982). Experiments on the mechanics of flowing snow. *Cold Regions Science and Technology* 5(3):253-258. https://doi.org/10.1016/0165-232X(82)90018-0

Dent, J.D., Lang, T.E. (1983). A biviscous modified Bingham model of snow avalanche motion. *Annals of Glaciology* 4:42–46. https://doi.org/10.3189/S0260305500005218

De Biagi, V., Chiaia, B., Frigo, B. (2015). Impact of snow avalanche on buildings: Forces estimation from structural back-analyses. *Engineering Structures* 92(1):15–28. https://doi.org/10.1016/j.engstruct.2015.03.004

Domnik, B., Pudasaini, S.P. (2012). Full two-dimensional rapid chute flows of simple viscoplastic granular materials with a pressure-dependent dynamic slip-velocity and their numerical simulations. *Journal of Non-Newtonian Fluid Mechanics* 173–174:72–86. https://doi.org/10.1016/j.jnnfm.2012.03.001

Domnik, B., Pudasaini, S.P., Katzenbach, R., Miller, S.A. (2013). Coupling of full two-dimensional and depth-averaged models for granular flows. *Journal of Non-Newtonian Fluid Mechanics* 201:56–68. https://doi.org/10.1016/j.jnnfm.2013.07.005

Dong, Z-b., Su, L-j., Hu, B-l., Miao, S-s. (2024). Friction behaviors and flow resistances of rockice avalanches. *Cold Regions Science and Technology* 220:104130. https://doi.org/10.1016/j.coldregions.2024.104130.

Eglit, M.E., Kulibaba, V.S., Naaim, M. (2007). Impact of a snow avalanche against an obstacle: Formation of shock waves. *Cold Regions Science and Technology* 50:86–96. https://doi.org/10.1016/j.coldregions.2007.06.005

Faug, T., Caccamo, P., Chanut, B. (2012). A scaling law for impact force of a granular avalanche flowing past a wall. *Geophysical Research Letters* 39(23):L23401(1–5). https://doi.org/10.1029/2012GL054112

Faug, T., Chanut, B., Beguin, R., Naaim, M., Thibert, E., Baroudi, D. (2010). A simple analytical model for pressure on obstacles induced by snow avalanches. *Annals of Glaciology* 51(54):1–8. https://doi.org/10.3189/172756410791386481

Faug, T., Naaim, M., Fourriere, A. (2007). Dense snow flowing past a deflecting obstacle: An experimental investigation. *Cold Regions Science and Technology* 49(1):64–73. https://doi.org/10.1016/j.coldregions.2007.01.003

Faug, T., Naaim, M., Naaim-Bouvet, F. (2004). Experimental and numerical study of granular flow and fence interaction. *Annals of Glaciology*, 38:135–138. https://doi.org/10.3189/172756404781814870

Favier, L., Daudon, D., Donze, F.-V., Mazars, J. (2009). Predicting the drag coefficient of a granular flow using the discrete element method. *Journal of Statistical Mechanics: Theory and Experiment* P06012. https://doi.org/10.1088/1742-5468/2009/06/P06012

Fei, J., Jie, Y., Hong, C., Wu, Z. (2020). Modelling of avalanche-obstacle interaction using the depth-averaged continuum approach. *Granular Matter* 22(31):1–15. https://doi.org/10.1007/s10035-020-0995-2

Fierz, C., Armstrong, R.L., Durand, Y., Etchevers, P., Greene, E., McClung, D.M., et al. (2009). The international classification for seasonal snow on the ground. *Prepared by the ICSI*-

UCCS-IACS working group on snow classification (IHP-VII technical documents in hydrology). UNESCO: IHP.

Frigo, B., Bartelt, P., Chiaia, B., Chiambretti, I., Maggioni, M. (2020). Reverse Dynamical Investigation of the Catastrophic Wood-Snow Avalanche of 18 January 2017 at Rigopiano, Gran Sasso National Park, Italy. *International Journal of Disaster Risk Science* 12:40–55. https://doi.org/10.1007/s13753-020-00306-6

Furukawa, I. (1957). Impact of avalanche. *Journal of the Japanese Society of Snow and Ice* 19(5):140–141. https://doi.org/10.5331/seppyo.19.140.

Gleason, J.A. (2002). Preliminary results of snow surface friction coefficient measurements. *International Snow Science Workshop*, Penticton, British Columbia.:523–527.

Harbitz, C. B. (1998). A survey of computational models for snow avalanche motion, *EU Programme SAME*, NGI report no. 581220-1.

Hauksson, S., Pagliardi, M., Barbolini, M., Johannesson, T. (2007). Laboratory measurements of impact forces of supercritical granular flow against mast-like obstacles. *Cold Regions Science and Technology* 49:54–63. https://doi.org/10.1016/j.coldregions.2007.01.007

Hirt, C.W., Nichols, B.D. (1981). Volume of Fluid (VOF) method for the dynamics of free boundaries. *Journal of Computational Physics* 39(1):201–225. https://doi.org/10.1016/0021-9991(81)90145-5.

Hungr, O., McClung, D. M. (1987). An equation for calculating snow avalanche run-up against barriers. *Avalanche Formation, Movement and Effects (Proceedings of the Davos Symposium, September 1986)*, IAHS publ. no. 162.

Internet resource 1/https://en.wikipedia.org/wiki/Hannibal%27s_crossing_of_the_Alps

Internet resource 2/https://en.wikipedia.org/w/index.php?title=Avalanche_control & old id=1181599295

Internet resource 3/https://www.britannica.com/science/avalanche

Internet resource 4/https://www.slf.ch/en/avalanche-bulletin-and-snow-situation/about-the-avalanche-bulletin/avalanche-types

Internet resource 5/https://www.slf.ch/en/avalanche-bulletin-and-snow-situation/about-the-avalanche-bulletin/avalanche-sizes

Internet resource 6/https://www.sciencedirect.com/topics/earth-and-planetary-sciences/snow-avalanche

Jaedicke, C., Kern, M.A., Gauer, P., Baillifard, M.A., Platzer, K. (2008). Chute experiments on slushflow dynamics. *Cold Regions Science and Technology* 51:156–167. https://doi.org/10.1016/j.coldregions.2007.03.011

Kattel, P., Kaffle, J., Fischer, J.-T., Mergili, M., Tuladhar, B.M., Pudasaini, S.P. (2018). Interaction of two-phase debris flow with obstacles. *Engineering Geology* 242:197–217. https://doi.org/10.1016/j.enggeo.2018.05.023.

Kern, M.A., Tiefenbacher, F., McElwaine, J.N. (2004). The rheology of snow in large chute flows. *Cold Regions Science and Technology* 39:181–192. https://doi.org/10.1016/j.coldregions.2004.03.006

Keshari, A.K., Satapathy, D.P., Kumar, A. (2010). The influence of vertical density and velocity distributions on snow avalanche runout. *Annals of Glaciology* 51(54):200–206. https://doi.org/10.3189/172756410791386409

Khapayev, S. A. (1978). Dynamics of avalanche natural complexes: an example from the highmountain Teberda state reserve, Caucasus mountains, USSR. *Arctic and Alpine Research* 10(2):335–344. https://doi.org/10.1080/00040851.1978.12003971

Khattri, K.B., Fischer, J.-T., Jaboyedoff, M., Pudasaini, S.P. (2018). Wet snow avalanche simulations to assess flow-obstacle-interactions and potential defence structure designs. *Proceedings, International Snow Science Workshop*, Innsbruck, Austria.

Kocyigit, O., Gurer, I. (2007). Effect of the Voellmy coefficients on determining run-out distance: A case study at Uzungöl, Turkey. *Gazi University Journal of Science*, 20(3):79–85.

Kulibaba, V.S., Eglit, M.E. (2008). Numerical modeling of an avalanche impact against an obstacle with account of snow compressibility. *Annals of Glaciology* 49:27–32. https://doi.org/10.3189/172756408787814771

Kyburz, M.L., Sovilla, B., Gaume, J., Ancey. C. (2022). Physics-based estimates of drag coefficients for the impact pressure calculation of dense snow avalanches. *Engineering Structures* 254:113478 (1–17). https://doi.org/10.1016/j.engstruct.2021.113478

Lachamp, P., Faug, T., Naaim, M., Laigle, D. (2002). Simulation of the effect of defence structures on granular flows using SPH. *Natural Hazards and Earth System Sciences* 2:203–209. https://doi.org/10.5194/nhess-2-203-2002

Lang, T.E., Dawson, K.L., Martinelli, Jr., M. (1979, a). Application of numerical transient fluid dynamics to snow avalanche flow. Part I. Development of computer program AVALNCH. *Journal of Glaciology* 22(86):107–115. https://doi.org/10.3189/S0022143000014088

Lang, T.E, Dawson, K.L., Martinelli, Jr., M. (1979, b). Numerical simulation of snow avalanche flow. *Rocky Mountain Forest and Range Experiment Station Forest Service*, Research Paper RM-205, U.S. Department of Agriculture.

Lang, T.E., Brown, R.L. (1980). Snow-avalanche impact on structures. *Journal of Glaciology* 25(93):445–455. https://doi.org/10.3189/S002214300001529X

Lang, T.E., Dent, J.D. (1980). Scale modelling of snow-avalanche impact on structures. *Journal of Glaciology* 26(94):189–196. https://doi.org/10.3189/S0022143000010728

Lang, T.E., Martinelli, Jr., M. (1979). Application of numerical transient fluid dynamics to snow avalanche flow, Part II, Avalanche modeling and parameter error evaluation. *Journal of Glaciology* 22(86):117–126. https://doi:10.3189/S002214300001409X

Lang, T.E., Nakamura, T., Dent, J.D. & Martinelli, Jr., M. (1985). Avalanche flow dynamics with material locking. *Annals of Glaciology* 6:5–8. https://doi.org/10.3189/1985AoG6-1-5-8

Li, X., Sovilla, B., Jiang, C., Gaume, J. (2020). The mechanical origin of snow avalanche dynamics and flow regime transitions. *The Cryosphere* 14:3381–3398. https://doi.org/10.5194/tc-14-3381-2020

Ligneau, C, Sovilla, B, Gaume, J. (2022). Numerical investigation of the effect of cohesion and ground friction on snow avalanches flow regimes. *PLoS ONE* 17(2):e0264033. https://doi.org/10.1371/journal.pone.0264033

Maggioni, M., Barbero, M., Barpi, F., Borri-Brunetto, M., De Biagi, V., Freppaz, M., et al. (2019). Snow avalanche impact measurements at the Seehore Test Site in Aosta Valley (NW Italian Alps). *Geosciences* 9(471):1–20. https://doi.org/10.3390/geosciences9110471

Martinelli, Jr, M., Lang, T.E., Mears, A.I. (1980). Calculations of coefficients avalanche from field friction data. *Journal of Glaciology* 26(94):109–119. https://doi.org/10.3189/S0022143000010650

McClung, D.M., Mears, A.I. (1995). Dry-flowing avalanche run-up and run-out. *Journal of Glaciology* 41(138):359–372. https://doi.org/10.3189/S0022143000016233

McClung, D.M., Schaerer, P.A. (1983). Determination of avalanche dynamics friction coefficients from measured speeds. *Annals of Glaciology* 4:170–173. https://doi.org/10.3189/S0260305500005425

McClung, D.M., Schaerer, P.A. (1985). Characteristics of flowing snow and avalanche impact pressures. *Annals of Glaciology* 6:9–14. https://doi.org/10.3189/1985AoG6-1-9-14

McClung, D., Schaerer, P. (1999). *The avalanche handbook (First edition). The Mountaineers*, Seattle, Washington, USA.

McClung, D., Schaerer, P. (2011). *The avalanche handbook (Third edition)*. *The Mountaineers*, Seattle, Washington, USA.

Mead, L.B., Nakamura, H., Lang, T.E., Dent, J.D. (1986). Comparison of experimental and computer modeling of snow-block impact on structures. *Journal of Glaciology* 32(112):321–324. https://doi.org/10.3189/S0022143000011989

Mellor, M. (1975). A review of basic snow mechanics. *Proceedings of Grindelwald Snow Mechanics Symposium held April 1–5, 1974*, IAHS-AISH publ. no. 114:251–291.

Naaim, M., Durand, Y., Eckert, N., Chambon, G. (2013) Dense avalanche friction coefficients: influence of physical properties of snow. *Journal of Glaciology* 59(216):771–782. https://doi.org/10.3189/2013JoG12J205

Naaim, M., Faug, T., Thibert, E., Eckert, N., Chambon, G., Naaim, F., et al. (2008). Snow avalanche pressure on obstacles. *International Snow Science Workshop: 21–27 September, Whistler, B.C., Canada*: 740-746.

Nakamura, T., Nakamura, H., ABE, O., Sato, A., Numano, N. (1987). A newly designed chute for snow avalanche experiments. *Avalanche Formation, Movement and Effects (Proceedings of the Davos Symposium, September 1986)*, IAHS Publ. no. 162:441–451.

Nettuno, L. (1995). Field measurements and model calibration in avalanche dynamics. *Surveys in Geophysics* 16:635–648. https://doi.org/10.1007/BF00665744

Nguyen, Q.D., Boger, D.V. (1992). Measuring the flow properties of yield stress fluids. *Annual Review of Fluid Mechanics* 24(1):47–88. https://doi.org/ 10.1146/annurev.fl.24.010192.000403

Nishimura, K., Maeno, N. (1989). Contribution of viscous forces to avalanche dynamics. *Annals of Glaciology* 13:202–206. doi: 10.3189/S0260305500007898

Nishimura, K., Barpi, F., Issler, D. (2021). Perspectives on snow avalanche dynamics research. *Geosciences* 11(57):1–10. https://doi.org/10.3390/geosciences11020057

Nohguchi, Y. (1989). Three-dimensional equations for mass centre motion of an avalanche of arbitrary configuration. *Annals of Glaciology* 13:215–217. https://doi.org/10.3189/S0260305500007928

Norem, H., Irgens, F., Schieldrop, B. (1989). Simulation of snow-avalanche flow in run-out zones. *Annals of Glaciology* 13:218–225. https://doi.org/10.3189/S026030550000793X

Oda, K., Kamiishi, I., Yamaguchi, S., Nakamura, Y., Tanaka, T. (2014). Simulation of avalanche motion for design of snow prediction. *Proceedings of International Snow Science Workshop*, Banff:702–707.

Oda, K., Moriguchi, S., Kamiishi, I., Yashima, A., Sawada, K., Sato, A. (2011). Simulation of a snow avalanche model test using computational fluid dynamics. *Annals of Glaciology* 52(58):57–64. https://doi.org/10.3189/172756411797252284

Patankar, S.V. (2009). *Numerical heat transfer and fluid flow*. Taylor & Francis Group, CRC press, New York, USA.

Pedersen, R.R., Dent, J.D., Lang, T.E. (1979). Forces on structures impacted and enveloped by avalanches. *Journal of Glaciology* 22(88):529–534. https://doi.org/10.3189/S0022143000014507

Perla, R., Cheng, T.T., McClung, D.M. (1980). A two-parameter model of snow-avalanche motion. *Journal of Glaciology* 26(94):197–207. https://doi.org/10.3189/S002214300001073X

Platzer, K., Bartelt, P., Jaedicke, C. (2007). Basal shear and normal stresses of dry and wet snow avalanches after a slope deviation. *Cold Regions Science and Technology* 49:11–25. https://doi.org/10.1016/j.coldregions.2007.04.003

Platzer, K., Bartelt, P., Kern, M. (2007). Measurements of dense snow avalanche basal shear to normal stress ratios (S/N). *Geophysical Research Letters* 34:L07501. https://doi.org/10.1029/2006GL028670

Pudasaini, S.P., Hutter, K. (2007). Avalanche Dynamics: Dynamics of Rapid Flow of Dense Granular Avalanches. *Springer-Verlag Berlin and Heidelberg*. https://doi.org/10.1007/978-3-540-32687-8

Rao, N.M. (1985). Avalanche protection and control in the Himalayas. *Defence Science Journal* 35(2): 255–266. https://doi.org/10.14429/dsj.35.6020

Rohm, S., Hasler, M., Knoflach, C., Putten, J.V., Unterberger, S.H., Schindelwig et al. (2015). Friction between steel and snow in dependence of the steel roughness. *Tribology Letters* 59:27. https://doi.org/10.1007/s11249-015-0554-x

Romanova, D. I. (2017). 3D avalanche flow modeling using OpenFOAM. *Proceedings of ISP RAS* 29(1):85–100. https://doi.org/10.15514/ISPRAS-2016-29(1)-6

Saito, Y., Kato, H., Otsuki, M., Kimura, I., Shimizu, Y., Isenko, E. (2012). Refinement of MPS method for practical application to snow avalanches. *Annals of Glaciology* 53(61):13–22. https://doi.org/10.3189/2012AoG61A014

Salm, B. (1993). Flow, flow transition and runout distances of flowing avalanches. *Annals of Glaciology* 18:221–226. https://doi.org/10.3189/S0260305500011551

Salm, B. (2004). A short and personal history of snow avalanche dynamics. *Cold Regions Science and Technology* 39:83–92. https://doi.org/10.1016/j.coldregions.2004.06.004

Salm, B., Burkard, A., Gubler, H. (1990). Berechnung von Fliesslawinen: eine Anleitung für Praktiker mit Beispielen. Mitteilung 47, Eidg. Institut für Schnee- und Lawinenforschung SLF.

Salway, A.A. (1978). A seismic and pressure transducer system for monitoring velocities and impact pressures of snow avalanches. *Arctic and Alpine Research* 10(4):769–774. https://doi.org/10.1080/00040851.1978.12004014

Sanz-Ramos, M., Blade, E., Oller, P., Furdada, G. (2023). Numerical modelling of dense snow avalanches with a well-balanced scheme based on the 2D shallow water equations. *Journal of Glaciology*:1–17. https://doi.org/10.1017/jog.2023.48

Satapathy, D.P., Keshari, A.K., Kumar, A. (2009). Numerical modeling and experimental validation of runout distances. *Proceedings of International Symposium on Snow and Avalanches*, 6–10 April, SASE, Manali, India.

Sauermoser, S., Illmer, D. (2002). The use of avalanche calculation models practical experiences. *International Congress INTERPRAEVENT 2002 in the Pacific Rim-Matsumoto/Japan*, Congress publication 2:741-750.

Savage, S.B., Hutter, K. (1989). The motion of a finite mass of granular material down a rough incline. *Journal of Fluid Mechanics* 199:177–215. https://doi.org/10.1017/S0022112089000340

Schaerer, P.A. (1975). Friction coefficients and speed of flowing avalanches. *Snow Mechanics-Symposium (Proceedings of the Grindelwald Symposium, April 1974)*, IAHS Publ. no.114:425–432.

Sheikh, A.H., Verma, S.C., Kumar, A. (2008). Interaction of retarding structures with simulated avalanches in snow chute. *Current Science* 94(7):916–921. http://www.jstor.org/stable/24101748

Solowski, W. T., Baroudi, D., Ghobakhlou, M., Korkiala-Tanttu, L. K. (2015). Simulations of dense snow avalanches with generalized interpolation material point method: preliminary outcomes. *IV International Conference on Particle-based Methods–Fundamentals and Applications*, *PARTICLES* 2015, Barcelona, vol. 4.

Som, S.K., Biswas, G. (2008). Introduction to fluid mechanics and fluid machines. *Tata McGraw-Hill Publishing Company Ltd*, revised second edition, New Delhi, India.

Sovilla, B., Faug, T., Kohler, A., Baroudi, D., Fischer, J.-T., Thibert, E. (2016). Gravitational wet avalanche pressure on pylon-like structures. *Cold Regions Science and Technology* 126: 66–75. https://doi.org/10.1016/j.coldregions.2016.03.002

Sovilla, B., Schaer, M., Kern, M., Bartlelt, P. (2008). Impact pressures and flow regimes in dense snow avalanches observed at the Vall'ee de la Sionne test site. *Journal of Geophysical Research* 113: 1–14. https://doi.org/10.1029/2006 JF000688

Sovilla, B., Schaer, M., Rammer, L. (2008). Measurements and analysis of full-scale avalanche impact pressure at the Vallée de la Sionne test site. *Cold Regions Science and Technology* 51:122–137. https://doi.org/10.1016/j.coldregions.2007.05.006

Sovilla, B., Kyburz, M., Ligneau, C., Fischer, J.-T., Schaer, M. (2020). Spatial and temporal variability of snow avalanche impact pressure and its importance for structural design. 22nd EGU General Assembly Conference Abstracts Paper No. 813 (Online), 4–8 May. https://doi.org/10.5194/egusphere-egu2020-8133

Stabilini, F. (2019). Propagation and impact of a dense flow snow avalanche: from the small-scale experiments to the val di zocca event, *Master's Thesis*, *Department of Civil and Environmental Engineering*, Politecnico di Milano.

Takahashi, T., Yoshida, H. (1979). Study on the deposition of debris flows, Part 1 - Deposition due to abrupt change of bed slope. *Annuals, Disaster Prevention Research Institute, Kyoto University, Japan :*22 B-2.

Teufelsbauer, H., Wang, Y., Chiou, M.C., Wu, W. (2009). Flow-obstacle interaction in rapid granular avalanches: DEM simulation and comparison with experiment. *Granular Matter* 11: 209–220. https://doi.org/10.1007/s10035-009-0142-6

Teufelsbauer, H., Wang, Y., Pudasaini, S. P., Borja, R. I., Wu, W. (2011). DEM simulation of impact force exerted by granular flow on rigid structures. *Acta Geotechnica* 6:119–133. https://doi.org/10.1007/s11440-011-0140-9

Thibert, E., Baroudi, D., Limam, A., Berthet-Rambaud, P. (2008). Avalanche impact pressure on an instrumented structure. *Cold Regions Science and Technology* 54(3):206–215. http://doi.org/10.1016/j.coldregions.2008.01.005

Thibert, E., Faug, T., Bellot, H., Baroudi, D. (2013). Avalanche impact pressure on a plate-like obstacle, *International Snow Science Workshop, 7-11 October, Grenoble-Chamonix, France*: 663–670.

Tiefenbacher, F., Kern, M.A. (2004). Experimental devices to determine snow avalanche basal friction and velocity profiles. *Cold Regions Science and Technology* 38(1):17–30. https://doi.org/10.1016/S0165-232X(03)00060-0

Upadhyay, A., Kumar, A., Chaudhary, A. (2010). Velocity measurements of wet snow avalanche on the Dhundi snow chute. *Annals of Glaciology* 51(54):139–145. https://doi.org/10.3189/172756410791386580

Verma, S.C., Kumar, A., Panesar, G.R., Shukla, A.K., Mathur, P. (2004). An experimental study of snow avalanche friction parameters using snow chute, *Proceedings, International Symposium on Snow Monitoring and Avalanches (ISSMA), Snow and Avalanche Study Establishment (SASE), Manali, India, 12–16 April:*46-51.

Voellmy, A. (1955). Ueber die Zerstoerunskraft von Lawinen Schweizerische Bauzeitung. Jahrg. 73:159–165, 212–217, 246–249, 280–285 [English translation: On the destructive force of avalanches, Translated by R.E. Tate, U.S. Department of Agriculture Forest Service, Alta Avalanche Study Center, Wasatch National Forest, Translation No. 2, 1964].